Fall 11-2020

THE NATURAL POTENTIAL OF TRANSITION METALS TO ACTIVATE THE INITIAL STEPS OF FISCHER-TROPSCH CATALYSIS: A DFT STUDY

Sumegha Godara

THE NATURAL POTENTIAL OF TRANSITION METALS TO ACTIVATE THE INITIAL STEPS OF FISCHER-TROPSCH CATALYSIS: A DFT STUDY

by

Sumegha Godara, B.E., MS.

A Dissertation Presented in Partial Fulfillment
of the Requirements of the Degree
Doctor of Philosophy

COLLEGE OF ENGINEERING AND SCIENCE
LOUISIANA TECH UNIVERSITY

November 2020

ABSTRACT

With recent advances in modeling and simulations methods along with state-of-the-art supercomputers, theoretical studies are becoming a cheaper choice for scientific predictions and provide complementary support to the experiments. Intense research in catalysis has been done in the past two decades experimentally as well as theoretically. This works employs first-principle studies to predict the most promising catalysts for Fischer-Tropsch (FT) reaction based on size and composition. The transition metals Fe, Co, Ni, Ru, Pd, and Pt, have been explored in pure and alloyed nanocluster forms for the effectiveness of catalytic properties.

The first and most crucial step of the FT reaction is carbon-mono-oxide adsorption on the surface of the catalyst, followed by its dissociation to form long-chain hydrocarbons. The studies done in this work explores the natural potential of the metals towards the CO adsorption and dissociation and provide a reference for further studies to find the best catalyst for the FT reaction. In this work density, functional theory calculations were carried out using Generalized Gradient Approximation with RPBE functional on two sizes of pure and bimetallic nanoclusters viz. ~0.5 nm and ~1.2 nm consisting of 13 and 55 atoms respectively. Core-shell icosahedron geometry of nanoclusters in the form of A_1B_{12} (0.5 nm) and $A_{13}B_{42}$ (1.2 nm) is used. Bimetallic nanoclusters are formed using a combination of the above-mentioned metals. 13-atom clusters pure and binary clusters of Ru, Pd, and Pt, are explored with DND and DNP basis sets while 55-atom nanoclusters studies are done

using plane-wave basis sets. Based on the CO adsorption and dissociation energies, an initial predictor, percentage difference was proposed to identify potentials catalyst systems. In 13-atom pure systems Ru was found to have the highest value of the % difference. In 55-atom clusters of Ru, Ni, Pd, and Co, Ru was found to have a maximum value of the percentage difference, hence greater catalytic performance.

In bimetallic systems, only systems showing better excess energy were considered for further studies. Surface energy was seen to be the dominant factor in the binding of metal atoms in a core-shell arrangement. In bimetallic 55-atom nanoclusters, $Fe_{13}Ru_{42}$ was found to be the best catalyst among all the binary combinations explored. Ni and Pt are better than Ru, Co, and Fe (in decreasing order of preference) in the core of cluster when shell metal is Pd. $Fe_{13}Co_{42}$ nanocluster was found to have greater value of percentage difference than bare Co nanocluster of same size. Ru, Co, and Fe (in decreasing order of preference) preferred to be in the core of the cluster where host(shell) element is Ni than the pure Ni cluster. $Fe_{13}Pt_{42}$ was found to be better than any other element in the core of cluster, when shell was composed of Pt. The initial predictor proposed in this work predicted the order of preference of potentials catalyst (top 6 candidates) as follows: $Fe_{13}Ru_{42} > Ru_{55} > > Ru_{13}Ni_{42} > Pd_{55} > Co_{13}Ni_{55} > Fe_{13}Ni_{42}$.

APPROVAL FOR SCHOLARLY DISSEMINATION

The author grants to the Prescott Memorial Library of Louisiana Tech University the right to reproduce, by appropriate methods, upon request, any or all portions of this Dissertation. It is understood that "proper request" consists of the agreement, on the part of the requesting party, that said reproduction is for his personal use and that subsequent reproduction will not occur without written approval of the author of this Dissertation. Further, any portions of the Dissertation used in books, papers, and other works must be appropriately referenced to this Dissertation.

Finally, the author of this Dissertation reserves the right to publish freely, in the literature, at any time, any or all portions of this Dissertation.

Author _____

Date _____

DEDICATION

This Dissertation is dedicated to my beloved grandmother, Rukma Devi; to my beloved parents, Laxmi Narayan (father) and Kusam Lata (Mother); to my beloved brother, Sunil Godara; to my husband, Rahul Sharma; to my daughter, Shivanya Laxmi Sharma; Narendra Kumar; Vijendra Singh; and to all my family, friends and my advisors who have made the completion of this dissertation possible.

TABLE OF CONTENTS

LIST OF FIGURES

LIST OF TABLES

ACKNOWLEDGMENTS

I would like to thank Dr. Daniela S Mainardi for giving me such an opportunity to conduct research under her supervision. I am greatly indebted to all the support and guidance at each step of the research program.

I express my profound gratitude to Dr. B. Ramu Ramachandran for all the encouragement and for always being there to clear my doubts during all these years.

My sincere thanks to Dr. Collin Wick and Dr. Derosa for the guidance and help provided during my doctoral studies. Thank you, Dr. Shengnain Wang, for the courses he taught, which helped me to keenly observe the components of my research.

I would like to thank my parents, Mr. Laxmi Narayan, and Mrs. Kusam Lata, and my Late brother, Sunil Godara, for their support and motivation.

I would like to thank my husband, Rahul Sharma, and his parents, Mr. Prakash Chandra, and Mrs. Meena, for their support.

Thank you very much, Mr. Tarachand, Mrs. Santosh Devi, Dr. Vijendra Singh, Narendra Kumar, Virendra Kumar, Dr. Sudhir Amritphale, Smita Amritphale, Fernando Soto, and Suraj Gyawali, for all your support and encouragement during all these years at Louisiana Tech University.

CHAPTER 1

INTRODUCTION

1.1 Fischer Tropsch Synthesis

The growing demand for low cost and clean energy sources and depletion of natural reserves of fuel has increased the search for diverse energy resources like solar, wind, biomass, etc. To meet with increasing demands of energy in today's world, considering the limited amount of crude oil, the need for alternative resources of fuel arises. Out of various alternate resources of fuels, Fischer Tropsch synthesis (FTS) is the most viable and green resource. FTS was discovered by two German scientists named Franz Fischer and Hans Tropsch in the 1920s based on the discovery of the syn-gas($CO+H_2$) by Sabatier and Senderens[1]. The FTS process is such a technology that provides clean fuel but also has been challenging in several aspects[2]. Heterogeneous catalysis has been crucial in recent years and prerequisite for around 20% of industrial world production[3].

The feedstocks in this FTS process are natural gas, coal, and biomass, which produce syn-gas and a wide variety of products (linear paraffin, oxygenates, and α-olefins) yield by series of primary and secondary reactions. FTS is a process that converts a mixture of carbon-mono-oxide (CO) and hydrogen to liquid hydrocarbons over the surface of a catalyst. The reactions that take place during FTS are given in the following equations[4].

$$nCO + (2n+1)H_2 \xrightarrow{Surface\ of\ Catalyst} C_nH_{2n+2} + nH_2O \quad \textbf{Eq. 1-1}$$

$$nCO + 2nH_2 \xrightarrow{Surface\ of\ Catalyst} C_nH_{2n} + nH_2O \quad \textbf{Eq. 1-2}$$

$$CO + H_2O \xrightarrow{Surface\ of\ Catalyst} CO_n + H_2 \quad \textbf{Eq. 1-3}$$

Where *n* is an integer. **Eq. 1-1**, **Eq. 1-2**, and **Eq. 1-3** are the reactions for alkane production, alkene production, and water-gas shift reaction, respectively.

Catalysts are the compounds which accelerate the reaction by lowering the energy barrier of the reaction. This FTS reaction happens in the presence of catalysts, mainly Ruthenium (Ru), Iron (Fe), and Cobalt (Co), and Nickel (Ni)[5]. At first, iron was used as a catalyst by Fischer and Tropsch which produced long-chain hydrocarbons at low pressure, but it deactivated rapidly[6]. This led to the intense studies of metal catalysts including cobalt and nickel. The 3d and 4f transition metals i.e. Pd, Ru, Pt, Rh, Os, Ir, etc. are considered suitable for adsorption of CO and H_2[6].

The activity and product selectivity of a catalyst depends on the reaction conditions, use of promoters and support, size, shape, and composition[7]. For instance, Fe, Co, and Ru are known to be suitable to produce long-chain hydrocarbons while Pd, Os, Ir, and Pt produce methanol. Ni and Rh are known to produce methane and oxygenates respectively[8]. Based on the operating temperature, FT processes can be classified as low-temperature Fischer-Tropsch (LTFT) i.e. @ 200-240 ºC, and high-temperature Fischer-Tropsch (HTFT) i.e. @300-350 ºC[4]. However, the operating temperature of the FT process is typically set around the intermediate temperature between LTFT and HTFT i.e., 275 ºC, and pressure ranging from one to several tens of atmospheric pressure[9].

1.2 Reaction Mechanism

FT process has been of great interest due to the clean Sulphur free fuel production with almost no aromatic substances[7], [10]. FT is a catalyzed polymerization reaction that starts with the adsorption of CO on the surface of the catalyst and hydrogenated to form CH_x monomers, which are also called chain initiation steps followed by chain growth and chain termination steps. Intense studies to understand the mechanism of the reaction (hydrocarbon formation sequence) have been conducted to date. According to Sabatier's principle, if the interaction between catalysts and reactants is too weak, there will be no reaction due to the drifting away of the reactant from the catalyst surface. Conversely, if the bond is too strong, the product will not leave the surface, causing the poisoning of the catalyst[11]. Widely accepted mechanisms for the FT reaction i.e. the surface carbide mechanism and surface enol mechanism, are discussed in the next section.

1.2.1 Surface Carbide Mechanism

Figure 1-1 Shows the schematic of steps involved in the surface carbide mechanism.

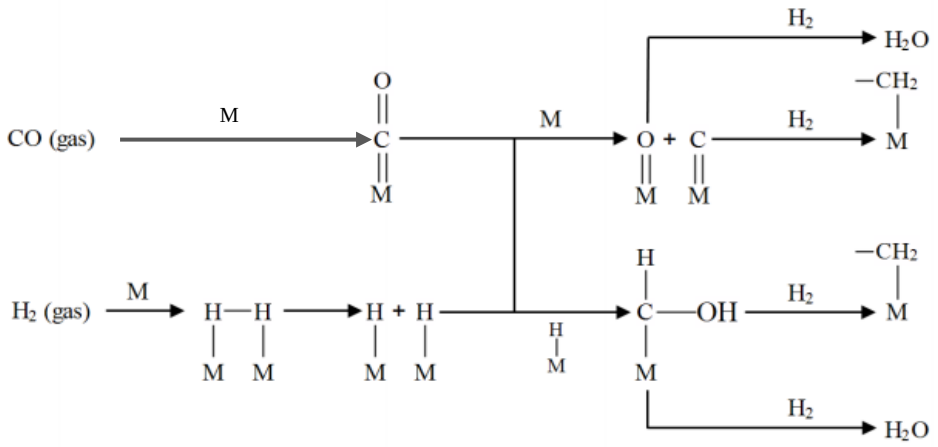

Figure 1-1: Surface Carbide mechanism steps imported from Ref. [12], [13]. M denotes metal surface.

In the surface carbide mechanism, the chain initiation step is executed by the chemisorption of the gaseous CO on the catalyst surface, forming the metal (M) - carbide bonds. Subsequently, CO is dissociated into C and O species on the catalyst surface[11]. Further, as a second reactant, hydrogen gets chemisorbed and dissociated on the metal catalyst surface. During the reaction between adsorbed CO and H_2, intermediate species C_1 is formed (as M-CH_x, x is an integer) and leads to CH_2 formation, removing the oxygen as water. In 1926 Franz Fischer and Hans Tropsch also assumed the same probable path[11].

1.2.2 Surface Enol Mechanism

Another plausible path in the reaction mechanism to form the monomer units is the formation of enol groups (M=CHOH), which was proposed by Storch in 1951[14]. In this mechanism, the adsorbed CO does not get dissociated, and H* from the adsorbed H_2 reacts with CO* to form formyl species (HCO*/COH*). Further hydrogenation of the formyl group leads to the generation of enol groups. Chain growth steps (formation of monomers) is propagated by the condensation of neighboring enolic groups[12].

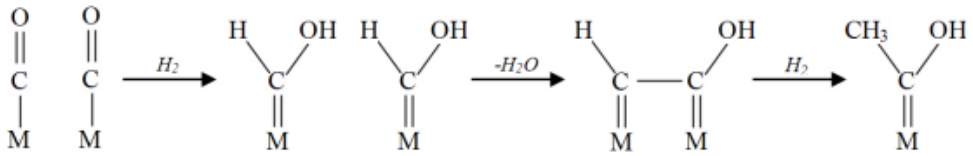

Figure 1-2: Mechanism scheme of enol intermediates imported from Ref. [12], [15]. M denotes metal surface.

1.3 Literature Review

Understanding the mechanism of activation and dissociation of CO is important as this is the very first step in the FTS process and it determines which and how the monomers (CHx) are formed as well as how the chain growth will advance[16]. Extensive experimental and theoretical studies have been carried out to investigate the mechanism of CO activation and dissociation on the catalysts surface in the past. Computational Approach is one of the key tools for understanding the chemical kinetics and thermodynamics pathway for material synthesis[17]–[19]. CO binding energy plays a crucial role in FT catalysis. Changing the shape, size, and composition of catalysts can change the CO binding energy and hence can help to find a catalyst with higher activity.

Studies have shown that the dissociation barrier of CO is higher when it is done directly onto the surface of a catalyst when the dissociation of the bond occurs in products of hydrogen-assisted reaction[16]. On flat surfaces, it is acknowledged that the H-assisted reaction pathway has a lower barrier than the direct CO dissociation[20]. Different mechanisms can work simultaneously on the catalyst surface that will have more than one active site [16]. The coverage of CO on the cluster, the effect of support, and promotes can change the adsorption energy and overall catalytic activity of the nanocluster[21].

Experimental studies using electron diffraction and infrared spectroscopy have shown that CO binds at hollow sites on Pd (111) crystal at low loading(coverage of CO)[22], [23]. In reactions like the FTS process, the catalyst activity and selectivity depend on the type and size of the metal catalyst.

Theoretical studies were done by Inderwildi et al. show that carbide mechanism is not feasible on Co(0001) surfaces while the different pathway via CHO and CH_2O is preferred, though this result requires experimental evidence [20]. Liu et al. studied the dissociation of CO to C and O on the flat, kinked, and stepped surfaces of Ru, Pd, and Rh metals using DFT. They found that the CO dissociation barrier is relatively low at the kinked and stepped surface of Rh (111) as compared to the flat Rh (111) surface. The same results were obtained in the case of CO dissociation on the Pd (111) surface. Figure 1-3 shows the three sites of CO dissociation i.e. flat, step, and kink on the Rh surface[20].

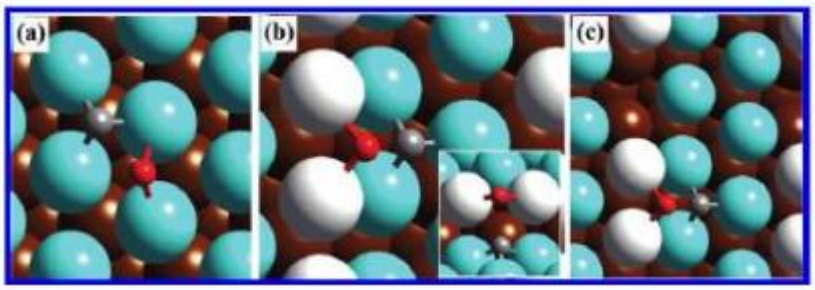

Figure 1-3: The top view of the calculated TS structures for the CO dissociation reactions on Rh(111) (a) Rh(111) Flat surface (b) Rh-step and (c) Rh- kink. The side view of TS on the Rh-step is shown in the inset in (b). The small gray balls, small red balls, and big blue balls are C atoms, O atoms, and Rh atoms, respectively. In particular, the step-edge Rh atoms in the Rh-step and Rh-kink are shown as big white balls[20]

Bimetallic catalysts are seen to have better selectivity towards higher molecular weight hydrocarbons[24]. Xiao et al. have reported the increase in the catalytic activity of bimetallic CoRu alloy as compared to their monometallic counterparts[24]. The ratio of

metals in bimetallic catalysts plays an important part in the activity of alloy. For instance, Ma et al. reported a decrease in CO conversion when Fe content was increased in $FeCo@SiO_2$ catalysts[25].

In recent years, small nanoclusters (~2 nm) are studied widely for their different catalytical properties than their corresponding bulk due to their shape and size. The high surface to volume ratio of these nanoclusters provides more active sites of the CO adsorption[13]. DFT has predicted active sites on (111) crystal surfaces of Pd, Pt, and Ru similar to as found experimentally[26]. The smaller the cluster size more atoms are located on the surface and those atoms are coordinatively unsaturated[14]. The properties of these nanoclusters can be tweaked by alloying with other metals, hence enhancing the catalytic activity. The studies on PdAu nanoalloy show that adsorption of CO is weaker on the alloyed surface than that of pure Pd[27]. Understanding the interaction CO with the metallic surface is crucial to predict the efficiency of various catalyst models.

GGA-RPBE functional has been shown to correctly describe the adsorption energies or bond strengths of small molecules on transition metal surfaces[28]. Icosahedron clusters consist of (111) facets that provide different active sites for the adsorption of CO (very first step).

1.4 Goal and Objectives of this work

According to the most popular surface carbide mechanism, the very first step of the FT reaction is CO adsorption, followed by its dissociation on the surface of the metal catalyst. The goal of this research is to find the natural potential of the elements (Ru, Pd, Pt, Ni, Co, and Fe) to break the CO bond on its surface not only for FT but for every

reaction which starts from CO adsorption and dissociation. This goal is accomplished by the following objectives:

1.4.1 To investigate the effect of cluster size on the CO adsorption and breaking on the catalyst surface:

Two sizes of clusters with icosahedron geometry[29] are used in this work, 13 atom cluster with a diameter of ~0.5 nm and 55 atom clusters with a diameter of ~1.2 nm[30]. Icosahedron models of 13 and 55 atom transition metal nanoclusters are thoroughly studied by ab initio methods in the last two decades due to their relatively high stability[31]. Icosahedron geometry has a core-shell structure. For instance, in 13 atom cluster, it has 1 atom in the center and 12 atoms in the shell of the cluster. 55 atom cluster consists of three layers with 1, 12, and 42 atoms in each layer from the center towards the surface of the cluster. This core-shell packing is more favorable in bimetallic clusters as the smaller atom occupies the core, hence reducing the compressive strain[32].

1.4.2 To investigate the effect of cluster composition on the CO adsorption and breaking on the catalyst surface:

Previous studies have shown that systematically arranged bimetallic clusters have shown better selectivity and catalytic performance towards a particular reaction than monometallic clusters [33]. Segregation in alloyed nanoclusters depends upon the atomic radius and surface energy of the metals used[34]. It has been seen in several studies that the smaller atom tends to stay in the core of the bimetallic cluster and vice versa[34].

In heterogeneous catalysis, the active sites play a pivotal role and are capable of changing the surface interactions between the adsorbate and the catalyst surface. Hence, all possible active sites are investigated in this work. In this work, we have investigated the

potential of metal nanocluster itself on the CO adsorption and dissociation without considering the reaction conditions.

To the best of my knowledge, the CO adsorption and dissociation on all six (Ru, Fe, Co, Pt, Ni, Pd) icosahedral pure and bimetallic metal clusters theoretically on GGA-RPBE theory level have never been studied.

Hypothesis: *Changing the size and core-shell composition of nanoclusters can change the CO adsorption and dissociation energies on the surface of a catalyst for FT like reactions (starting with CO adsorption and dissociation).*

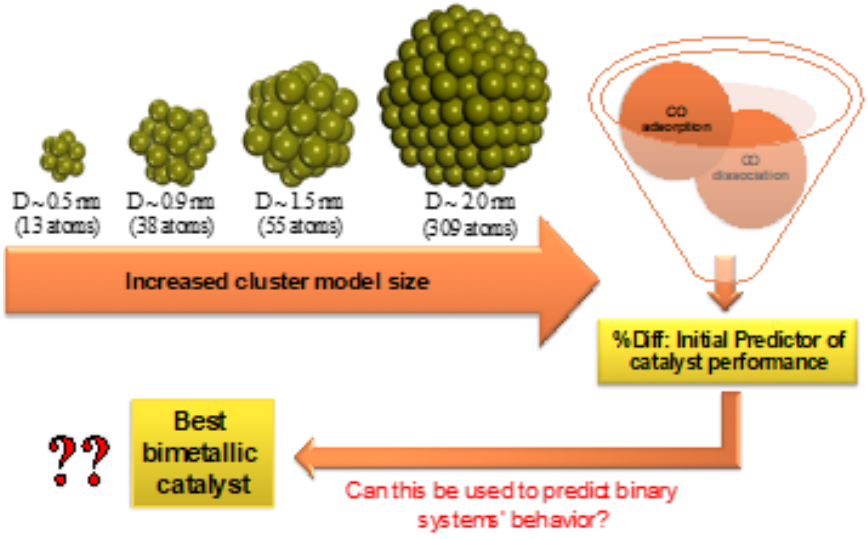

Figure 1-4: Schematic of the Approach used in this work.

In this work, CHAPTER 2 discusses the methods and techniques used in our DFT studies with a brief overview of DFT. CHAPTER 3 discusses the geometry and stability of the 13 atom pure and binary nanoclusters. In CHAPTER 4, the computational findings on CO adsorption and dissociation studies performed on the 13 atoms (~0.5 nm) pure nanoclusters of Ru, Pd, and Pt, and the bimetallic clusters (combinations of Ru, Pd, Ni, Pt, Fe, and Co) are discussed. My colleague worked on the rest of the pure 13-atom clusters

of Fe, Co and Ni, hence 13 atom clusters mainly include the three metals(Ru, Pd, and Pt) in pure cluster form as well as in the shell of bimetallic clusters. In CHAPTER 5, computational studies on geometry and thermodynamic stability of bimetallic nanoclusters consisting of 55 atoms (~1.2 nm) pure (Ru, Pd, Ni, and Co) and bimetallic (combinations of Ru, Pd, Ni, Pt, Fe, and Co) nanoclusters are presented and discussed. CHAPTER 6 presents the CO adsorption and bond breaking on the surface of 55 atom pure and bimetallic clusters along with chemical stability and charge transferred after CO gets bonded to the cluster surface. In CHAPTER 7, the effect of size and composition on the overall catalytic activity of the clusters is discussed. Finally, CHAPTER 8 summarizes the research work and lists future work.

CHAPTER 2

COMPUTATIONAL MODELING METHODS

Nowadays, computational modeling is widely employed in materials science due to advancements in computational technology. Over the last two decades, computational methods have become more accurate and can assist and guide experiments[28]. This chapter describes the theory behind the electronic structure methods used in this work to calculate the electronic properties of transition metals used. The Density Functional Theory (DFT) is one of the most popular quantum mechanical approaches to calculate the properties e.g. energy, molecular structure, etc. of molecular systems. The software used in this works is as follows:

- DMol^3: a module of the Biovia Materials Studio Suite from Accelrys, Inc[35]
- Vienna Ab Initio Simulation Package (VASP)[36]

2.1 Many-Body Equation

Quantum mechanics deals with the mathematical description to predict the behaviors of subatomic particles. It provides the basis to understand the energetics and structure of atoms, molecules, and solids. The behavior of quantum particles can be understood by solving the time-independent Schrödinger equation, which was given by a physicist named Erwin Schrödinger in 1926[21], which is as follows:

$$H\Psi(R,r) = E\Psi(R,r) \qquad \textbf{Eq. 2-1}$$

where, H is the Hamiltonian operator[37] as shown in **Eq. 2-2**,

$$H = \hat{T} + \hat{V} + \hat{U} \qquad \textbf{Eq. 2-2}$$

$\hat{T}$, $\hat{V}$, and $\hat{U}$ are the kinetic energy operator, electron-nucleus interaction potential operator, and electron-electron interaction operator, respectively,

Ψ is the wave function, E is the eigenvalue of H, and R and r are the position vectors of positions of nuclei and electrons, respectively[38].

The total energy of a system can be calculated by solving the Schrödinger equation. However, the exact solution for any system other than 1-electron systems is not possible, given the dimensionality of the wave function. Therefore, the need for an alternative and simpler descriptor for the system led to the implementations of the mathematical approximations. One such approximation was proposed by Max Born and Robert Oppenheimer in 1927, also known as Born-Oppenheimer Approximation[39]. This approximation suggests that since the mass of electrons is much smaller than the mass of nuclei, the nuclei may be considered as static and that only electrons move. This removes the nuclei kinetic energy term leaving behind the movement of electrons around the fixed nucleus, hence creating a potential energy surface (due to nuclei) for electron movement[40]. But solving the Schrödinger equation is still complicated due to the many-body character of the electronic wave function in BO approximation i.e. electronic behavior depends on the relative position of other electrons in the system.

This gave birth to relatively simpler computational such as Hartree-Fock (HF) approximation, semi-empirical methods, and Density Functional Theory (DFT). DFT is different from HF and semi-empirical methods as instead of solving Eq. 2-3 using the wave function, and it solves the many-body problem by using electron density[21].

2.2 Density Functional Theory

2.2.1 Introduction to DFT

DFT is based on the two theorems given by Hohenberg and Kohn[41] in 1964. According to the first theorem, the ground state properties of the system are a unique functional of the electron density. To elaborate further, every system has a unique electronic structure hence the electron density for each system. The second Hohenberg and Kohn theorem states that we can define a universal functional of energy in terms of density for any external potential. It means the density which globally minimizes the functional is the ground state density, and the value of the global minima of the functional is the ground state energy[42].

2.2.2 Kohn-Sham Equations and Exchange-Correlation Functional

Later in 1965, the Kohn-Sham[43] equation was proposed, which is based on the construction of a system having non-interacting particles having the same density as that of a system containing interacting particles. According to that, the ground state energy[37] can be written as shown in Eq. 2-4.

$$E(\rho) = T(\rho) + U(\rho) + E_{xc}^{KS}(\rho) \qquad \textbf{Eq. 2-5}$$

where, $T(\rho)$ is the kinetic energy of the non-interacting system,

$U(\rho)$ is the electrostatic energy due to Coulombic interactions and can be expressed as shown in **Eq. 2-6**

$$U(\rho) = \int v_N(r)\rho(r)dr + \frac{1}{2}\int \frac{\rho(r_1)\rho(r_2)}{|r_1 - r_2|} dr_1 dr_2 + V_{NN} \qquad \textbf{Eq. 2-6}$$

where the first, second, and third terms represent the electron-nucleus attraction, electron-electron interaction, and nucleus-nucleus repulsion, respectively,

$E_{ee}^{KS}(\rho)$ in **Eq. 2-5** represents the Kohn-Sham exchange-correlation energy functional (sum of quantum mechanical exchange-correlation energy and correlation kinetic energy).

Now, to calculate the exchange-correlation functional, a few approximations were made such as Local density approximation (LDA), Generalized Gradient Approximation (GGA), meta-GGA, and hybrid functionals. The LDA[21] is the simplest functional in which exchange-correlation energy is derived from the homogeneous electron gas (HEG) model. **Eq. 2-7** shows the LDA exchange-correlation energy for a spin-polarized system, where e_{xc} is the exchange-correlation function of a HEG with two spin densities ρ_a, ρ_b with $\rho = \rho_a + \rho_b$.

$$E_{xc}^{LDA}(\rho) = \int \rho(r)\, e_{xc}(\rho_a, \rho_b) dr \qquad \textbf{Eq. 2-7}$$

LDA functionals work well for an infinite HEG, but for the real systems which have inhomogeneous density, give inaccurate results[44]. It predicts very large binding energies and overbinds the weakest intramolecular interactions in comparison with the experimental values[44]. To overcome these problems a new approximation GGA was introduced with gradient corrections in electron density and showed significant improvement upon LDA in measuring the molecular properties[38]. The exchange-correlation functional for the GGA is shown in **Eq. 2-8**

$$E_{xc}^{GGA}(\rho) = \int \rho(r)\, e_{xc}(\rho_a, \rho_b) |\nabla \rho_a, \rho_b| dr \qquad \textbf{Eq. 2-8}$$

where $\nabla(\rho_a, \rho_b)$ is the gradient of the electron density.

Over the years, several successful GGA functionals were derived. The most commonly used GGA functionals are PW91(Perdew & Wang)[45], PBE (Perdew-Burke-

Ernzerhof)[46], and RPBE (Revised Perdew-Burke-Ernzerhof)[47]. In this dissertation, all of the calculations are done using the GGA-RPBE functional as it is known to predict accurate molecular adsorption energies[48].

2.2.3 Potential Energy Surface (PES)

In simple terms, PES is the graphical relationship between the geometry of the system and its energy in a $3N-6$, dimensional space where N is the number of atoms. The potential energy of a molecular system changes as we change conformational parameters, such as the bond length of a diatomic molecule (either stretch or compress it), and this is represented in the PES for that system. Additionally, a molecular system has energy (vibrational) even at 0 K, and this is called zero-point vibrational energy (ZPVE)[49].

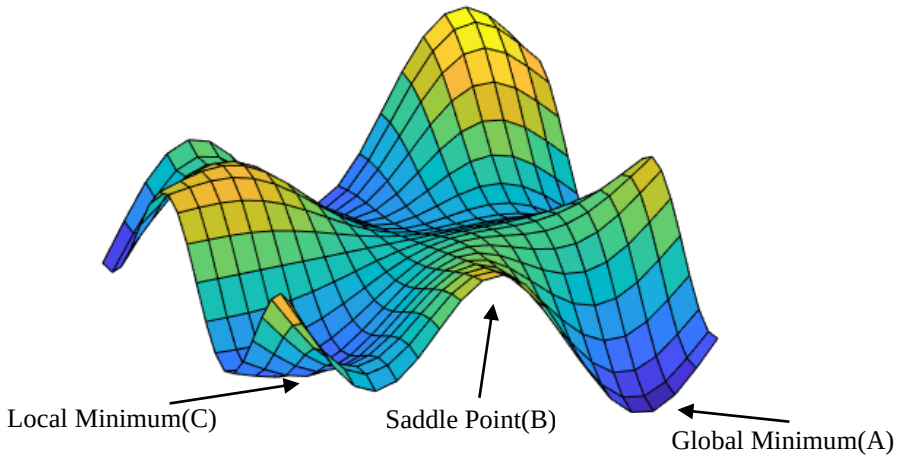

Figure 2-1: Schematic representation of PES of a system containing 3 atoms. (Created via MATLAB).

In **Figure 2-1**, the energy of the system is minimum at point A and called global minimum (only one), point C is another low energy extreme point which is called a local minimum. We define minima where the first and second derivatives of the energy with

respect to geometry are zero and positive, respectively. Also, the energy for nearby geometric conformations of these minima in any directions is higher. The point B in **Figure 2-1** is called saddle point where the first and second derivatives of energy are zero and negative, respectively[49]

2.2.4 Basis Sets

Basis sets are mathematical functions that represent the molecular orbitals[50]. An electron can exist anywhere in space; basis sets confines the electron in a specific region. To get a more accurate approximation of the system, we need larger basis sets that also demand expensive computational resources.

Molecular orbitals can be expressed in the form of linear combinations of atomic orbitals as

$$\Phi_i(r) = \sum_a C_i^a \chi_a(r) \qquad \textbf{Eq. 2-9}$$

where, χ_a represents atomic orbital, Φ_i denotes molecular orbitals, and C is a constant.

The basis set functions have two types, the first type is atom centered which includes slater type orbitals (STO) and Gaussian type orbitals (GTO) and the second type is non-atom centered which are delocalized[51]. Mathematically STO and GTO can be represented as shown in Eqs. 2-10 and 2-11.

$$\chi^{GTO} = Nx^l y^m z^n e^{-ar^2} \qquad \textbf{Eq. 2-12}$$

$$\chi^{STO} = Nr^{n-1} e^{-ar} y_{lm}(\theta, \varphi) \qquad \textbf{Eq. 2-13}$$

where, N is a normalization factor, $x, y,$ and z are Cartesian coordinates, $r, \theta,$ and φ are the spherical coordinates, l and m are the angular momentum, a is the exponent, and y_{lm} is a spherical harmonic.

Several different types of basis sets are minimal basis sets, split valence basis sets, polarized basis sets, diffuse functions, and plane-wave basis sets[50].

The Minimal basis set uses a minimum number of basis functions to describe each orbital occupied by the electron. The split valence basis sets have two or more sizes but do not allow the change of shape of orbitals, e.g., Gaussian basis set 6-31G[52]. The polarized basis sets allow both shape and size change of orbital by adding polarization functions. For example, they add 'f' functions to atoms (e.g., heavy metals) that have valence 'd' orbitals. Some examples for Gaussian polarized basis sets are 31G(d) and 6-311G(d, p) which are equivalent to Double Numerical polarization (DND) and Double Numerical plus Polarization (DNP), respectively in $DMol^3$ [53][54]. Another type of basis set is a diffuse function which are large functionals of s and p orbitals and denoted by '+' sign, e.g., Gaussian basis set 6-31G(d)+[55][54].

In addition to the above-mentioned basis sets, another kind of basis set exist, which is not based on atomic positions, known as plane-wave basis sets. These provide smooth convergence to the periodic systems and do not have a basis set superposition error (BSSE). Although they require pseudo-potentials[51], they save computational time as compared to atom centered basis sets. The Plane-wave method is based on Blöch's theorem which states that electronic wave functions in a periodic structure can be written as a product of two parts i.e. wavelike part and cell-periodic part[56].

$$\Psi_i(r) = \sum_G c_{i,k+G} \exp\left[i(k+G).r\right] \qquad \textbf{Eq. 2-14}$$

where, $\Psi_i(r)$ is the wavefunction of an electron, $c_{i,k+G}$ is the expansion coefficient, which tends to zero when plane waves have high kinetic energy, k is a point in Brillouin zone

(BZ) or wave vector, $G.l = 2\pi m$ is the reciprocal lattice vectors, l is the lattice vector of the crystal and m is an integer.

Practically, the plane-wave basis set is truncated up to the cut off energy(kinetic) provided and called a finite basis set[57]. In this work for 13 atom cluster studies, the DND and DNP basis sets were used as employed by DMol^{3}while for the bigger size cluster, and the plane-wave basis set was used.

2.2.5 K-point Sampling

With the use of Blöch's theorem, calculations have to be performed within the periodic cell at an infinite number of k points that can be computationally expensive[58]. For practical applications, to sample the reciprocal space, a finite number of k points can be used within the first BZ[59]. The electronic wavefunction at closely located k points are similar, hence we can reduce the number of k points. Some approximations to sample the k points are methods by Monkhorst & Pack[60], Chadi & Cohen[61], and Baldereschi[62]. The error in calculating the properties was removed by using denser k points. In the case of metals, as some bands are not fully occupied, sampling the k-space around the Fermi surface is difficult due to discontinuities in the $\rho_k(r_0)$ functions (ρ=charge density when k crosses the Fermi surface)[59]. The bigger the system is the smaller number of k points are needed to be used. In this work Γ-point sampling is used for the calculations done in VASP.

2.2.6 Pseudopotentials

A large plane-wave basis set is required if an all-electron calculation is to be performed to expand the wave functions; hence the huge amount of computational time is needed[57]. In solids, most of the properties are determined by valence electrons instead of the tightly bound core which is closer to the nucleus. Based on this fact, the pseudopotential

approximation[63] was developed which freezes the core electrons and replaces the Coulomb potential with the effective ionic potential[64]. Several types of pseudopotential approximations exist such as the projector augmented waves (PAW)[65][66], ultrasoft pseudopotentials[67], norm-conserving pseudopotentials[68]. In this work, Effective core potentials ($DMol^3$) and PAW potentials (VASP) are used.

2.2.7 Transition State Theory

Transition State Theory (TST), developed by Eyring, Evans, and Polanyi in 1935[69], is based on collision theory. The reactant and product are at the global minima on the potential energy surface, and the first-order saddle point on the minimum energy path (MEP) connecting them is called the transition state. According to TST, a transition state exists between the reactant and product pathway, and the corresponding energy and structure are called transition state energy and transition state structure, respectively. The transition state complex(structure) is found on the MEP on the PES connecting reactant and products. TST helps to calculate standard enthalpy, standard Gibbs energy of activation, and standard entropy of activation. Several methods to find the transition state structure on the PES are the nudged elastic band (NEB)[70], climbed-image nudged elastic band (CI-NEB)[71], synchronous transit methods, etc. In this work, synchronous transit methods and CI-NEB are used, employed in DMol3 and VASP, respectively.

Synchronous Transit Methods

In synchronous transit methods, a Linear synchronous transit (LST) and Quadratic synchronous transit method (QST) is used to find out the transition state. LST method uses linear interpolation on the PES to find a maximum energy structure; further, QST is used to refine the TS using conjugate gradient minimization. After searching the transition state

structure, TS optimization is performed using eigenvector following method (based on Newton-Raphson method)[72] in which the Hessian matrix, along with one normal mode, is calculated to search for maximum energy[73].

Nudged Elastic Band Method

In the NEB method, the intermediate structures are bonded with springs to provide a constraint to stay between reactant and products and behave as an elastic band. NEB calculation finishes when the sum of the force components perpendicular and along the reaction path is zero[70]. Later, an improved (from NEB) method, CI-NEB, was developed by Graeme Henkelman in which the point(configuration) is not affected by the spring force of nearby points. In CI-NEB, once the highest energy image on the elastic band is found, the forces (only along with the inverted elastic band) on the image make it move up to the potential energy surface. CI-NEB requires lesser numbers of images between reactant and product and does not require any additional computational time unlike the NEB method[70].

2.3 Computational Software

The software used in this study for quantum mechanical calculations is discussed here. The detailed procedure to calculate energies, parameters, and settings are given for each software used.

2.3.1 DMol^3

DMol^3 is a modeling and simulation software to predict, understand, and analyze molecular structure, properties, and behavior of molecules or a group of molecules[35]. Firstly, we geometry optimized icosahedral pure and bimetallic (core-shell) 13 atom clusters of Ru, Pd, and Pt. Bimetallic structures were created by replacing the core atom

with a different metal (Pd, Pt, Fe, Ru, Ni, and Co). Ground state energies of all the systems (clusters, CO adsorbed clusters. clusters with CO bond broken) were performed using RPBE in combination with the DND and DNP (for comparison purposes) with the ECP basis sets. Atomic coordinates were relaxed until the energy change between steps is less than $2 \times 10^{-5}\, Ha(Hartree)$ and Hellmann-Feynman forces were less than $0.004\, Ha\, \text{Å}^{-1}$. The energy barrier was obtained by doing the transition state search using LST/QST methods[74]. Vibrational frequency calculations were performed to confirm the ground states and transition states. Additionally, ZPVE corrections were considered in all calculations.

2.3.2 VASP

Due to limitations of computational resources, icosahedral pure and bimetallic 55 atom cluster calculations were done using periodic boundary conditions as implemented in VASP. Core treatment of electrons was done using the projector augmented wave-functions (PAW) and ultra-soft pseudopotentials. The plane-wave energy cutoff of $400\, eV$ (more than ENMAX in POTCAR file) was used for each metallic system. A periodic box with an edge length of 25 Å was used to provide enough vacuum space between the cluster images. All atoms in the pure and bimetallic clusters were allowed to relax until the forces on all atoms were less than $0.02\, eV\ \text{Å}^{-1}$. The transition state search was done by employing the CI-NEB method. The formulae used in calculations are mentioned in the specific chapter's computational details.

2.3.3 Vesta

To see the charge density difference, Vesta was used, which is a 3D visualization program of crystal structures and charge densities[75].

CHAPTER 3

RESULTS – PURE AND BIMETALLIC 13-ATOM CATALYST MODELS

3.1 Pure and Alloyed Ru, Pd and Pt Nanoclusters

In this chapter, the smallest magic number nanoclusters containing 13 atoms were used as the catalyst models to explore the initial steps of FT catalytic activity. Pure and binary (core-shell) combinations of Ru, Pd, Pt were considered in making nano-catalyst models in a core(1)-shell(12) arrangement of 1 atom of either Co, Fe, Ni, Ru, Pd, or Pt in the core, and 12 atoms of either Ru, Pd, or Pt in the shell.

3.2 Computational Details

All DFT calculations were performed using the Dmol^3 module in Materials Studio 6.0 software. The GGA-RPBE exchange-correlation functional was used to study electronic structures. This method was used in combination with the Double Numerical plus polarizing functions (p- and d-) on heavy atoms basis (DND), and effective core potential (ECP). All energies reported in this work include Zero-point energy corrections.

The cluster binding energy per atom (cohesive energy) is calculated according to **Eq. 3-1** for pure (Ru, Pd, or Pt), and **Eq. 3-2** for binary (A_1B_{12} with A= Co, Ni, Fe, Ru, Pd, Pt, B = Ru, Pd, Pt, and A ≠ B) nanoclusters.

$$E_b(M_{13}) = \frac{[13 * E(M) - E(M_{13})]}{13} \qquad \textbf{Eq. 3-1}$$

where, $E_b(M_{13})$ is the binding (cohesive) energy of the 13-atom pure M metal (M = Ru, Pd, or Pt) cluster,

$E(M_{13})$ is the total energy of the 13-atom pure M metal cluster, and

$E(M)$ is the total energy of the metal atom M.

$$E_b(A_1B_{12}) = \frac{[1 * E(A) + 12 * E(B) - E(A_1B_{12})]}{13} \qquad \textbf{Eq. 3-2}$$

where, $E_b(A_1B_{12})$ is the binding (cohesive) energy of the A_1B_{12}bimetallic core(A)-shell(B) nanoclusters containing $13 = 1 + 12$ total number of atoms,

A and B are any two elements where, A= Co, Ni, Fe, Ru, Pd, or Pt, B = Ru, Pd, or Pt, and A ≠ B

$E(A)$ and $E(B)$ are the energies of one atom of the A and B metals, respectively, and 1 and 12 are the total numbers of atoms of A and B ,respectively in an A_1B_{12} core-shell arrangement. For instance, a cluster having 1 atom of Ru in the core and 12 atoms of Pd in the shell will be denoted as Ru_1Pd_{12}.

$E(A_1B_{12})$ is the total energy of binary metal clusters containing 1 atom in the core of type A and 12 atoms in the shell of type B metal.

The Excess energy, E_{exc}, was calculated using **Eq. 3-3** to compare the thermodynamic stability of binary clusters as compared to each other.

$$E_{exc} = \frac{\left[\frac{1}{13}E_c(A) + \frac{12}{13}E_c(B) - E(A_1B_{12})\right]}{13} \qquad \textbf{Eq. 3-3}$$

$E_c(A)$ and $E_c(B)$ are the total energies of the pure clusters containing A and B type metal, respectively.

A positive value of E_{exc} indicates the binary nanocluster is thermodynamically more stable than the respective pure nanocluster.

3.3 Structural Stability of Nanoclusters

Geometry optimized structures of pure Pd, Ru, and Pt nanoclusters are shown in Figure 3 1. The ground state palladium cluster showed a distorted Mackay Icosahedron geometry with D3d symmetry. The ground state ruthenium nanocluster has decahedral geometry with D5h symmetry, whereas the platinum cluster initial symmetry changed to a layered prism-like structure. These calculated ground-state configurations are considered the most common 13-atom transition metal clusters in the literature[76].

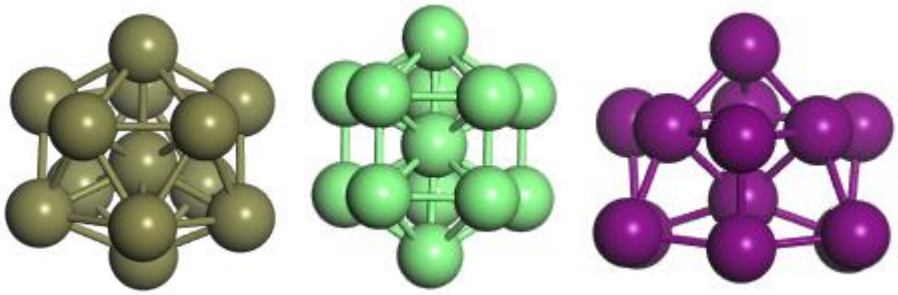

Pd_{13} Ru_{13} Pt_{13}

Figure 3-1: Geometry optimized 13 atom pure nanoclusters of Pd, Ru, and Pt shown in olive, green, and purple.

There are many structural isomers of pure and bimetallic clusters that can have comparable total energies. Geometry optimizing the isomers with frequency analysis can guide towards finding the global minimum. Vibrational frequency analysis of each optimized structure was done to ensure the ground state conformations were reported in this work.

In **Figure 3-2** the ground state geometries of 13-atom A_1B_{12}bimetallic core(A)-shell(B) nanoclusters optimized at the RPBE/DND theory level are presented. When Pt is the host (shell) element, bimetallic combinations showed slightly modified structures as compared to the pure Pt_{13} cluster (Figure 3-1). In the case of Ru as the host element, all combinations except Fe_1Ru_{12} favored the geometry found for the pure Ru_{13} cluster. Interestingly, the Fe_1Ru_{12} nanocluster showed the Mackay icosahedral symmetry. Finally, when Pd was the host element, all the A_1Pd_{12} (A = Co, Ni, Fe, Ru, Pd, or Pt) nanostructures showed a distorted Mackay icosahedron geometry, similar to the pure Pd_{13} cluster (Figure 3-1).

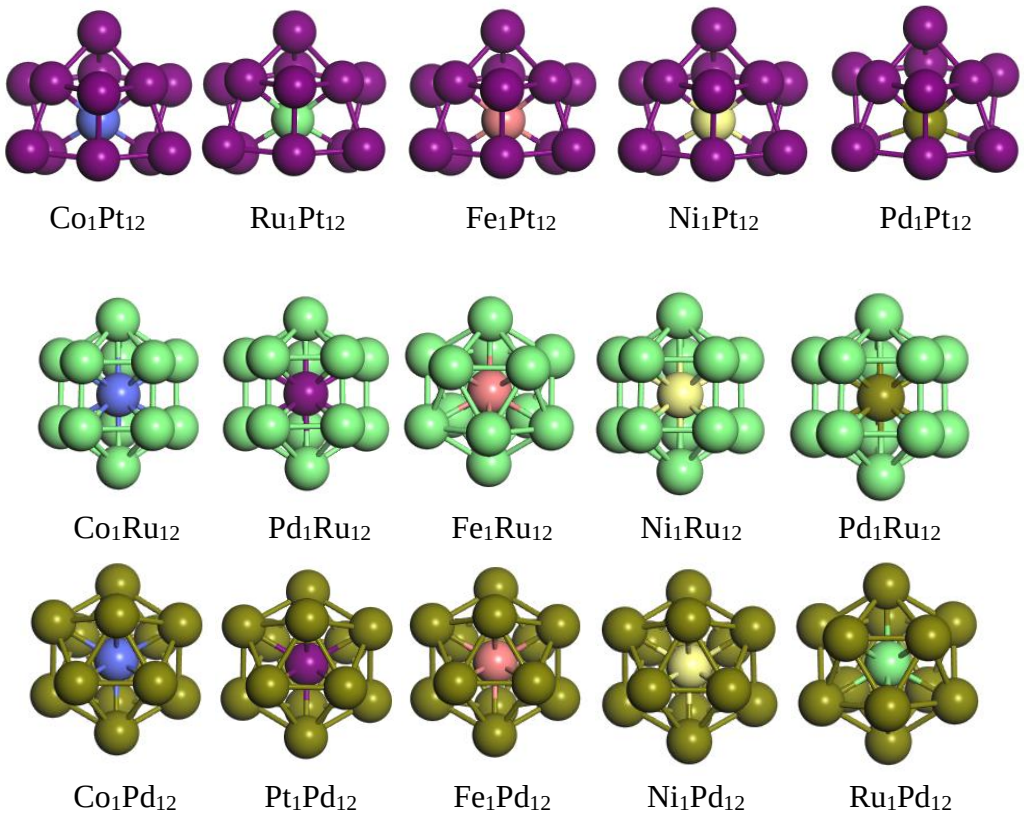

Figure 3-2: Ground-state geometries of 13-atom A_1B_{12}bimetallic core(A)-shell(B) nanoclusters optimized at the RPBE/DND theory level. Ru, Pd, Pt, Ni, Co, and Fe are shown in green, olive, purple, yellow, blue, and pink, respectively.

The GGA-structural stability of the pure and binary nanoclusters was also explored using the RPBE exchange-correlation functional in combination with the Double Numerical plus polarization (s-, p- and d-) on all atoms (DNP) basis set, and effective core potential (ECP). **Figure 3-3** shows the ground state geometries of pure Pt_{13} and bimetallic A_1Pt_{12} (A = Co, Ni, Fe, Ru, or Pd) nanoclusters optimized at the RPBE/DNP theory level. Given that the DNP basis set is like DND, but includes a polarization s-function on all atoms, it is interesting to note that these pure Pt_{13} and bimetallic A_1Pt_{12} (A = Ru, Pd, and Pt) geometries are different from those optimized at RPBE/DND theory level (Figures 3-1 and 3-2). All these clusters showed a distorted Mackay Icosahedron geometry with D3d

symmetry when DNP is used. The ground state geometries of the nanoclusters in which the shell elements are Ru or Pd, however, stayed the same as those shown in **Figure 3-1** and **Figure 3-2** when optimized at RPBE/DNP theory level. The difference in ground-state geometries for Pt-based clusters may be due to the effect of polarization on the $6s^1$ unpaired electron of Pt.

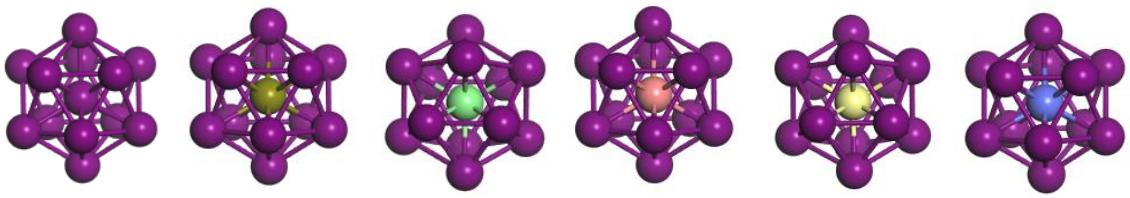

Pt_{13} Pd_1Pt_{12} Ru_1Pd_{12} Fe_1Pt_{12} Ni_1Pd_{12} Co_1Pt_{12}

Figure 3-3: Geometry optimized 13 atom pure and bimetallic A_1Pt_{12} (A = Ru, Pd, and Pt) nanoclusters at the RPBE/DNP theory level. Pt, Ru, Pd, Co, Fe, and Ni are shown in purple, green, olive, blue, pink, and yellow, respectively.

3.3.1 Binding (Cohesive) Energy of Binary Nanoclusters

Among the pure clusters, as we can see in Figure 3-4 Ru_{13} shows the strongest cohesive energy followed by Pt_{13} and Pd_{13}. The cohesive energy of Pd_{13} can be improved by adding Ru (best case), then Fe, Co, Ni, and finally Pt in the core of the Pd-based cluster. In the case of Ru_{13}, the cohesive energy deteriorates by adding Co, Ni, Pt, and Pd but improves considerably by replacing the central atom with Fe (**Figure 3-4**). We have also plotted the comparison of cohesive energies of pure 13 atom clusters when calculated at DND, DNP, and Plane wave basis sets (implemented in VASP). The cohesive energies were calculated using **Eq. 3-1**.

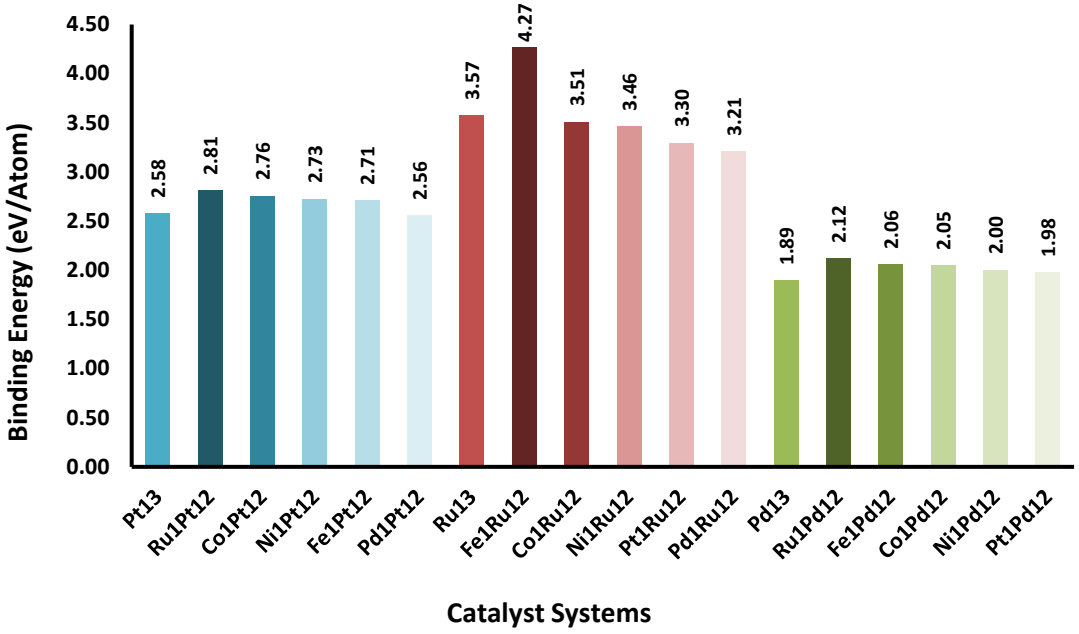

Figure 3-4: Binding (Cohesive) Energies of 13-atom pure and binary nanoclusters (calculations performed at the GGA/RPBE/DND level). Colors indicate clusters families (Pt-based, Ru-based, and Pd-based clusters are shown in blue, red, and green shades, respectively).

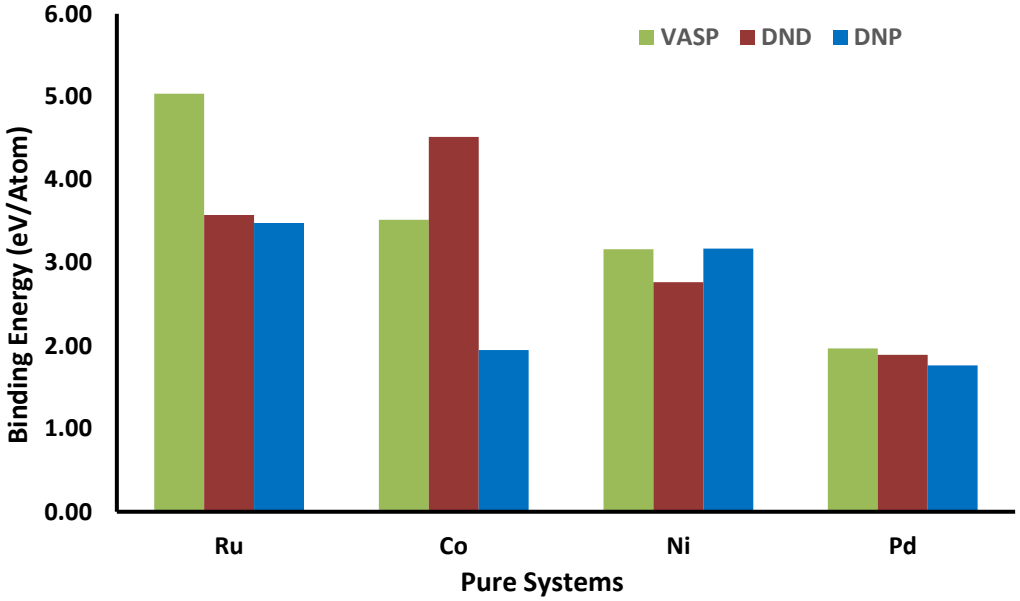

Figure 3-5: Comparison of Binding (Cohesive) Energies of 13-atom pure nanoclusters performed at the DND, DNP, and plane-wave basis set.

In **Figure 3-5** the comparison of binding energy values for pure clusters calculated using plane-wave basis set, DND and DNP is given. The calculation using plane-wave basis sets showed the highest binding energy for Ru 13 -atom cluster followed by Co, Ni, and Pd. All three basis sets showed that atoms in Pd cluster are weakly bonded to each other as compared to all other metal clusters explored.

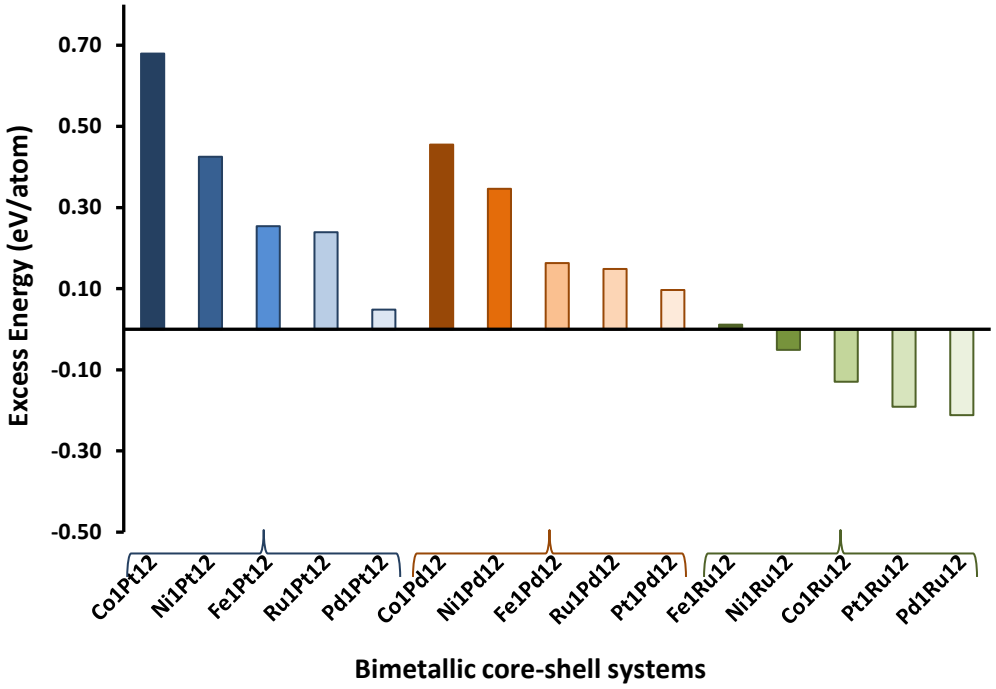

Figure 3-6: Excess Energies of 13-atom binary nanoclusters. Calculations were performed at the GGA/RPBE/DNP theory level.

The excess energies of binary nanoclusters were calculated using **Eq. 3-3** and are shown in **Figure 3-6**. These excess energies are calculated in reference to the pure Pd, Ru, and Pt clusters (zero for pure clusters), respectively, depending on the metal family under consideration. For instance, the binary clusters having Pt in the shell with other elements in the core (Ru, Pd, Co, Ni, and Fe), the excess energy was taken with respect to Pt (zero for pure Pt cluster). The addition of Co, Ni, Fe, Ru, and Pd increases (best to worst) the

excess energy of Pt-based nanoclusters. The addition of Co, Ni, Fe, Ru, and Pt (best to worst) increases the excess energy of Pd-based nanoclusters.

In the case of Ru-based nanoclusters, however, the addition of Fe increases the excess energy of Ru-based nanoclusters, while the addition of Ni, Co, Pt, and Pd (increasing order) in its core deteriorates it. It is interesting to note that, when Pt and Pd are the shells, the maximum cohesive energy was noted when Ru was added to the core of the cluster**.**

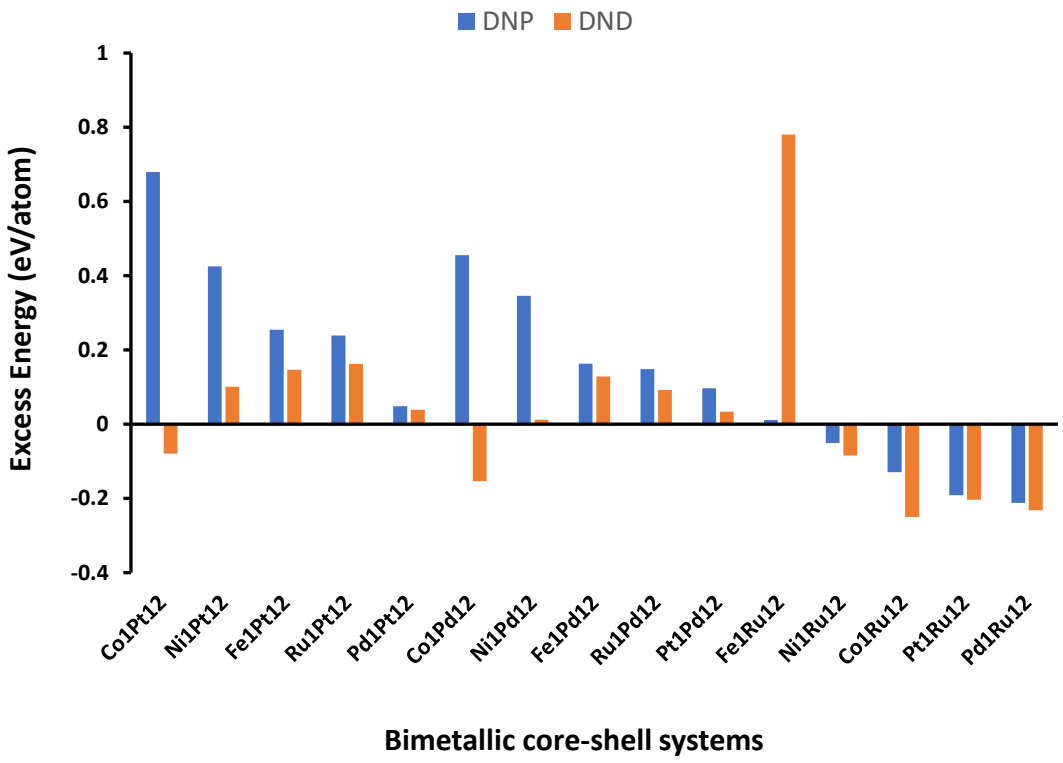

Figure 3-7: Comparison of Excess Energies of 13 atom binary nanoclusters between DND and DNP.

Figure 3-7 shows the comparison of excess energy values calculated using either DND or DNP basis sets. For clusters with Co, in the core, the DND basis set shows negative excess energy as opposed to those when the DNP basis set is used. For the Fe_1Ru_{12} cluster,

the excess energy obtained using DND shows an exceptionally high value. The comparison of excess energies in the case of the Pt cluster might not give a clear idea due to the different geometry of Pt nanoclusters in both cases (icosahedron/layered prism).

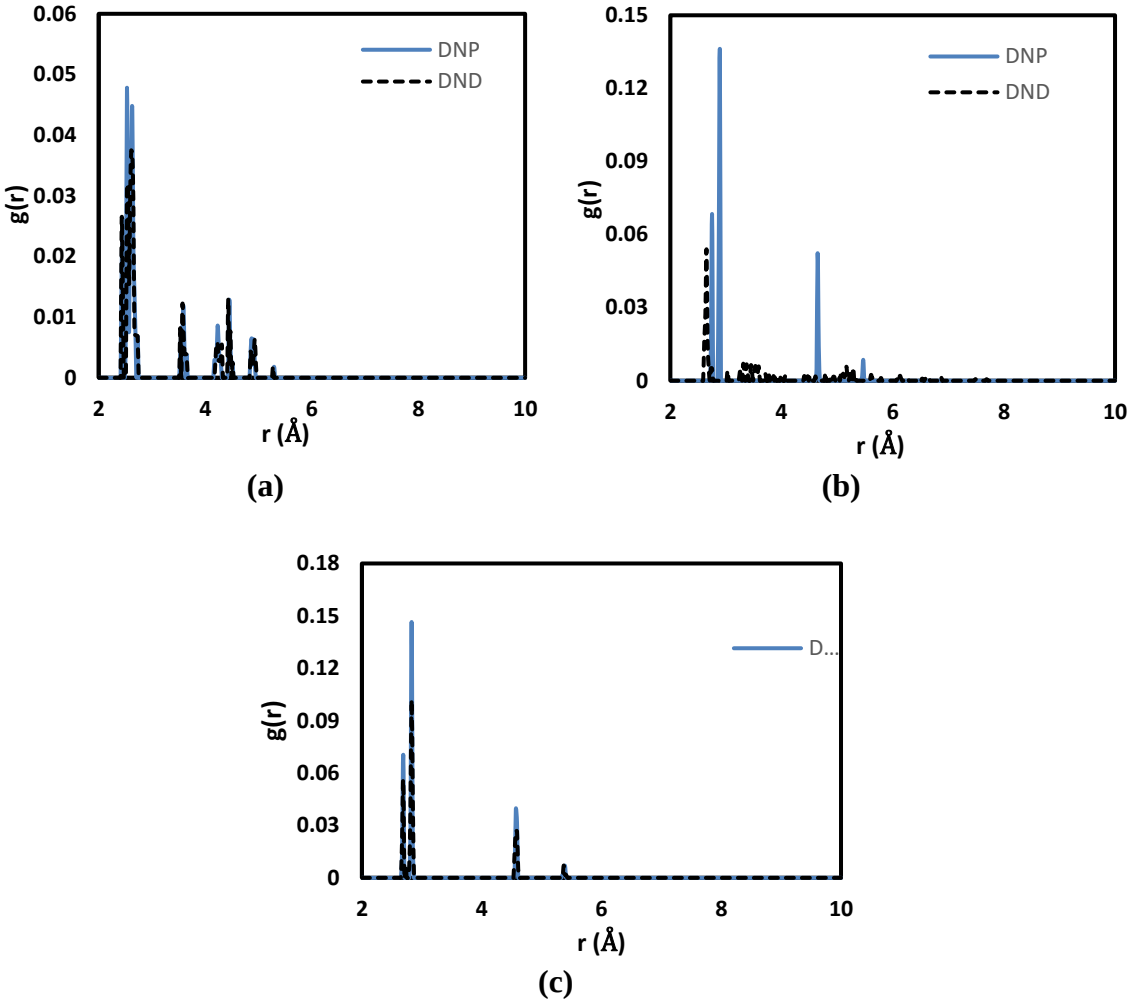

Figure 3-8: Plots of Radial distribution function $g(r)$, relative to the center of geometry of 13 atom pure clusters at DND and DNP both theory level. (a), (b) and (c) are for Ru, Pt, and Pd respectively.

The radial distribution function for the metal-metal distances in pure 13-atom clusters is shown in **Figure 3-8** to see if there is any significant change in the geometry of the clusters optimized using DND and DNP basis sets. For Ru and Pd clusters, there was

no significant change observed between the nearest neighbor's distance (**Figure 3-8 (a)** and **c**). However, for the Pt cluster, there was a change in geometry observed when using the DNP level which is different from the regular icosahedron structure, as explained in section 3.3. Hence, for the Pt cluster, the RDF plot at DND showed peaks for Pt-Pt distances at different places than those at the DNP theory level (**Figure 3-8 c**). Pt nanoclusters of small sizes (<1.5 nm) are known to arrange the atoms in a more compact manner and are sensitive to the basis sets used; hence the geometry gets distorted [76]–[78].

CHAPTER 4

RESULTS – CO ADSORPTION AND DISSOCIATION ON 13-ATOM CLUSTERS

4.1 Computational Details

After finding the ground state conformations of pure and binary 13-atom nanoclusters, CO adsorption was studied on all available sites of the nanoclusters, and finally, the CO bond breaking on the surface of the nanocatalysts (dissociative adsorption of atomic C and O species) was investigated.

All DFT calculations were performed using the Dmol^3 module of the Materials Studio 6.0 software. The GGA-RPBE exchange-correlation functional was used to study electronic structures in combination with the Double Numerical basis set (DND) and effective core potential (ECP). All energies reported in this work include Zero-point energy corrections. The CO binding energy values were also calculated at the RPBE/DNP theory level, keeping all other settings unchanged.

To ensure local minima and transition state, harmonic vibrational frequency analysis was done. To study transition states (TS), LST/QST method was used, and TS was confirmed by obtaining only one imaginary frequency.

The binding energy of CO, $E_{ads}(CO)$, upon CO binding on the surface of the metal nanoparticle was calculated using **Eq. 4-1**.

$$E_{ads}(CO) = E(CO^*) - E(M) - E(CO) \qquad \textbf{Eq. 4-1}$$

where, $E(CO^*)$ is the energy of the cluster with one CO molecule adsorbed on its surface,

$E(M)$ is the energy of the metal cluster, and

$E(CO)$ is the energy of a single CO molecule.

According to Eq. 4-1, negative binding energy corresponds to a stable CO binding on the cluster surface. The energy barrier for CO binding was calculated by subtracting the total energy of the reactant (nanocluster with one CO adsorbed) from that of the transition state. The transition state is the highest point on the lowest energy path connecting the reactant and product (CO split on the nano catalyst surface).

4.2 CO Adsorption

CO adsorption was studied using **Eq. 4-1** on pure and binary systems. Three adsorption sites were investigated in all the clusters. According to **Figure 4-1**, the more negative the E_b, the stronger the CO adsorption is.

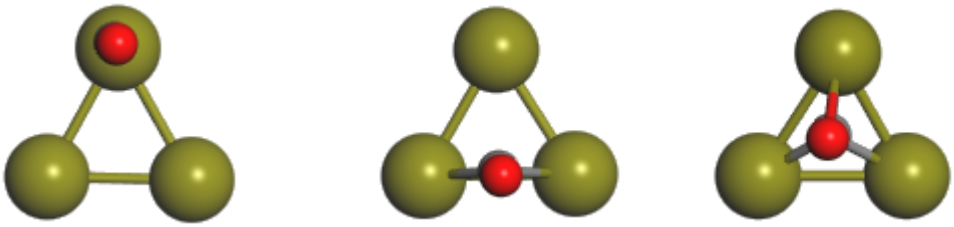

Figure 4-1: Different CO adsorption sites illustrated on a 3-atom metal cluster (CO adsorbs vertically, with C (gray) closer to the metal surface. Oxygen is shown in red.

When CO gets adsorbed vertically on a metal atom, it is called the top absorption site. Adsorption of CO between two metal atoms is considered a bridge adsorption position, and among three metal atoms, it is called a hollow adsorption site. On the Ru_{13} cluster,

there were 7 adsorption sites instead of 3 due to its decahedral geometry. **Figure 4-2** shows one top, two bridge, and one 4-fold hollow sites, in addition to the three adsorption sites shown in **Figure 4-1**.

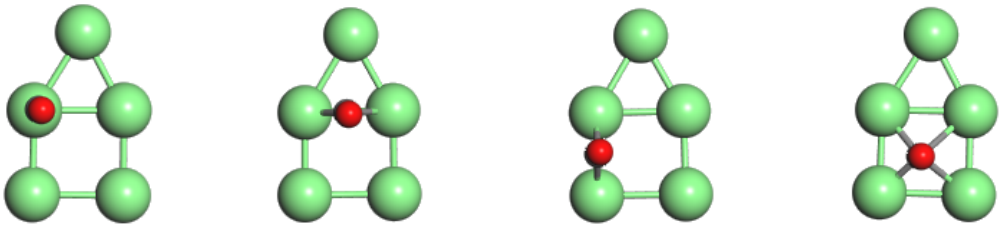

Figure 4-2: Different CO adsorption sites illustrated on a 3-atom metal cluster (CO adsorbs vertically, with C (gray) closer to the metal surface. Oxygen is shown in red.

For both DND and DNP basis sets, all the above mentioned CO adsorption sites in **Figure 4-1** and **Figure 4-2** were explored. Among the pure clusters, the strongest CO adsorption was found on the top site of the Ru_{13} cluster, followed by the top site of Pt_{13}, and the Pd_{13} hollow site. Ru has also shown to form stable carbides in previous studies[79], which resembles our observation of the CO binding energy to be the highest as compared to Pd and Pt nanoclusters. The CO adsorption energies were found to be -2.16, -1.83, and -1.36 eV on Ru_{13}, $Pt_{13,}$ and Pd_{13}, respectively, at the RPBE/DND theory level (Table 4-1). It has been found in experimental studies that hollow and top sites are preferred for CO adsorption on the Pd (111) and Pt (111) surfaces, respectively, in small as well as large nanoclusters[80] in agreement with our findings. The calculated CO adsorption energy on the PAS of the Pd cluster compares well (± 0.01 eV) with the theoretical studies done by Pedersen et al. on Pd (111) surfaces using the RPBE theory[48].

Table 4-1: CO adsorption Energies (E_{ads}) on all active sites (Top, Bridge and, Hollow), Preferred adsorption site(PAS), binding energy values associated with the PAS (highlighted green), and CO bond-breaking energies ($E_{barrier}$) for the breaking of the CO bond from its PAS on pure and binary nanoclusters. Calculations were performed at the RPBE/DND theory level.

System	Adsorption sites/E_{ads} (eV)			PAS	$E_{barrier}$ (eV)
	Top	Bridge	Hollow		
Ru	-2.16/1.79	-1.84/1.71/-1.83	-1.77	Top	1.35
Pd	-1.21	-1.31	-1.36	Hollow	1.34
Pt	-1.83	-1.39	-1.22	Top	4.76
Pd_1Ru_{12}	-3.27	-2.66	-2.74	Top	-
Pt_1Ru_{12}	-3.51	-4.88	-3.53	Top	-
Co_1Ru_{12}	-2.03	-1.55	-2.04	Hollow	-
Ni_1Ru_{12}	-2.22	-1.73	-1.66	Top	-
Ru_1Pd_{12}	-1.15	-1.29	-1.37	Hollow	-
Pt_1Pd_{12}	-1.29	-1.34	-1.42	Hollow	-
Fe_1Pd_{12}	-1.02	-1.24	-1.23	Bridge	-
Co_1Pd_{12}	-0.88	-0.80	-0.74	Top	-
Ni_1Pd_{12}	-1.17	-1.30	-1.32	Hollow	-
Pd_1Pt_{12}	-1.75	-1.51	-1.51	Top	-
Ru_1Pt_{12}	-1.53	-1.44	-1.44	Top	-
Fe_1Pt_{12}	-1.70	-1.39	-1.38	Top	-
Co_1Pt_{12}	-1.40	-1.39	-1.37	Top	-
Ni_1Pt_{12}	-1.70	-1.40	-1.39	Top	-

All these calculations were repeated and performed at the RPBE/DNP theory level while keeping all the other settings unchanged with respect to the calculations using the DND basis set. The corresponding results can be found in **Table 4-2**. Error! Not a valid bookmark self-reference. shows the comparison of CO binding energy values on the cluster calculated using either DND or DNP basis set. The CO binding energies calculated using the DNP basis set show a difference of ~1 eV for Pd_1Ru_{12} and Pt_1Pt_{12} when comparing with the corresponding ones calculated using DND. Interestingly for $Fe_1Pt_{12,}$ the CO binding energy is ~3 eV higher when calculated with DNP as compared to DND. For the rest of the systems, the binding energies are in ± 0.5 eV range when calculated with DND and DNP basis sets.

Table 4-2: CO adsorption Energies (E_{ads}) on all active sites (Top, Bridge and, Hollow), Preferred adsorption site(PAS), binding energy values associated with the PAS (highlighted green), and CO bond-breaking energies ($E_{barrier}$) for the breaking of the CO bond from its PAS on pure and binary nanoclusters. Calculations were performed at the RPBE/DNP theory level.

System	Adsorption sites/E_{ads} (eV)			PAS
	Top	Bridge	Hollow	
Ru13	-2.28/-1.95	-1.93/-1.83/-2.0	-1.91/-2.28	Top/Hollow
Pd13	-1.21	-1.34	-1.65	Hollow
Pt13	-2.12	-1.77	-1.57	Top
Pd_1Ru_{12}	-2.21/0.03	-2.22/-1.91/-1.91	-1.86/-1.27	Bridge
Pt_1Ru_{12}	-2.23/-2.04	-1.89/-2.75/-1.92	-5.70/-5.61	Hollow
Co_1Ru_{12}	-2.30	-1.25	-0.92	Top
Ni_1Ru_{12}	-2.14	-1.68	-1.60	Top
Ru_1Pd_{12}	-1.26	-1.25	-1.22	Top
Pt_1Pd_{12}	-1.51	-1.56	-1.56	Hollow
Fe_1Pd_{12}	-1.23	-1.35	-1.34	Bridge
Co_1Pd_{12}	-1.02	-1.03	-0.97	Bridge
Ni_1Pd_{12}	-1.25	-1.18	-1.26	Hollow
Pd_1Pt_{12}	-2.13	-1.75	-1.56	Top
Ru_1Pt_{12}	-1.90	-1.59	-1.58	Top
Fe_1Pt_{12}	-1.86	-1.79	-1.46	Bridge
Co_1Pt_{12}	-1.63	-1.62 (Top)	-1.17	Top
Ni_1Pt_{12}	-1.84	-1.59	-1.37	Top

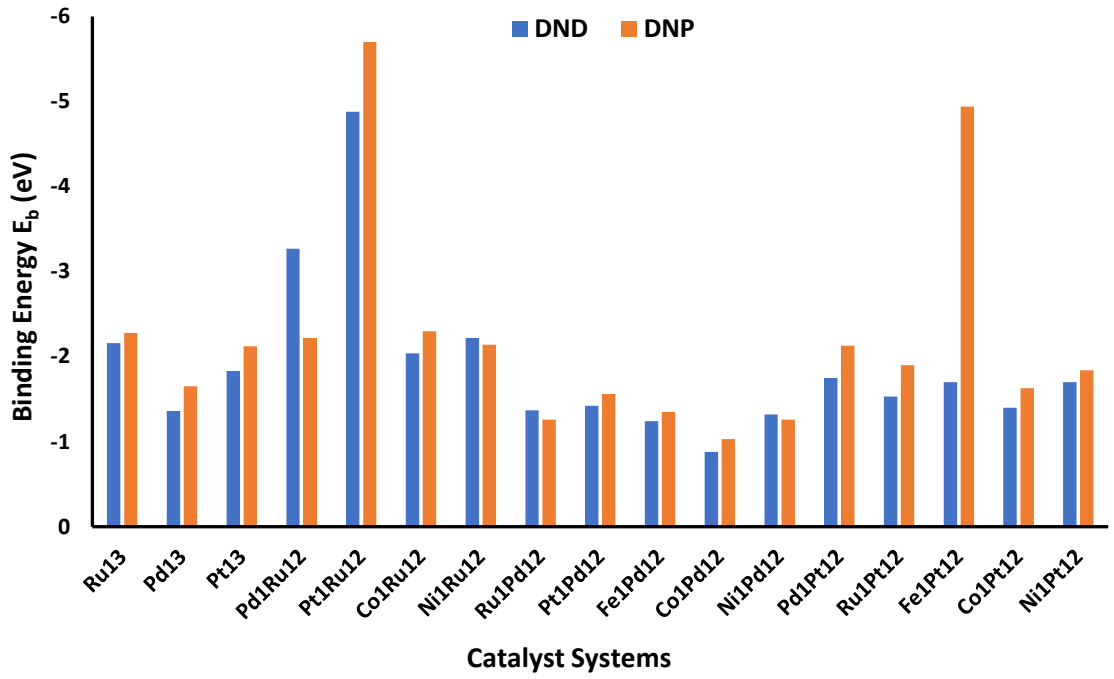

Figure 4-3: Comparison of CO binding energies on the surface of pure and binary metal clusters at the DND and DNP basis set. The Blue and orange bars are for DND and DNP basis sets, respectively.

The ground state structures obtained at the RPBE/DNP theory level, which were found to be different from those found at the RPBE/DND level, are shown in **Figure 4-4**.

Figure 4-4 shows the structures obtained after the geometry optimization of CO adsorbed on hollow, four-fold hollow and bridge sites of Pt_1Ru_{12} nanocluster. In **Figure 4-4 (a)**, when CO got adsorbed on the 2-bridge position, the cluster gains an open geometry as compared to the closed packed decahedral. This phenomenon might be due to the surface energy of the Pt_1Ru_{12} nanocluster. Pt and Ru atoms have comparable sizes, but the surface energy of Pt is lower than that of Ru by 0.41 eV/atom[81].

For the "initial" (CO location at the start of the simulation) hollow site in **Figure 4-4 (b)**, the CO gets adsorb on the top site after the geometry optimization. CO adsorbs in a bridge position after geometry optimization in **Figure 4-4 (c)**, where the initial site of

adsorption was 4-fold hollow. The core Pt atom came to the surface of the nanocluster from its center position upon CO adsorption for both hollow (initial) adsorptions. Similar behavior has been observed in the studies done by Gyawali et al. on Pt_1Fe_{12} nanoclusters[82]. This shows that CO adsorption on any hollow site of the Pt_1Ru_{12} cluster may not be viable, making the cluster chemically unstable. This behavior can be attributed to the high surface energy of the Ru cluster, where it does not prefer to be in a shell. Only lower surface energy metals are stable in the shell in a core-shell conformation[83]. Theoretical studies performed on 55 atom clusters by Mendes et al. on PBE theory level shows the minimum energy structure is where Pt is in the shell of a cluster which has Ru in its shell[83]. We can see from our results that this behavior persists in an even smaller size (~0.5 nm) of the cluster. Therefore, the preliminary studies on 13-atom clusters could help in predicting the catalytic behavior of transition metals.

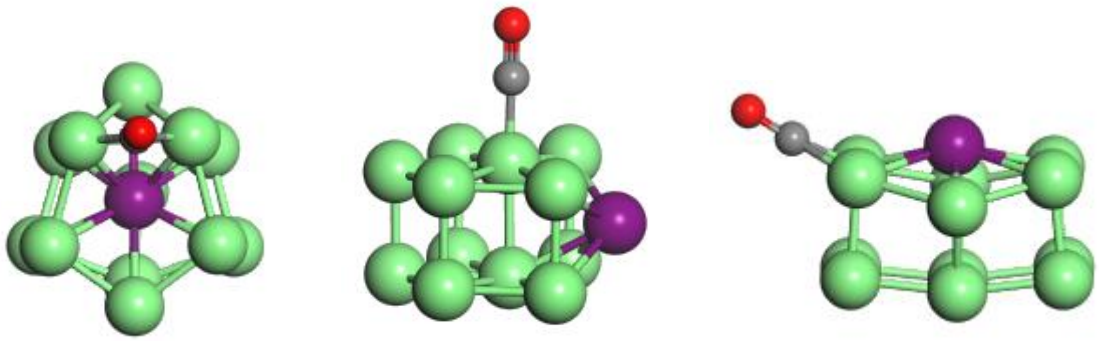

(a) Pt_1Ru_{12} (Bridge) **(b) Pt_1Ru_{12} (initial-Hollow)** **(c) Pt_1Ru_{12} (initial- 4-fold)**

Figure 4-4: CO adsorbed on Pt_1Ru_{12} nanocluster. (a) CO adsorbed on a bridge site (b) CO position changed from initial four-fold hollow to bridge after optimization, (c) CO position changed from initial hollow site to top after optimization. Pt, Ru, C, and O are purple, green, grey, and red, respectively.

4.3 CO Bond Breaking on Pure Clusters

The CO breaking reaction on the pure and bimetallic clusters, from when CO is adsorbed on the preferred adsorption site, is shown in **Figure 4-5**. Transition state structures along with reactants (CO bonded to the surface of the cluster at the PAS) and products (CO bond breaking on the surface of the cluster) are shown for pure 13 atom clusters. All the transition state geometries were confirmed to have only one imaginary frequency.

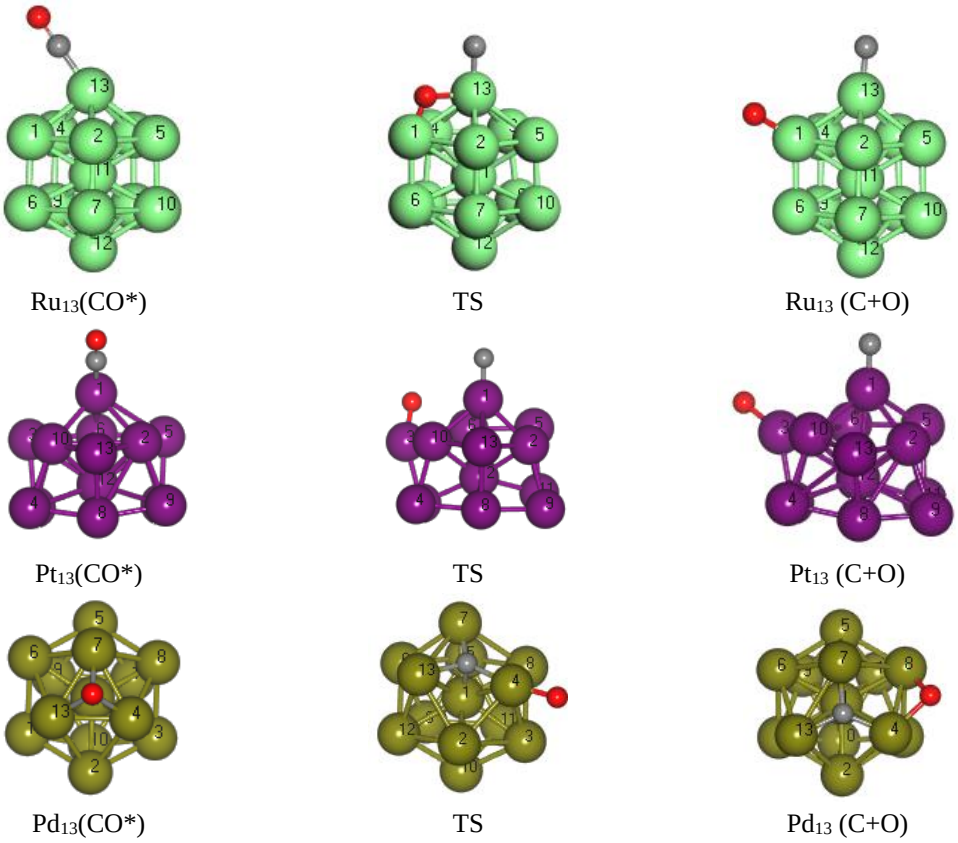

Figure 4-5: CO dissociation pathway on pure nanoclusters. The first picture in each set corresponds to the cluster with CO adsorbed on the PAS, the middle one corresponds to the transition state, and the last pictures show the C and O atomic species (CO dissociative adsorption) absorbed on the metal cluster (C: grey, O: red).

A low energy barrier makes it easier to dissociate (break) the C-O bond on the metal surface. In this work, only the natural potential of the metal clusters to dissociate the C-O bond is presented, i.e., without the assistance of hydrogen.

Figure 4-6 shows a schematic view of the potential energy surface of the reactant, the transition state product, and the barrier energy of the elementary reaction step (CO bond breaking). The reactant needs to overcome the $E_{barrier}$ energy to be able to break the C-O bond on the surface of the cluster.

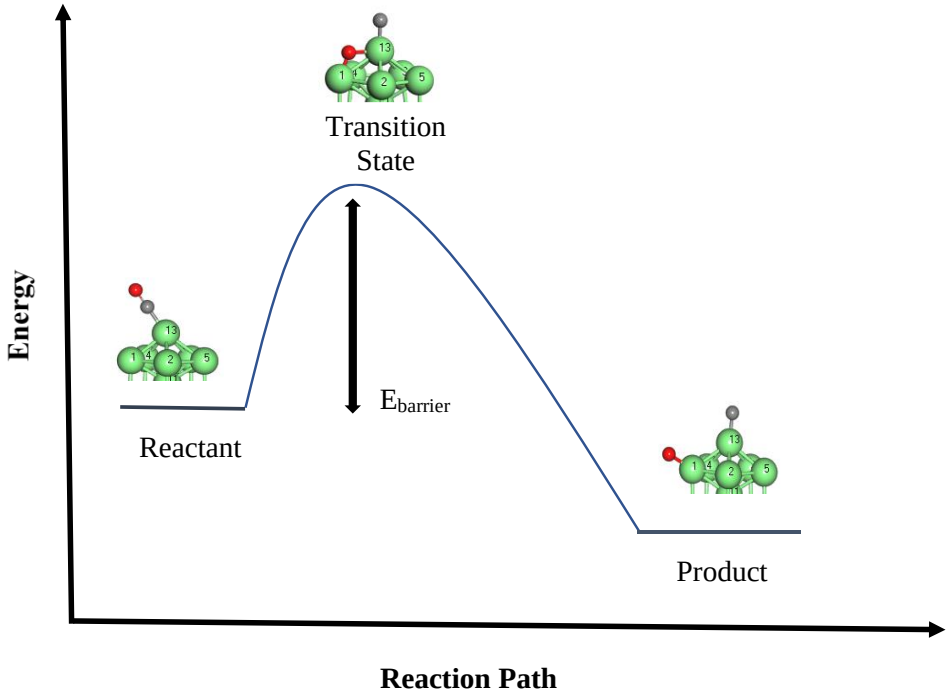

Figure 4-6: One-dimensional schematic representation of the potential energy surface of the reactant, transition state, and the product as well as the associated energy barrier ($E_{barrier}$) over the reaction Path.

4.4 Initial Predictor of Catalytic Activity

We came up with an indicator of the activity of the catalyst to break the CO bond on its surface, which we called the initial predictor (%Diff). The % Diff is shown in **Eq. 4-2** which was identified to evaluate catalyst performance.

$$\%Diff = \frac{[|E_{ads}(CO)| - E_{barrier}(CO)]}{Average[|E_{ads}(CO)|, E_{barrier}(CO)]} * 100 \qquad \textbf{Eq. 4-2}$$

We hypothesize that for the systems for which the % Diff is maximized, there is a better activity towards processes that begin with the CO adsorption followed by the CO bond breaking on the catalyst surface, like the FTS process. We acknowledge, however, that this initial predictor might not be the absolute measure of the performance of the catalyst, as several other factors such as working conditions, the effect of promoters, and support were not studied in this work.

By calculating this quantity for pure clusters, it was found that the %Diff was the highest for Ru_{13} (46%), followed by Pd_{13} (-13%) and it was the lowest for platinum (-88.9%). As reported in previous studies, Ru is known to be the best catalyst for FTS in agreement with our findings. The behavior of Pt in our studies is also in agreement to the current state of knowledge that Pt is easily poisoned by CO and it is very hard to break the C-O bond on its surface; a fact that limits the use of this material as a catalyst for fuel cell applications[84].

The CO bond-breaking studies were done only on pure clusters of small size. On the bimetallic combinations, calculations were done just to see the thermodynamic stability and the CO adsorption strength. Due to their very small size, 13-atom cluster synthesis experimentally is not possible, but they give a good platform to study transition metal catalysis computationally. After the satisfactory preliminary studies were done on

13 atoms, the bigger cluster size containing 55 atoms was studied for CO adsorption and CO bond-breaking potential of the metals and is discussed in the following chapters.

CHAPTER 5

RESULTS – PURE AND BINARY 55-ATOM CATALYST MODELS

By tuning the size, shape, and composition of nanoclusters, we can design new catalysts for different applications[85]. After getting the preliminary results on 13-atom pure and binary nanoclusters, we studied the next magic number nanocluster. These 55-atom nanoclusters are ~1.2 nm in diameter and may be used to better predict the nanoparticle efficiency towards FTS. The Mackay Icosahedron geometry is considered to be the most stable in this size range[30], [31]. Thus, this icosahedral structure of 55-atom nanostructure has one atom in the center, 12 atoms in the inner shell, and 42 atoms on the surface. These can be built by adding 42 atoms in the outside shell of the 13-atom cluster. Layered icosahedron core-shell geometry constructed of twenty equilateral triangles with (111) -like facets make them interesting for catalysis purposes[86]. The vertices and sides of these structures have a higher coordination number than cuboctahedron structures of the same number of atoms in the shell and core[86]. Hence, we have studied icosahedron geometries of the pure and binary 55-atom nanoclusters of Ru, Pd, Ni, Co, Pt, and Fe.

5.1 Computational Details

Spin-polarized Density Functional Theory calculations within the generalized gradient approximation (GGA) formulated by the Revised Perdew-Burke-Ernzerhof [47] exchange-correlation functional were employed in the Vienna ab initio simulation package

(VASP). The interaction between ions and electron was described using the projector-augmented wave (PAW) methods. Plane-wave expansion cutoff energies were set to 400 eV. Nanocluster models were placed in a 25 Å cubic box to ensure enough vacuum gap between two cells. The equilibrium geometries were obtained when the atomic forces were smaller than 0.02 eV/Å with a total energy convergence within 10^{-5} eV. The Methfessel and Paxton's Fermi level smearing[87] was used with Gaussian width of 0.2 eV to accelerate electronic relaxation. The conjugate-gradient algorithm was used to relax the ions. Only the gamma point sampling of the Brillouin zone was done in reciprocal space.

5.2 Structural Stability of Nanoclusters

Highly symmetrical icosahedron pure and core-shell nanoclusters of magic number 55 show the local minimum structure as per theoretical studies done on thermodynamic stability[88]. The binding (cohesive) energy measures the cohesion of atoms with respect to the bulk, or atomization was calculated to explore cluster stability. However, to compare the thermodynamic stability by assessing the mixing of metals in binary core-shell structures with respect to the pure clusters, we calculated the excess energy. The excess energy can be defined as the energy difference upon forming a binary cluster relative to the pure one given the same geometry and size[83]. This was calculated as given in the **Eq. 5-1**.

$$E_{exc} = \frac{\left[\frac{13}{55}E_c(A) + \frac{42}{55}E_c(B) - E(A_{13}B_{42})\right]}{55} \qquad \textbf{Eq. 5-1}$$

E_{exc} is the Excess energy per atom of the binary cluster,

A=13 and B=42 are metal atoms (Ru, Pd, Pt, Ni, Co, and Ni) in the core and shell, respectively,

$E(A_{13}B_{42})$ is the total energy of a binary cluster containing 13 atom in its core and 42 atoms in the shell,

$E_c(A)$ and $E_c(B)$ are the total energies of the minimum energy monometallic 55-atom cluster of the same shape of type A and B, respectively.

A positive value of E_{exc} will indicate the binary nanocluster is thermodynamically more stable than the respective pure nanocluster.

For 55-atom pure and binary systems, the binding energies were calculated by modifying the **Eq. 3-1** and **Eq. 3-2** in CHAPTER 3 according to the number of atoms constituting the clusters, which are 55 in this case.

Eq. 5-2 and **Eq. 5-3** show the binding or cohesive energies of 55 atom pure and binary clusters.

$$E_b(M_{55}) = \frac{[55 * E(M) - E(M_{55})]}{55} \qquad \textbf{Eq. 5-2}$$

$$E_b(A_{13}B_{42}) = \frac{[13 * E(A) + 42 * E(B) - E(A_{13}B_{42})]}{55} \qquad \textbf{Eq. 5-3}$$

where, $E_b(M_{55})$ and $E_b(A_{13}B_{42})$ show the binding energy of 55 atom pure and bimetallic clusters respectively, M = Ru, Pd, Ni, Fe, Co, and Pt,

$E(M_{55})$ is the total energy of 55 atom pure cluster, and

$E(M)$ represents the total energy if isolated metal atom, calculated using the same input parameters.

$E(A)$, and $E(B)$ denotes the energy of an isolated metal atom of type A and B, respectively.

Figure 5-1 shows the ground state conformations of the 55-atom pure and bimetallic nanoclusters.

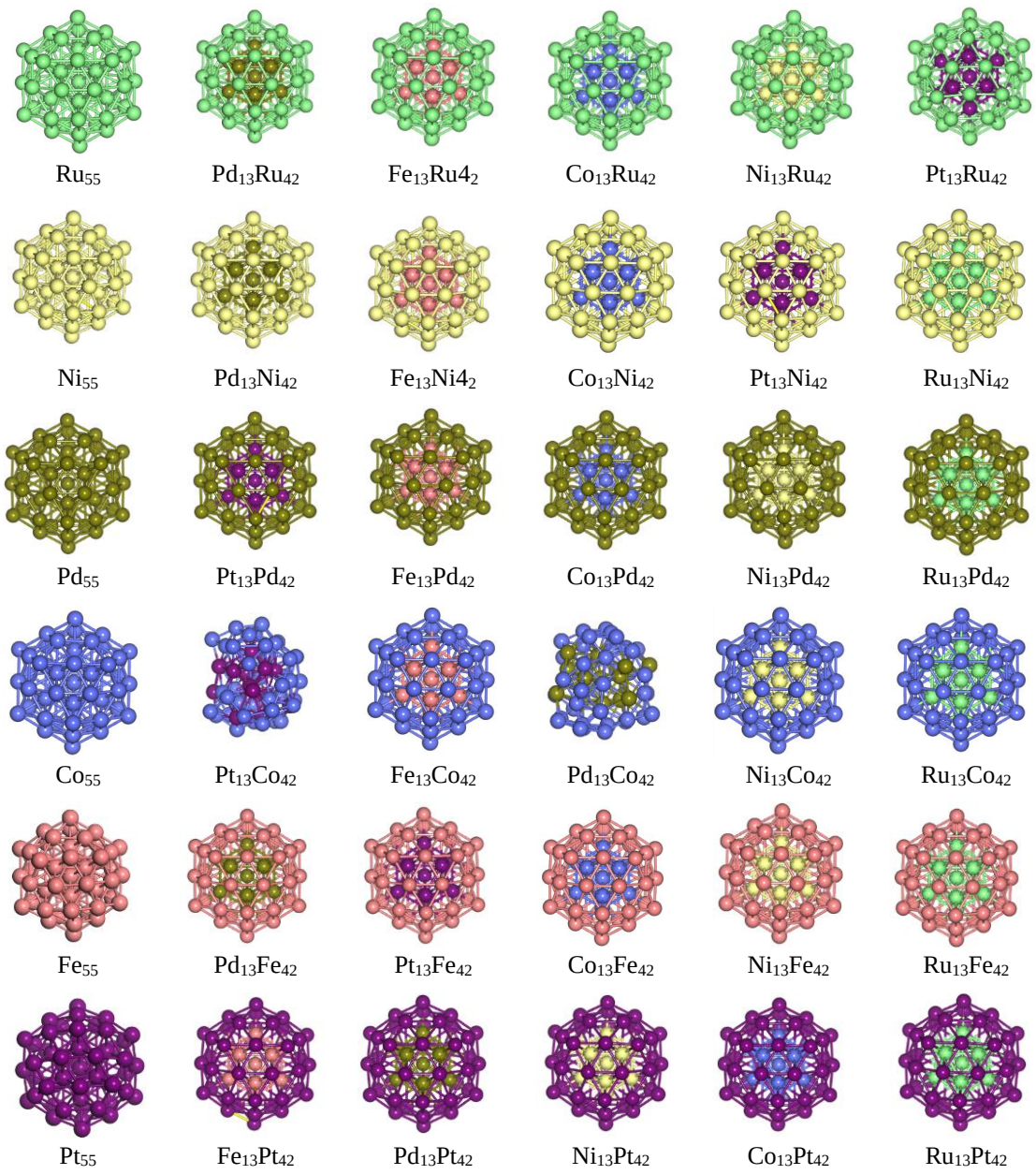

Figure 5-1: Geometry optimized (at the GGA/RPBE theory level in VASP) 55-atom pure and bimetallic nanoclusters. Ru, Pd, Pt, Co, Fe, and Ni are shown in green, olive, purple, blue, pink, and yellow, respectively.

We can see in **Figure 5-1** that the ground state structures of pure clusters have icosahedron geometry. Platinum regained its global minimum structure, which is called

Distorted Reduce Core (DRC), which is in good agreement with theoretical studies done by Batista et al.[89]. Although in this work, only the icosahedron structure of Pt and Fe are considered for comparison with their alloys (icosahedron geometry).

Looking at the geometry of $Pt_{13}Co_{42}$ and $Pd_{13}Co_{42,}$ we can clearly see that the Pt and Pd atoms prefer to segregate to the surface of the Co-based clusters. This can be explained due to the atomic size difference among these three atoms. Atomic radii of Pd and Pt are 11% and 16% larger than that of Co, respectively. In studies done by Mendes et al.[83], Pt atoms at the surface of the cluster have shown a most stable and more symmetrical structure when placed in combinations with lower atomic radii metals.

The excess energy values per atom for the binary clusters calculated using **Eq. 5-1** are given in **Figure 5-2**. Excess energy tells which combination of metals is more thermodynamically stable than others, and the preference of the metals to occupy the shell or the core regions[83].

According to the excess energy calculations, $Fe_{13}Pt_{42}$ was found to be the most stable binary system, followed by the cases where Ru_{13} Co_{13} and Ni_{13} in the core of the Pt-based cluster. The Pd metal tends to decrease the excess energy; hence it is the least favorable if added in the core of any other metal clusters in our studies. All the binary systems made with the host Pd metal showed greater excess energy than the pure Pd_{55} cluster. Ru_{55} has shown to be most stable if compared with the binary systems where the host metal is Ruthenium. The mixing of other metals in the core with Pt in the shell stabilizes the core-shell icosahedron structure than that observed in the pure Pt_{55} cluster.

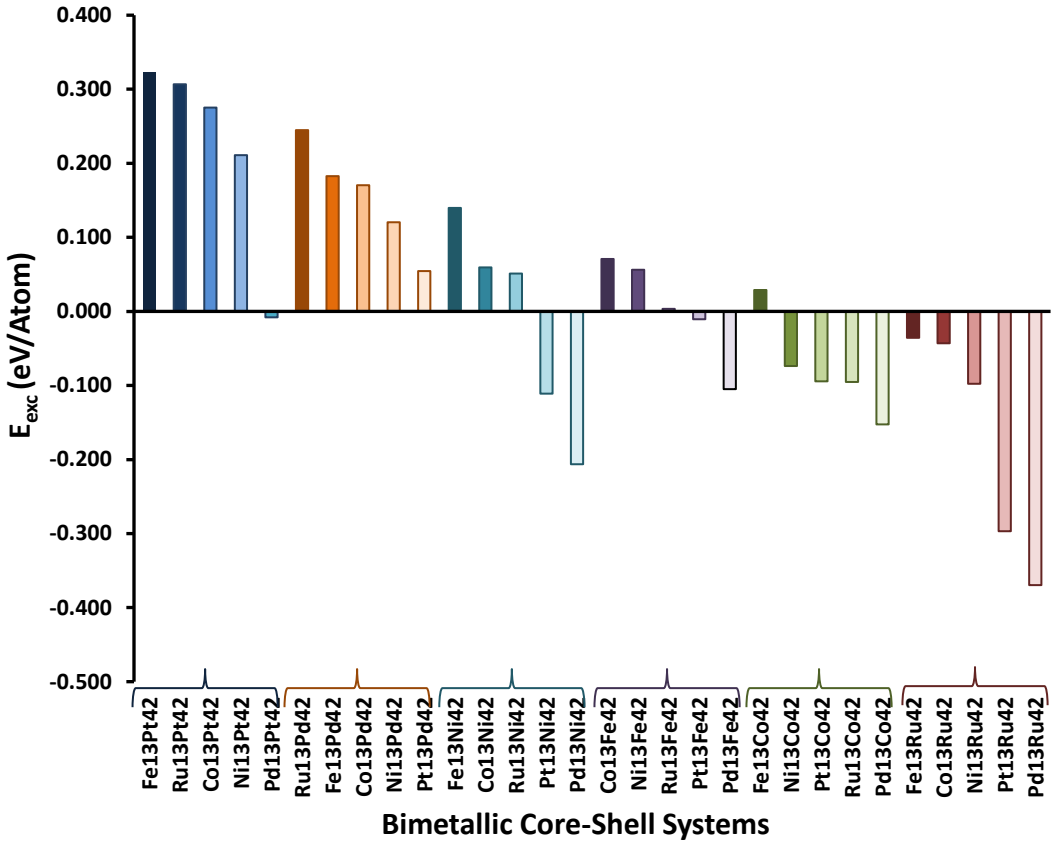

Figure 5-2: Excess energy (eV/atom) vs. binary systems grouped by the family of the same shell element. The calculation was performed at the RPBE theory level with a plane-wave basis set.

The structure where Fe in the core of the Ni cluster has larger excess energy than where the Ni is the core of the Fe cluster. Similar observations were made by Yang et al.[88] for 55 atom clusters at GGA/PBE theory level. Temperature effects were not considered while performing this analysis which might affect the results. We compared our observations to the model suggested by Mendes et al. which relates the structural properties to the atomic radii, surface energy, cohesive energy, binding energy, and electronegativity[83].

We can relate the structural stability and segregation of metal atoms in binary systems based on the size and surface energy of the metal atom. According to the Excess

energy values, the more thermodynamically stable bimetallic combinations are where either Fe or Ru is in the core of the clusters with Pd, Pt, Co, and Ni in the shell. When Fe is the element in the shell, Co in core gives the most stable cluster as compared to other elements in the core. Only based on thermodynamic stability and Fe being cheaper, Fe in the core with expensive metals in the shell can significantly decrease the cost of the catalysts.

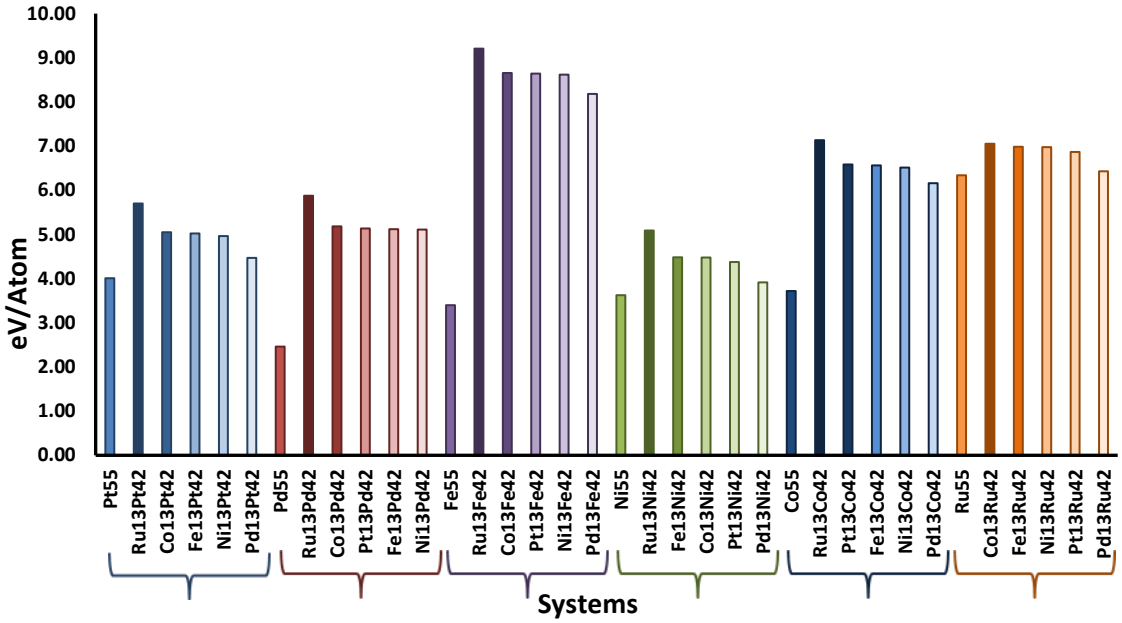

Figure 5-3: Cohesive/binding energy (eV/atom) vs. systems grouped by the family of the same shell element. The calculation was performed at the RPBE theory level with a plane-wave basis set.

The cohesive energy represents the strength of the intramolecular bonding of the solid[90], [91]. From the cohesive energy values of pure and binary nanoclusters, we can see that Ru in the core of any metal gives the highest cohesive energy, followed by Co in most cases. The case of binary clusters where Ru is in shell show more cohesive energy than the pure Ru_{55} cluster. Even if these are more strongly bonded with each other, the

preference of metal being in the core or shell can only be seen by the excess energy values which are lower of all binary combinations where Ru is the shell element. Although reaction conditions, promoters, chemical stability after CO adsorption on the cluster surface may play an important part in deciding the activity of the catalyst towards the reaction, those are not considered in this study.

The relevant data for the explanation of the above behavior of nanoclusters is given in **Figure 5-4**. Surface energy is the energy required to obtain one unit of surface area with respect to the bulk phase[83]. All the surface energies shown here are calculated theoretically for (111) surfaces for six all metals[83], [87]. Transition metals with lower surface energy usually occupy the lower coordinated regions, i.e., the surface and vice-versa.

The segregation of transition metals atoms in either core or shell of the cluster is also dependent on their atomic sizes. A bigger atom tends to occupy the surface region, while the smaller one prefers to stay in the core of bimetallic clusters[83]. More electronegative metals like Pt and Pd prefer to stay in the shell of bimetallic clusters[83].

In **Figure 5-2**, the stability of the systems $Fe_{13}Pt_{42}$, $Pt_{13}Co_{42}$, $Ni_{13}Pt_{42}$, $Pd_{13}Fe_{42}$, $Co_{13}Fe_{42}$, and their counterparts (core elements in the shell and vice versa) supports the claim of relating stability to both size and surface energy. For instance, in $Fe_{13}Pt_{42}$, $Ni_{13}Pt_{42}$, and $Co_{13}Fe_{42}$, the shell atoms are bigger and have lower surface energies than the core ones; hence, they are more stable in the shell.

Atomic Radii (Å)

Fe 1.56	**Co 1.52**	**Ni 1.49**
Ru 1.78	**Pd 1.69**	**Pt 1.77**

Ru>Pt>Pd>Fe>Co>Ni

Electronegativity

Fe 1.83	**Co 1.88**	**Ni 1.91**
Ru 2.20	**Pd 2.20**	**Pt 2.28**

Pt>Pd=Ru>Ni>Co>Fe

Surface Energy (eV/atom)

Fe 0.88	**Co 0.71**	**Ni 0.65**
Ru 1.16	**Pd 0.56**	**Pt 0.64**

Ru>Fe>Co>Ni>Pt>Pd

Figure 5-4: Atomic Radii, Surface Energy and Electronegativity of metals used. The higher (Darker-shade) to lower (lighter-shade) values are shown[81], [83], [87], [92].

While in $Pd_{13}Fe_{42}$, and $Pt_{13}Co_{42}$, the combinations are less stable due to the arrangement of metals with high surface energy and lower atomic size in the shell instead of the core. In the rest of the systems, the surface energy effects dominate. We also found that the electronegative metal atom prefers to stay in the core of the cluster with an exception to Ru. This might be due to the dominating effect of surface energy (Ru has the highest surface energy relative to other metals used in this study). All three abovementioned factors play an important part in the stability and segregation of the binary clusters.

CHAPTER 6

RESULTS – CO ADSORPTION AND DISSOCIATION ON 55-ATOM CLUSTERS

The CO adsorption is investigated for pure 55-atom clusters of Ru, Pt, Fe, Pd, Co, and Ni. CO bond breaking is only investigated for four pure metal clusters leaving the Pt and Fe clusters out, due to the chemical instability of the pure Pt and Fe cluster after CO adsorption; the structure of these clusters was seen to be distorted after the CO adsorption on a few bonding sites. The bimetallic clusters chosen to study the CO adsorption were based on excess energy to study the only combinations that are thermodynamically more stable than the others, which saves computational time as well.

6.1 Computational Details

Ground state structures of CO adsorbed on clusters were found using the plane-wave basis sets with a cutoff energy of 400 eV. Exchange and correlation interactions were treated through the GGA/RPBE method. The same cubic box with one side of 25 Å, which was used in pure cluster calculations, was used for CO adsorption and CO bond-breaking calculations. CO adsorption on all six possible active sites was investigated to find the PAS. To calculate the energy barrier, transition state calculations were done using the climbing image Nudged elastic band (CI-NEB) by interpolating three images between the initial and final states.

The binding energy of CO, $E_{ads}(CO)$, upon CO binding on the surface of the metal nanoparticle was calculated using **Eq. 6-1**.

$$E_{ads}(CO) = E(CO^*) - E(M) - E(CO) \qquad \textbf{Eq. 6-1}$$

where, $E(CO^*)$ is the energy of the cluster with one CO molecule adsorbed on its surface,

$E(M)$ is the energy of the metal cluster, and

$E(CO)$ is the energy of a single CO molecule.

According to Eq. 6-1, negative binding energy corresponds to a stable CO binding on the cluster surface.

6.2 Adsorption Sites

The highly symmetrical icosahedron structure has triangular or (111) facets with six adsorption sites known as Top (T_s), Bridge (B_s), and Hollow (H_s) sites. The T_s and B_s sites exist on the cluster vertex as well as on and face. T_s sites 1 and 2 are located on the vertex and edge top sites, respectively. B_s sites 3 and 4 are located on the facet and edge bridge site 3. H_s sites 5 & 6 are in-plane hexagonal closed packed (hcp)[93].

All six sites are shown in **Figure 6-1**.

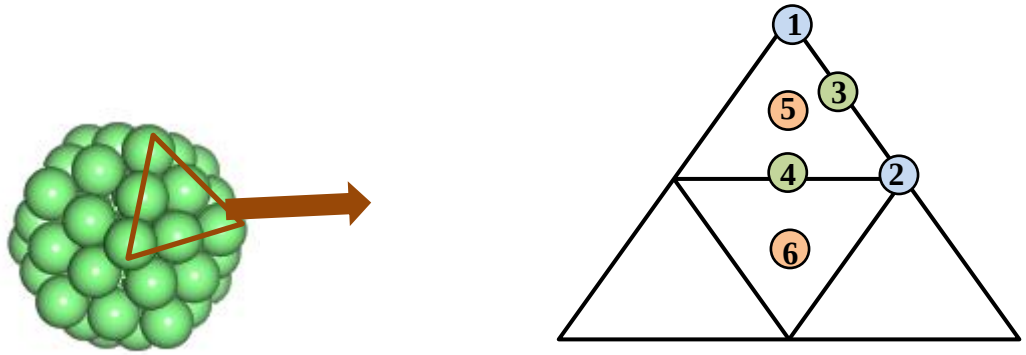

Figure 6-1: Adsorption sites on the triangular face of the icosahedral M_{55}: blue, peach, and green circles are shown as Top, Bridge, and hollow sites.

For CO adsorption, geometries that were perpendicular to the surface of clusters were considered as it is the most stable adsorption of CO with adsorbed through carbon atom[94]. This orientation can be explained because of the polarization of $2\pi^*$ and 5σ orbitals towards the carbon-end of the CO molecule and induces dipole moment towards the carbon-end[94]. In the case of the Ru_{55} cluster, the most stable adsorption site was found to be 6(Hs) with the binding energy of -2.08 eV followed by 4(Bs)-initially which got converted to 6Hs site at the end of the simulation; hence, no 4 sites was observed. On 6 and 4(now 6) sites C-O bond length was seen to be elongated to 1.375 Å and 1.356 Å, respectively (1.148 Å for free CO) after CO adsorption. Also, the 3Bs and 5Hs site converted to 2Ts and 4Bs sites, respectively, hence no 3 and 5 sites observed.

On the Pd_{55} cluster, the binding energies of CO on clusters were found to be very close on both 4(Bs) and 5(H_s) sites with C-O values to be 1.204 Å and 1.205 Å, respectively. Previous experimental and theoretical studies on slab models show that CO adsorption favors the 3-fold hollow sites on Pd (111) surface[95]. CO adsorption value on Pd_{55} nanocluster was found to be 0.3 eV larger than the experimental value of 1.47-1.54

eV on single crystal Pd (111) surface at low coverage[96], [97]. For Co_{55} 1(T_s) sites were found to be having maximum binding energy value with a C-O bond length of 1.177 Å.

The Ni_{55} showed the PAS to be 5(H_s) site with a C-O bond length of 1.206 Å. Although the preferred adsorption site on Ni (111) surface aligns with the experimental results[98][99], the binding energy values are overestimated (are in the 1.6 – 1.8 eV range), in contrast to the experimental E_b of 1.12-1.55 eV[100]. Theoretical studies performed by Carrasco et al. on the GGA-PBE level predicted the CO binding energy of -1.90 eV, which is in agreement with our findings of 1.89±0.01 range[101].

For Pt and Fe clusters, the geometries after CO adsorption got a little distorted from the initial icosahedron one. The clusters do not seem to have chemical stability after CO adsorption. Hence, the Pt_{55} and Fe_{55} clusters are not further studied for CO dissociation. These distortions can also be the reason for the high binding energy of CO onto these Pt and Fe clusters.

Table 6-1: CO adsorption Energies (E_{ads}) on all active sites (Top, Bridge and, Hollow), Bader charges at Preferred adsorption site(PAS) in Green, Bader charges(charge transferred to cluster from CO), adsorbed Carbon-Oxygen (C-O) and Carbon-Metal (C-M) distances, Bond breaking Energies of CO($E_{barrier}$) on pure nanoclusters

System		Adsorption sites						Q^{eff}_{Bader} on CO @PA (e)	$E_{barrier}$ (eV)
		1(Ts)	2(Ts)	3(Bs)	4(Bs)	5(Hs)	6(Hs)		
Ru	E_{ads}(eV)	-1.74	-2.05	-2.04	-2.07	-1.96	-2.08	-0.55	0.93
	C-O (Å)	1.178	1.182	1.182	1.129	1.207	1.219		
	C-M(Å)	1.892	1.861	1.860	2.118	2.055	2.118		
Pd	E_{ads}(eV)	-1.47	-1.41	-1.76	-1.89	-1.89	-1.85	-0.26	2.53
	C-O (Å)	1.167	1.167	1.189	1.204	1.205	1.205		
	C-M(Å)	1.862	1.860	1.982	2.062	2.062	2.070		
Co	E_{ads}(eV)	-1.47	-1.41	-1.42	-1.42	-1.41	-1.36	-0.31	4.79
	C-O (Å)	1.177	1.178	1.207	1.208	1.208	1.213		
	C-M(Å)	1.751	1.742	1.879	1.959	1.958	1.967		
Ni	E_{ads}(eV)	-1.62	-1.58	-1.72	-1.79	-1.80	-1.65	-0.49	2.61
	C-O (Å)	1.17	1.171	1.191	1.206	1.206	1.206		
	C-M (Å)	1.751	1.742	1.879	1.959	1.958	1.967		
Pt	E_{ads}(eV)	-2.23	-4.82	-2.02	-3.98	-1.88	-1.63	-0.08	-
	C-O (Å)	1.168	1.169	1.191	1.191	1.205	1.206		
	C-M(Å)	1.85	1.84	2.01	2.01	2.12	2.11		
Fe	E_{ads}(eV)	-2.31	-4.08	-1.03 ($2B_s$)	-3.29 ($2B_s$)	-1.77	-2.29 ($2B_s$)	-	-
	C-O (Å)	1.181	1.185	1.187	1.185	1.219	1.184		
	C-M(Å)	1.770	1.775	1.766	1.758	2.025	1.781		

In the case of the Pt_{55} cluster, the maximum binding energy of -3.98 eV was found on the atop site ($2T_s$). Several theoretical studies[26], [77], [102]–[105] have been conducted over the years to predict the adsorption site on Pt (111) surface. Our findings of adsorption on top site are in agreement with the experimental studies of CO adsorption on the Pt (111) surface[104]. The Pt-C(Metal-C) distances for atop, and bridge sites were found to be 1.845 Å and 2.01 Å, respectively; which resembles the experimental values of Pt-C distances which are 1.85±0.1 and 2.08±0.07 Å for top and bridge, respectively. The C-O distance is 1.15±.06 Å for all 6 sites on the Pt_{55} nanocluster. All the Pt-C distances are in agreement with theoretical studies of CO adsorption done on different theory levels on Pt (111) surface by Orita et al.[104].

For Fe_{55}, the strongest bonding of CO was found to be -4.08 eV at the top site ($2T_s$) of the cluster.

In this study, we found that the dissociation of CO (CO bond breaking) on the surface of Ni_{55}, Pd_{55}, and Co_{55} is an endothermic reaction, while on the surface of Ru_{55} is exothermic. The CO adsorption sites with PAS and C-O bond length are shown in **Table 6-1**.

The CO dissociation barrier was found to be the smallest for the Ru_{55} cluster, followed by the 55-atom Pd, Ni, and Co clusters. Studies were done by Liu et al. on different Ni surfaces showed that the CO dissociation (bond breaking) barrier is maximum at (111) surface compared to others. They found this barrier to be 2.96 eV while using PBE as implemented in VASP, which is 0.35 eV higher than that in our studies done at the RPBE theory level with the same energy cutoff[106].

The negative values of the Bader charges for Ru, Pd, Ni, and Co show that the charge was transferred to the CO molecule from the metal surface upon CO adsorption. Higher values of charge transfer on the Ru cluster surface corresponds to the strong binding energy value of the CO molecule on the cluster surface. The C-O bond length values on the PAS of all clusters indicate a very strong interaction between the CO molecule on the Ru surface, followed by Ni, Pd, and Co. It also indicates that breaking of the C-O bond on the Ru cluster is the easiest on the Ru surface, which is in the agreement with the findings that Ru is the best catalyst for the FT reaction. In the case of the Pt_{55} cluster, a minimal amount of charge got transferred to CO. This can be due to the highest electronegativity of Pt as compared with the other metals used.

Table 6-2: CO adsorption Energies (E_{ads}) on all active sites (Top, Bridge and, Hollow), Preferred adsorption site(PAS) in Green, Bader charges(charge transferred to cluster from CO), CO Bond breaking Energies ($E_{barrier}$) on Binary nanoclusters

System	E_{ads} (eV) @ Adsorption sites						$E_{barrier}$ (eV)
	1(T_s)	2(T_s)	3(B_s)	4(B_s)	5(H_s)	6(H_s)	
$Ru_{13}Pd_{42}$	-1.39	-1.02	-1.48	-1.52	-1.58	-1.52	3.85
$Ru_{13}Pt_{42}$	-1.85	-1.29	-1.35	-1.23	-1.23	-1.01	-
$Ru_{13}Fe_{42}$	-	-	-1.17	-	-	-	--
$Ru_{13}Ni_{42}$	-1.70	-1.49	-1.66	-1.80 (5 H_s)	-1.79	-1.68	2.19
$Co_{13}Pd_{42}$	-1.18	-1.24	-1.59	-1.21	-1.67	-0.68	
$Co_{13}Ni_{42}$	-1.56	-1.50	-1.63	-1.69	-1.68	-1.56	2.32
$Co_{13}Pt_{42}$	-1.53	-1.60	-1.75	-1.64	-1.64	-1.64	4.11
$Co_{13}Fe_{42}$	4.26	-0.07	2.13	3.57	2.91	1.66	-
$Ni_{13}Pd_{42}$	-1.20	-1.22	-1.61	-1.57	-1.69	-1.74	3.6
$Ni_{13}Pt_{42}$	-1.58	-1.62	-1.76	-1.64	-1.63	-1.64	4.23
$Ni_{13}Fe_{42}$	2.12	-0.56	-0.90	4.41	-0.32	-0.54	-
$Fe_{13}Ru_{42}$	-1.73	-1.78	-1.80	-1.96	-1.97	-1.94	1.16
$Fe_{13}Pd_{42}$	-1.90	-0.41	-0.63	-1.18	-0.83	-2.42	-
$Fe_{13}Pt_{42}$	-4.11	-3.87	-2.00	-2.09	-3.77	-1.39	7.85
$Fe_{13}Co_{42}$	-1.35	-1.51	-1.37	-1.50	-1.45	-1.39	2.79
$Fe_{13}Ni_{42}$	-1.54	-1.39	-1.49	-1.60	-1.61	-1.48	2.67
$Pt_{13}Pd_{42}$	-1.56	-1.39	-1.71	-1.806	-1.807	-1.72	3.81
$Pt_{13}Fe_{42}$	0.86	-1.35	-4.69	-3.17	-3.91	-5.83	-

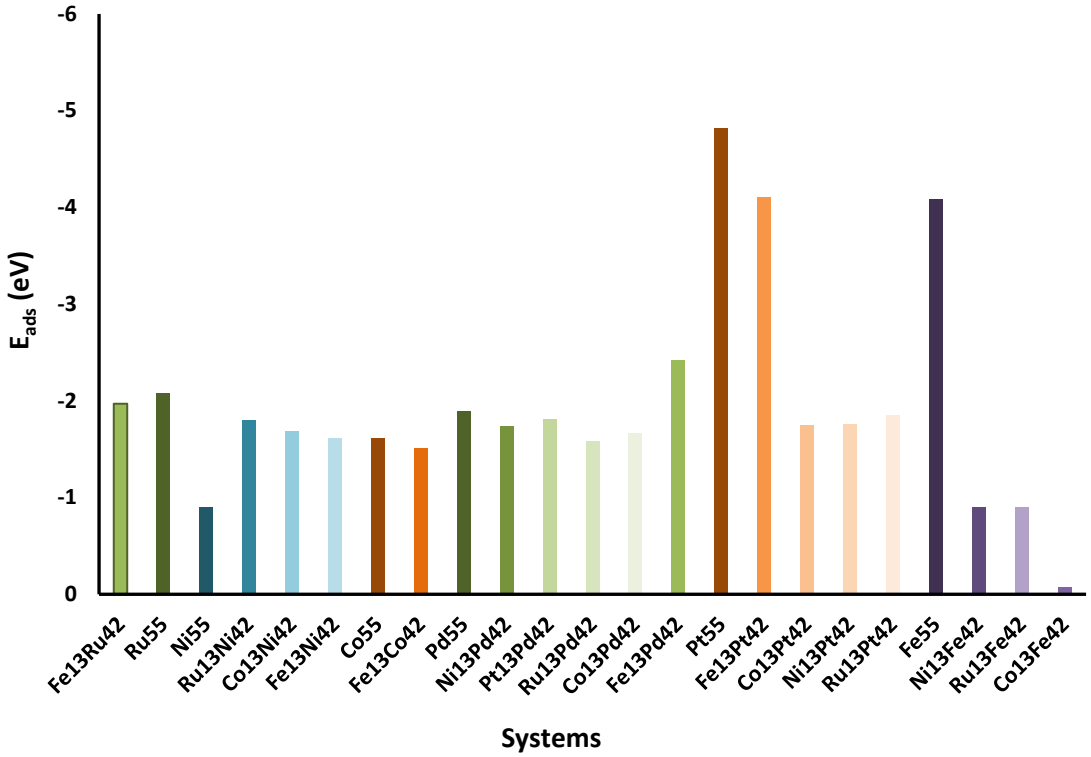

Figure 6-2: E_{ads} energies of CO binding on the 55 atom clusters.

The excess energy of the FeRu combination cluster where Fe was in the core was found maximum hence the binary combination where Ru was in the shell, chosen to perform the CO adsorption studies. As we can see in **Figure 6-2**, the Ru pure cluster shows better binding of CO onto its surface as compared to when Fe is added in the core of Ru clusters. For the binary combinations where Ni was the shell element, Ru in the core of the cluster showed the most robust binding of CO molecule on its surface, followed by Co and Fe. This means that the $Ru_{13}Ni_{42}$, $Fe_{13}Ni_{42}$, and $Co_{13}Ni_{42}$ are better at adsorbing CO than the pure Ni cluster.

Interestingly as the excess energy was improved significantly when the metals (Ru, Pt, Fe, Ni, and Co) were added to the cluster with Pd as shell element, the binary

combinations with Pd in the shell did not show better CO binding except when Fe was in core. Similarly, for the binary combinations with Pt, Fe, and Co in the shell, the CO binding to the surface of the cluster was not stronger than their pure counterparts. We can understand that by changing the composition of nanoclusters how the CO binding energy can be varied. Although to conclude the potential of the metals to break the CO bond, CO bond-breaking needs to be studied.

6.3 Bader Charge Analysis

To study the interactions between the adsorbed CO and clusters, the Bader charges were studied. Bader effective charges were calculated as the difference between the valence charge of free atom and Bader charge[107]–[110].

$$Q_{Bader}^{eff} = Q_{val} - Q_{Bader} \qquad \textbf{Eq. 6-2}$$

Where, Q_{Bader}^{eff} is the Bader effective charge, Q_{val} and Q_{Bader} are the valence (ZVAL-given in the pseudopotentials-POTCAR file) and calculated Bader charge of each atom. The effective Bader charges given in **Table 6-3** are the net charges transferred between the CO molecule and the cluster, charge exchange between the core and shell metal atoms. A negative value of Q_{Bader}^{eff} means there was a net transfer of charge (charge acquired) to the atom.

By looking at charge transfer data of pure clusters in **Table 6-1**, we can clearly see that a net negative sign shows that the charge got transferred to the CO molecule from the cluster. Pt being the most electronegative among the metals chosen shows the minimum charge transfer of (-)0.08 e to CO.

Table 6-3: Bader charges, Q_{Bader}^{eff} on CO: charge transferred to CO from the cluster, Q_{Bader}^{eff} on Shell atoms: charge transferred to/from shell atoms of cluster and Q_{Bader}^{eff} on core atoms: charge transferred to/from the core atoms of the cluster. A negative charge means charge acquired and vice versa.

System	Q_{Bader}^{eff} on CO (e)	Q_{Bader}^{eff} on Shell atoms (e)	Q_{Bader}^{eff} on Core atoms (e)
$Ru_{13}Pd_{42}$	-0.262	-2.947	3.210
$Ru_{13}Pt_{42}$	-0.092	-4.697	4.793
$Ru_{13}Fe_{42}$	-0.445	4.52	-4.087
$Ru_{13}Ni_{42}$	-0.499	0.230	0.268
$Co_{13}Pd_{42}$	-0.251	-3.613	3.858
$Co_{13}Ni_{42}$	-0.483	-1.004	1.483
$Co_{13}Pt_{42}$	-0.154	-5.004	5.155
$Co_{13}Fe_{42}$	-0.335	1.426	-1.092
$Ni_{13}Pd_{42}$	-0.273	-2.753	3.024
$Ni_{13}Pt_{42}$	-0.154	-4.203	4.356
$Ni_{13}Fe_{42}$	-0.451	-2.046	2.501
$Fe_{13}Ru_{42}$	-0.473	-3.606	4.079
$Fe_{13}Pd_{42}$	-0.242	-4.376	4.621
$Fe_{13}Pt_{42}$	-0.006	-7.103	7.108
$Fe_{13}Co_{42}$	-0.332	-1.486	1.822
$Fe_{13}Ni_{42}$	-0.481	-2.624	3.105
$Pt_{13}Pd_{42}$	-0.263	0.393	-0.127
$Pt_{13}Fe_{42}$	-0.392	8.866	-8.470

In bimetallic systems, the charge transfer was observed from less electronegative element to higher electronegative metal atoms.

The values of charge transferred were found to be directly proportional to the electronegativity difference. In the case of equal electronegative values of Pd and Ru, the core element (Ru) transferred charge to the shell atoms (Pd). We observed that the more electronegative metal atom prefers to stay in the shell of the binary cluster and vice versa. If we compare $Fe_{13}Ru_{42}$ and $Ru_{13}Fe_{42,}$ we find that due to the higher electronegativity of Ru than Fe, the charge gets transferred to Ru regardless of the position of the metal atoms (either core or shell). In general, the charge redistribution promotes electrostatic force between the core and the shell atoms of a nanocluster leading to stability of the bimetallic particles[88].

6.4 Radial Distribution Function

To study the structural stability of the cluster after CO adsorption, the Radial Distribution Function (RDF) of bare 55-atom nanoclusters and CO adsorbed cluster has been generated. The first peak in the RDF corresponds to the distance between the metal-metal first neighbors. **Figure 6-3** shows the RDF plots for pure clusters and CO adsorbed. RDF denotes the number of atoms present at a distance (radius) from the center of the geometry at $r = 0$. No change in the pure cluster's geometry has been observed in our studies after CO adsorption on the surface of the cluster.

RDF figures comparison for bare clusters and geometries corresponding to CO adsorbed at the PAS for binary clusters are given in Appendix A. For Ru, Ni, Co, and Pd clusters, no significant change in geometry of binary clusters after adsorption of CO has

been observed. This shows that clusters are geometrically stable after the CO adsorption. But there have been disturbances in the plots for Pt and Fe. After CO adsorption on both metal clusters, the geometry got a little distorted from a regular icosahedron. This is what we can also see from the RDF plots; the nearest neighbor distances are little different after and before CO adsorption.

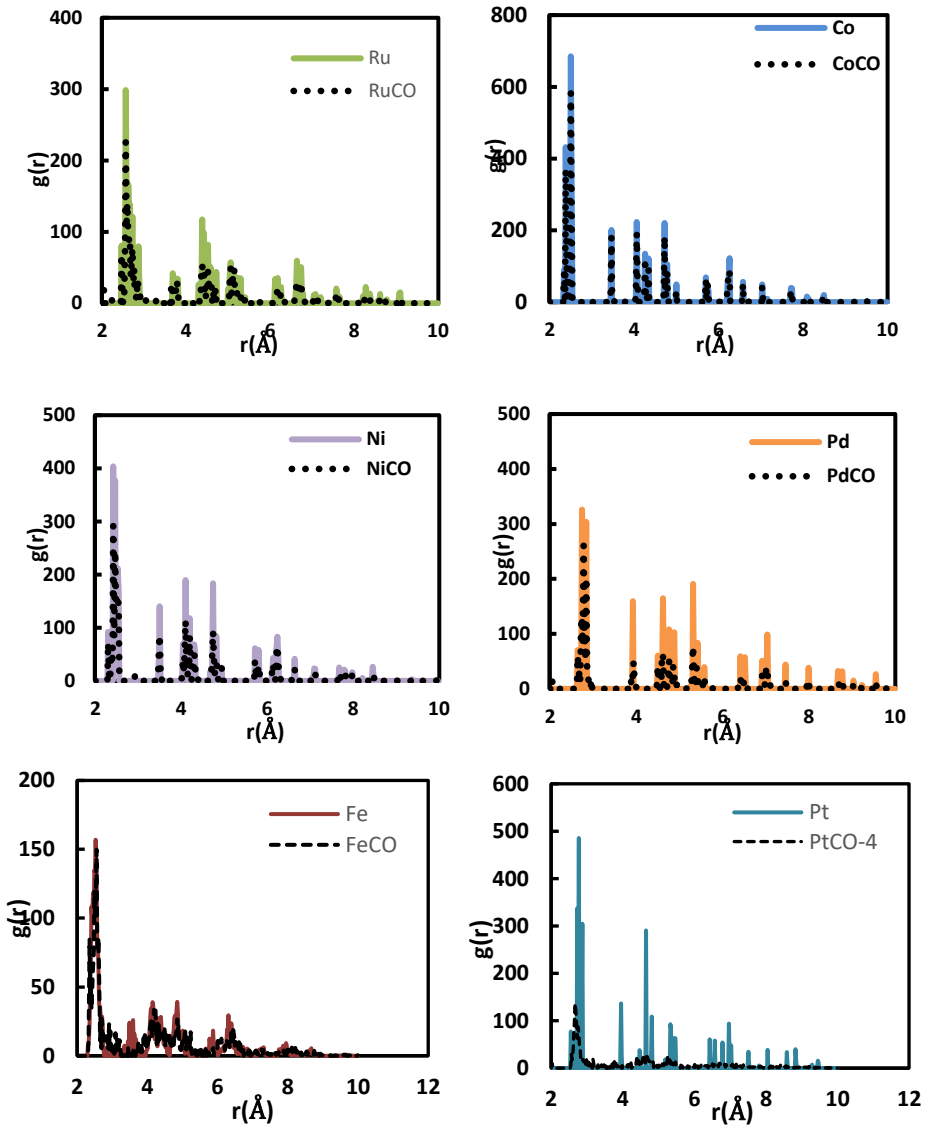

Figure 6-3: Radial distribution function $g(r)$, relative to the center of geometry of clusters for Ru, Co, Ni, and Pd with and without CO adsorption at PAS.

6.5 Charge Density Difference

Charge density difference was studied to see how the CO molecule affects the electron configuration distribution with respect to the isolated CO molecule and cluster. This shows the change in charge density during the reaction of the binding of the CO molecule to the cluster surface. This study ultimately helps in understanding the adsorption process and bonding mechanisms.

The charge density difference of the CO adsorbed on the nanocluster surface was calculated using the **Eq. 6-3**.

$$\Delta\rho = \rho_{M-CO} - \rho_M - \rho_{CO} \qquad \textbf{Eq. 6-3}$$

here, $\Delta\rho_{M-CO}$, ρ_M, and ρ_{CO} are the charge density of the CO adsorbed cluster, bare cluster, and the CO molecule, respectively. To calculate ρ_M, and ρ_{CO} the atomic positions are fixed as those they have in the CO adsorbed system.

This charge density difference $\Delta\rho$ has been shown in **Figure 6-4** for pure and binary 55-atom clusters with CO adsorbed at PAS.

As we can see in **Figure 6-4**, after the adsorption/binding of CO on the pure Ru_{55} cluster, the charge density did not change inside as well as the outside layers of the cluster. A negative charge density (blue) can be seen on the Oxygen atom of the CO molecule. For Ni, Pd, and Co clusters, the charges on the surface and layers inside which are closer to the CO adsorption site, got changed. One thing is to be noted that the clusters containing Fe regardless of the position (either core or shell), the charge density seems to vary a lot throughout the cluster, with the exception of $Fe_{13}Ni_{42}$ and $Fe_{13}Co_{42}$. CO adsorption significantly varies the charge density inside and at the surface of the cluster.

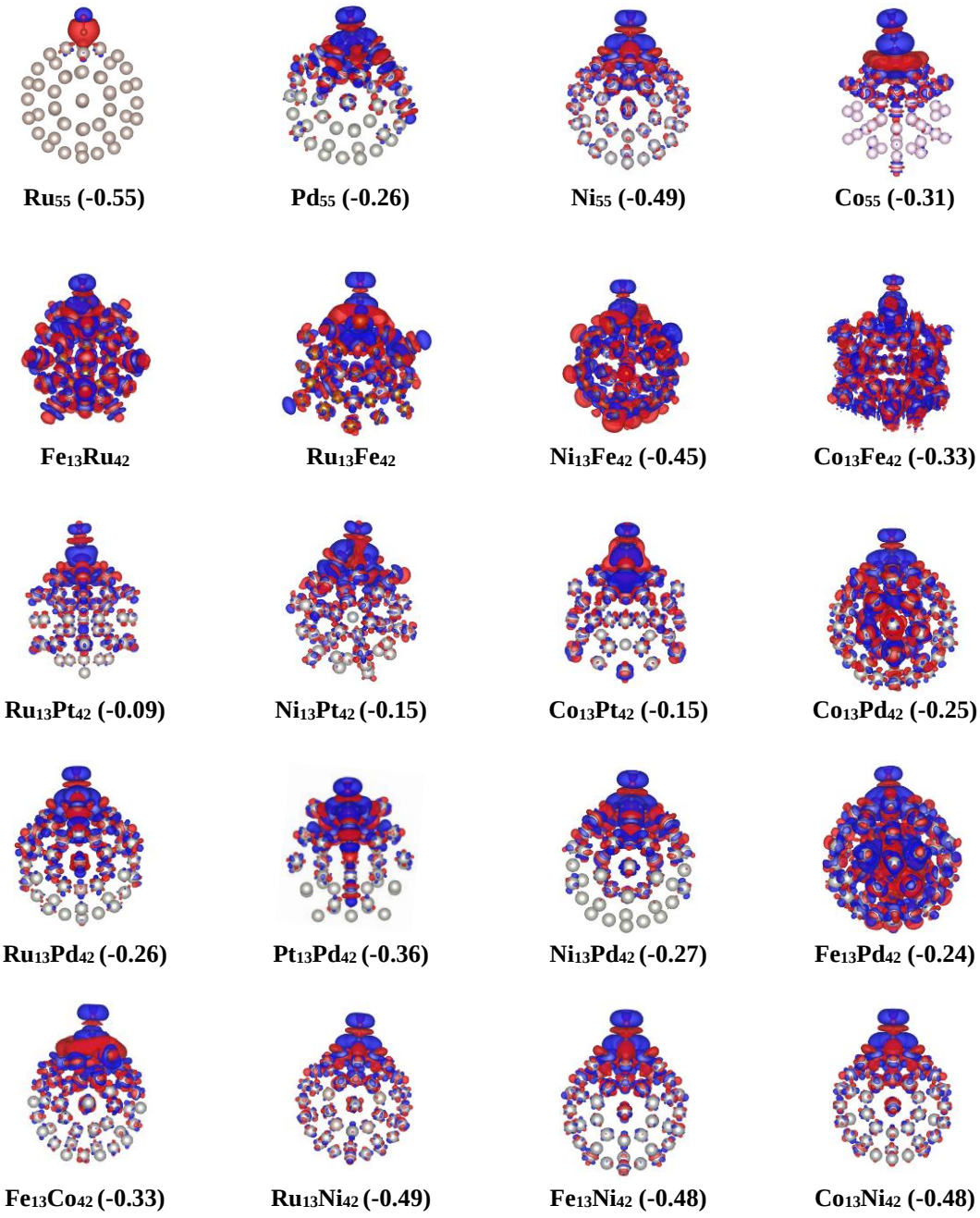

Figure 6-4: Charge density difference ($\Delta\rho$) for CO adsorbed on the PAS of each pure and bimetallic cluster. Blue and Red colors represent the accumulation (more negative charge) and depletion (more positive charge) of the charges, respectively. The values in parenthesis represent the charge transfer from CO to the cluster surface (negative and positive values of charge corresponding to accumulation and depletion of the charge on CO molecule).

CHAPTER 7

COMPARISON BETWEEN 13- AND 55-ATOM CLUSTERS

This chapter details the comparison between 13 (RPBE/DNP theory level) and 55 atom nanocluster's properties, e.g. excess energy, CO adsorption energy, etc.

7.1 Effect of Size on Cohesive Energy of Pure Clusters

Although for 13 atom clusters only Ru, Pt, and Pd were used in this study because 13-atom Fe, Co, and Ni were investigated by the Mainardi group in prior work[82], for comparison purposes, we calculated the cohesive energy of all six elements with the theory level used in this study (RPBE/DNP/ECP) which is different than used in Gyawali et al. The cohesive energy was calculated using **Eq. 3-1**.

The trend of cohesive energy for 13 atom clusters from maximum to minimum value is as follows: Co>Ru>Ni>Fe>Pt>Pd, while for the 55-atom clusters is: Ru>Pt>Co>Ni>Fe>Pd. For both cluster sizes, the Pd clusters show the lowest binding (cohesive) energy within the clusters. The results of the 55-atom cluster agree well with the studies done on the FT catalytic activity[12], [111]–[114] more than the 13 atom clusters. This might be due to the more internal strain in smaller size clusters.

The other reason might be the choice of ECP pseudopotential used in the calculation of 13 atom clusters which replaces the core electrons with a single potential instead of including all electrons of the cluster in the calculation.

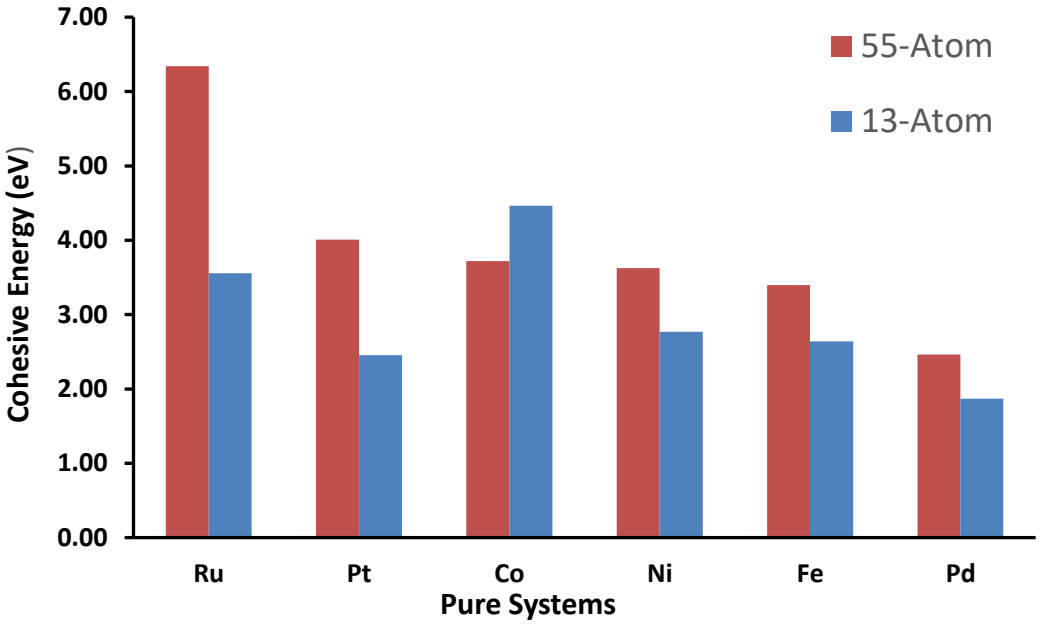

Figure 7-1: Comparison of Cohesive/binding energy (eV/atom) pure systems grouped by the family of the same shell element for 13 and 55 atom clusters.

Figure 7-1 shows the comparison plot of cohesive energies of 13 and 55 atom pure clusters.

7.2 Effect of Size and Composition on Excess energy of Bimetallic Systems

In 13 atom clusters, only the combinations of bimetallic clusters where shell atoms are Pt, Pd, and Ru are considered and compared with similar combinations of 55 atom nanoclusters. For both sizes viz. ~0.5 nm (13-atom) and ~1.2 nm (55-atom) clusters, the systems containing Pt in the shell had maximum excess energy followed by Pd and Ru in the shell. The clusters containing Pt and Pd in the shell positions showed minimum excess energy when Pd and Pt are in the core of the clusters, respectively. That means Pt in the core of Pd and vice versa were seen to be less thermodynamically stable as compared to

other binary combinations. For both sizes, clusters containing Ru in the shell showed to have maximum excess energy when Fe was in core followed by Ni/Co, Pt and Pd.

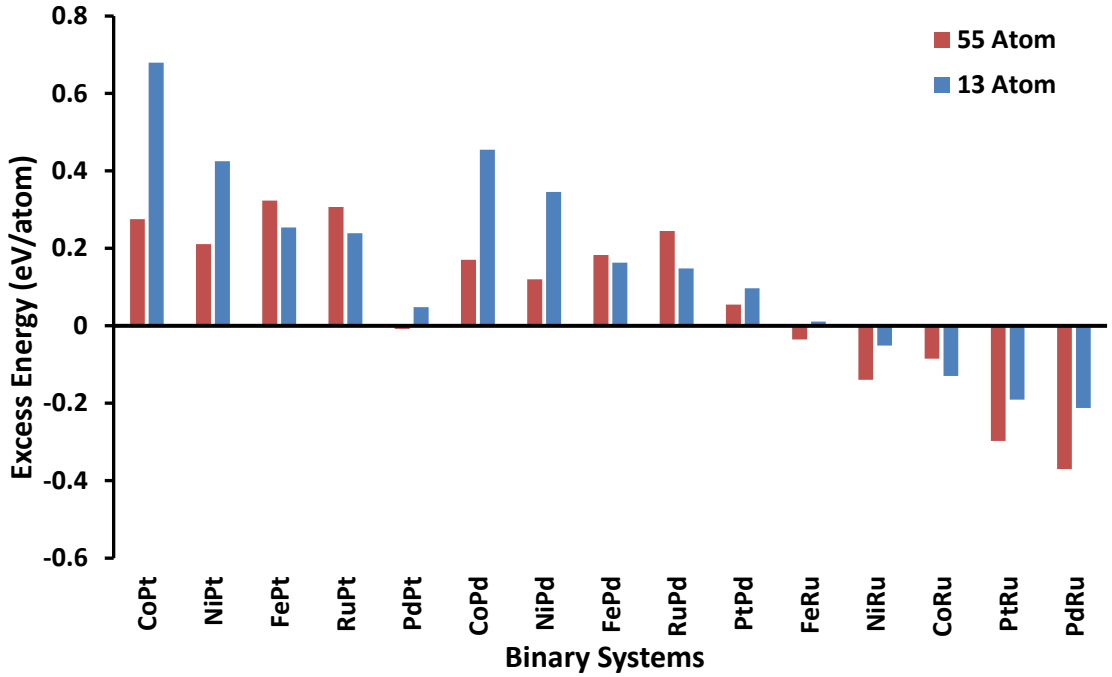

Figure 7-2: Comparison of Excess energy (eV/atom) Vs. Binary systems are grouped by the family of the same shell element. The first element in the name is the core-metal and the second one is shell-metal (in CoPt: Co in the core, and Pt in the shell).

Like cohesive energy results, for 13-atom clusters, the excess energy values also show better thermodynamic stability for clusters with Co and Ni in the core when the shell elements are Pd and Pt. The clusters the core element is Pd, with any shell element (Ru, Pt) show the lowest stability than any other binary combinations. We can conclude that Pd does not prefer to stay in the core regardless of any shell atom for both sizes of the clusters. The expected reason behind this nature has been explained in section **5.2**.

7.3 Effect of Size and Composition on CO Binding Energies

7.3.1 Effect of Size

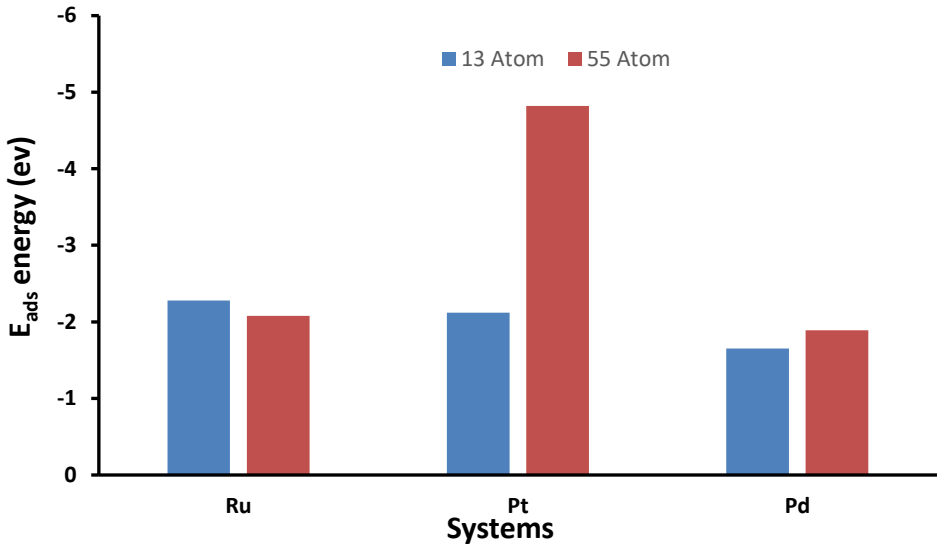

Figure 7-3: Comparison of Excess energy (eV/atom) Vs. Binary systems are grouped by the family of the same shell element. The first element in the name is the core-metal, and the second one is shell-metal (in CoPt: Co in the core, and Pt in the shell).

The 13 atom and 55 atoms both show the same trends for Ru and Pd metals in the CO binding energies. But for Pt, the 55 atom clusters show almost double the value of CO adsorption energy than on 13 atom cluster.

7.3.2 Effect of Composition

13 Atom Cluster

The CO binding/adsorption energies are maximum for pure Pd cluster as compared to the binary combinations when Pd was in the shell, and Fe, Co, Ni, Ru, and Pt were in the core of the cluster. For the clusters with Pt, and Ni in the core of the Pd cluster, the hollow site is preferred for CO adsorption like the pure Pd cluster. For the clusters with Ru and Fe in the core of the Pd cluster, the hollow and bridge sites have almost the same CO

binding energy. We can see that from these results that by changing the core of the cluster with other elements can affect the CO binding preferred adsorption site.

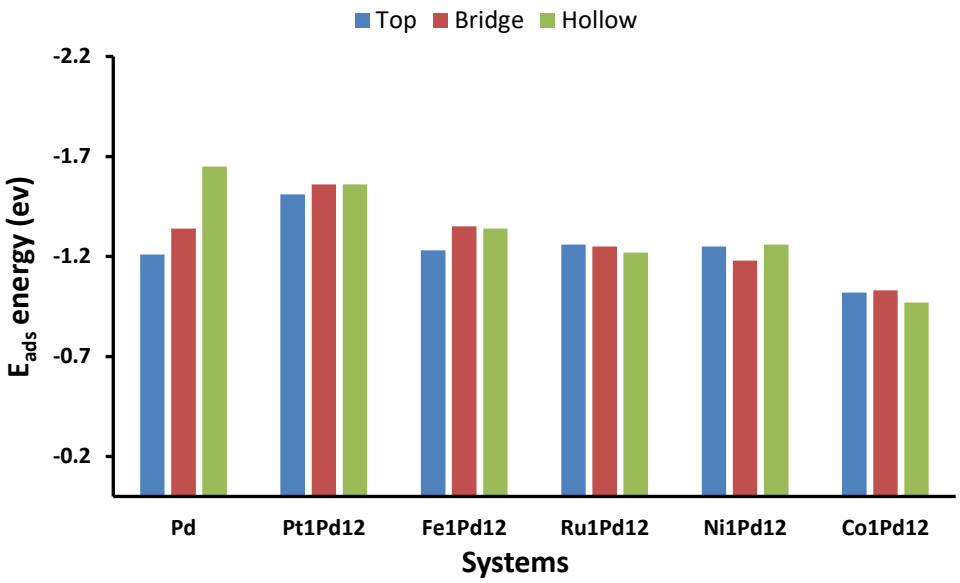

Figure 7-4: Comparison of Excess energy (eV/atom) Vs. Binary systems are grouped by the family of the same shell element. The first element in the name is the core-metal, and the second one is shell-metal (in CoPt: Co in the core, and Pt in the shell).

The CO binding energy on the pure Pt and the combination where the core element is Pd is almost the same. For the other binary combinations, it is lower than the Pure Pd cluster. It is interesting to note that the preferred absorption site does not change for any binary combinations and stays top site as PAS similar to the pure Pt_{13} cluster. The lowest binding energy was observed when the core element is Co.

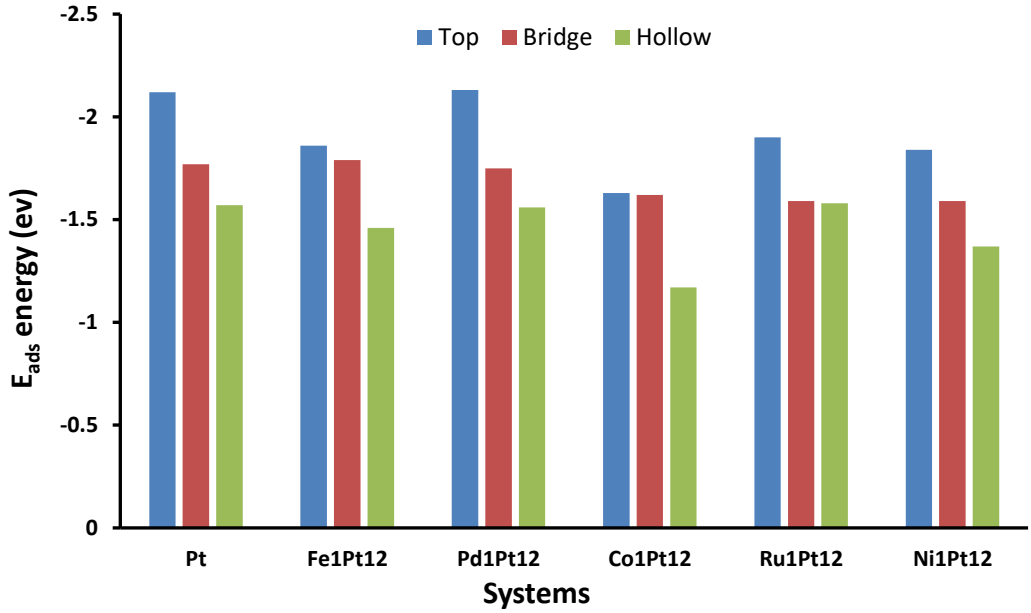

Figure 7-5: Comparison of E_{ads} energy of CO on pure and Binary systems grouped by the family of the same shell element. The first element in the name is the core-metal and the second one is shell-metal.

For the Ru cluster, the binding energy does not change much with any binary combinations except when Pt is in the core. This change can be due to the distorted geometry of Pt_1Ru_{12} after CO adsorption. Also, the PAS stays the same as the Ru_{13} pure cluster (top) regardless of the type of core metal atom.

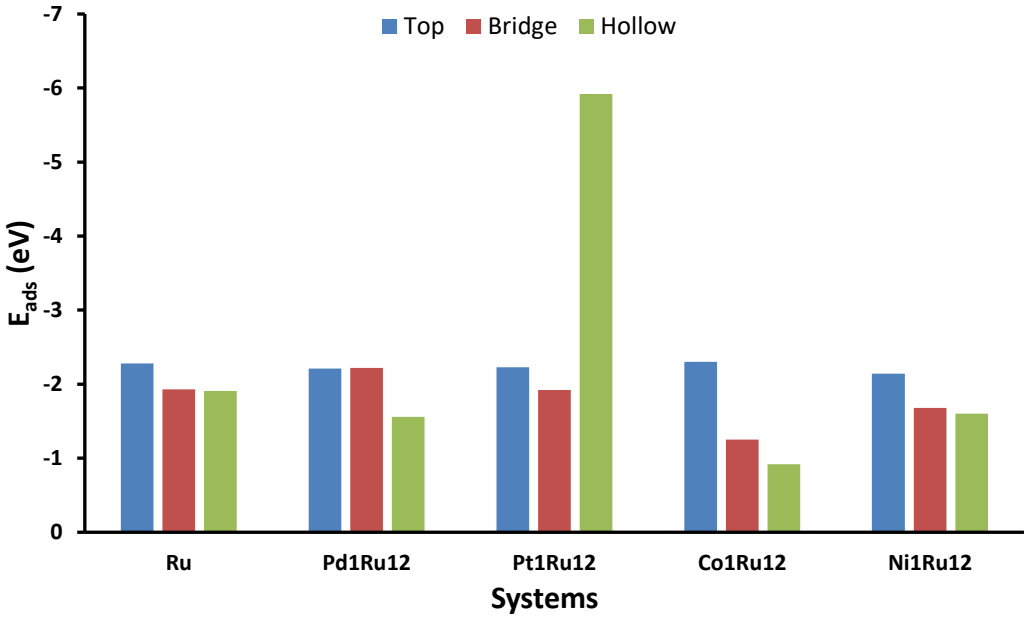

Figure 7-6: Comparison of E_{ads} energy of CO on pure and Binary systems grouped by the family of the same shell element. The first element in the name is the core-metal, and the second one is shell-metal (in CoPt: Co in the core, and Pt in the shell).

In all three cases where the shell atoms were Pd, Ru, and Pt, the lowest CO binding energy was found to be when Co was added to the core of these clusters.

55 Atom Clusters

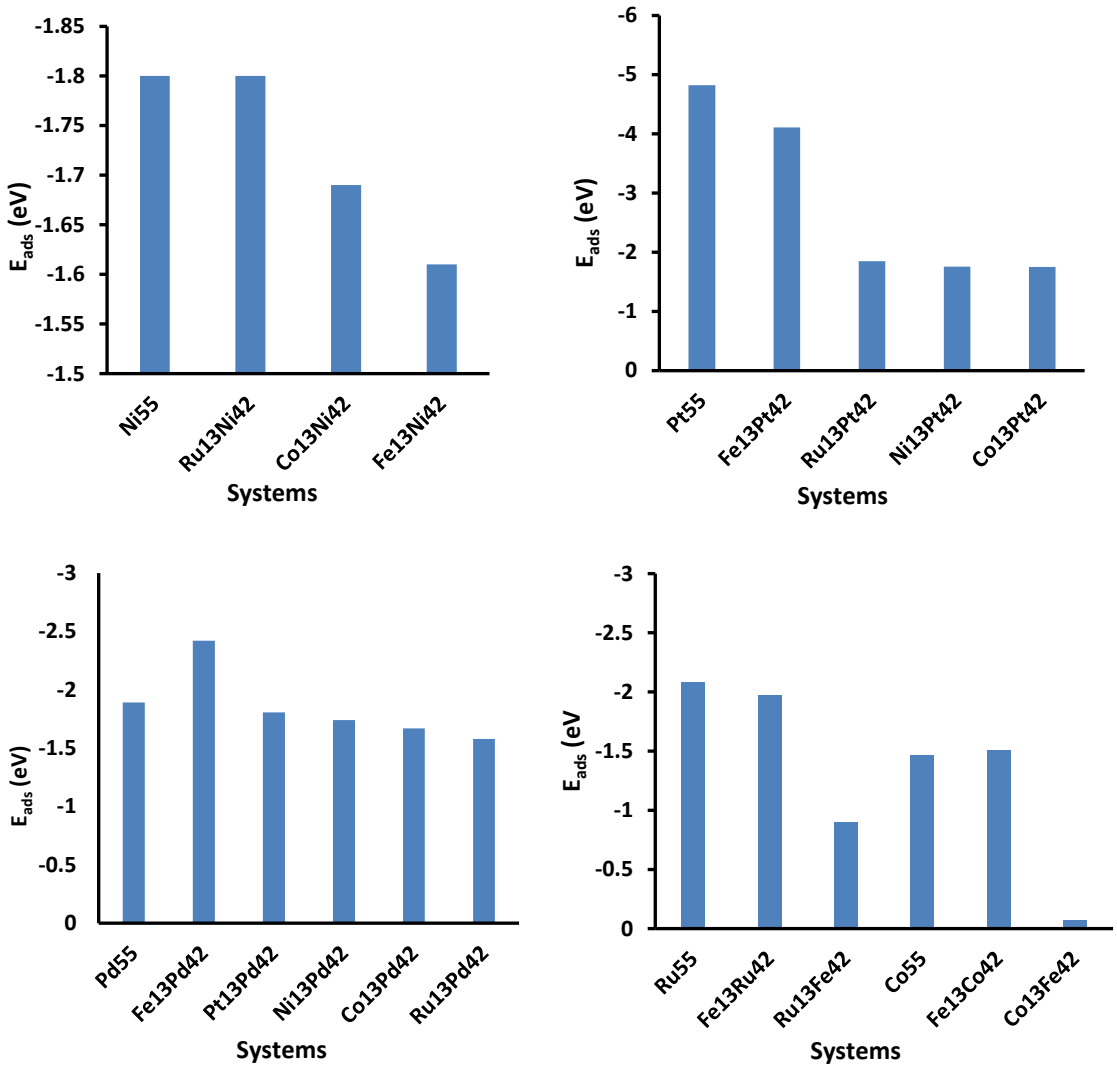

Figure 7-7: Comparison of CO binding energy on pure and Binary systems grouped by the family of the same shell element. The first element in the name is the core-metal and the second one is shell-metal (in $Co_{13}Pt_{42}$: Co in the core, and Pt in the shell).

The comparison of binding energies on the surface of pure and binary nanoclusters is given in **Figure 7-7**. The combinations further explored based on thermodynamic stability are compared based on CO binding energy. For the Ni_{55} cluster, the CO binding/adsorption energy stays the same when Ru was added to the core of the cluster. For Ni_{55} clusters, the CO was bonded stronger when Co was added in the core of the cluster

as compared to when Fe was the core element. For the Pt_{55} nanocluster, the CO binding energy was reduced by almost half when Ru, Co, and Ni were added to the core of the cluster. These combinations can help to decrease the tendency of Pt to form coke on its surface due to the strongly bonded CO. In the case of Pd nanocluster, the CO binding energy improved by 0.6 eV when Fe was added to the core of the cluster. The applications where the efficiency of Pd as a catalyst is low due to the weak bonding of CO molecule, adding iron in the core of the expensive Pd element(shell) can improve the performance significantly. Adding the Fe in the core of Co nanoclusters improved the CO binding slightly. For combinations where the shell element is Fe, the addition of Ru in the core showed strong bonding of CO as compared to when the Co was in the core.

7.4 Effect on % Difference

7.4.1 Effect of Size

For the 13 atoms, the % Diff was maximum for Ru, followed by Pt and Pd. The bimetallic clusters were not studied for % Diff as my Colleague studied those. The only common metals in both sizes are Ru and Pd, which shows similar results for the % Diff value.

7.4.2 Effect of Composition

To see the composition effect on the % Diff, we plotted a graph to compare the various nanoclusters consisting of 55 atoms and is shown in **Figure 7-8**.

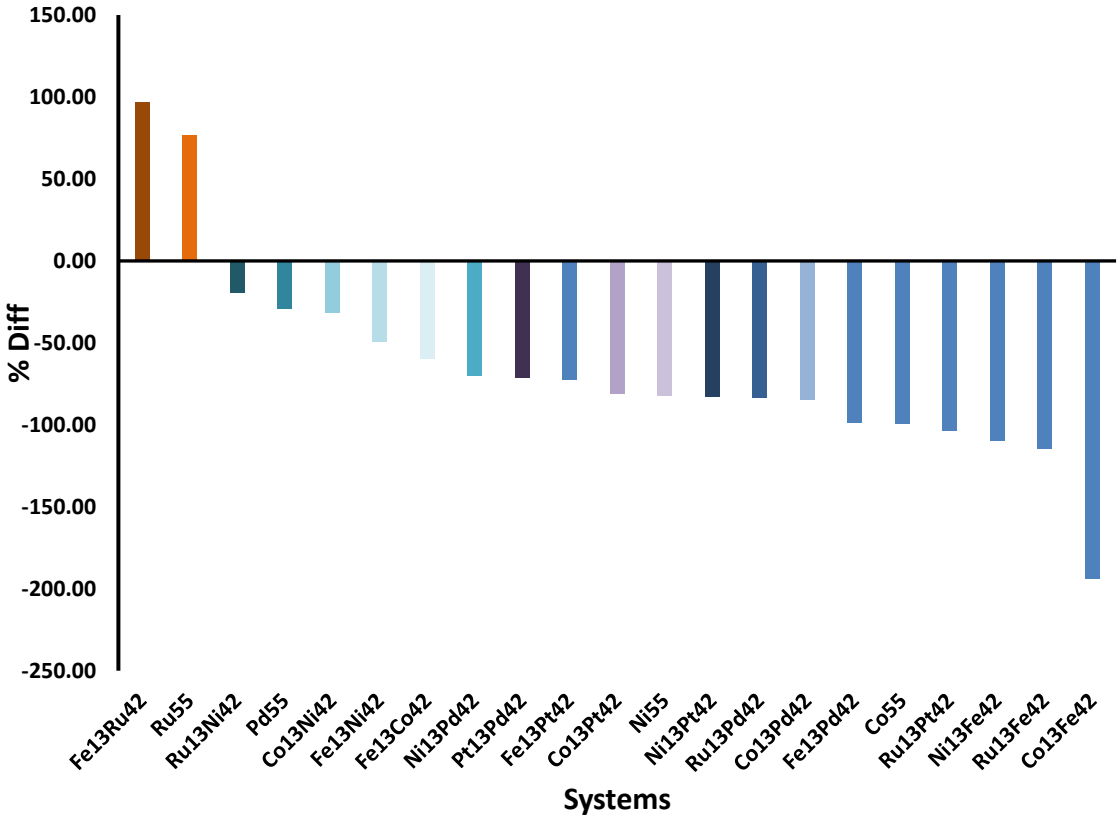

Figure 7-8: % Difference for Pure and Bimetallic nanoclusters.

The % Difference combines the effect of CO adsorption and CO bond breaking on the cluster surface. Fe in the core of Ru cluster was found to be the best catalyst among the cases explored based on % Diff. Ru_{55} is the next best case, which also has been known to show the best catalytic properties towards the FT process. Adding Ru in the core of Ni and Fe in the core of Co clusters have shown to be better than their pure counterparts. The $Fe_{13}Co_{42}$ was found to be better than $Co_{13}Fe_{42}$. Ru in the core of Ni shows better catalytic activity than in any other metal's core. Fe, Ru, and Co in the core of clusters have shown to increase the % difference value than the pure counterparts. But the core-shell combinations depend on size, surface energy, the electronegativity of the metals.

The graph shown in **Figure 7-9** combines the CO binding energy, the reaction barrier, reaction/formation energy of the product(atomic C and O on the surface), and the initial predictor(% Diff). We can see that the metal clusters having the highest % Diff have low reaction barriers and low reaction energy. The CO binding energy should be higher but not so much that it does not allow the C-O bond breaking.

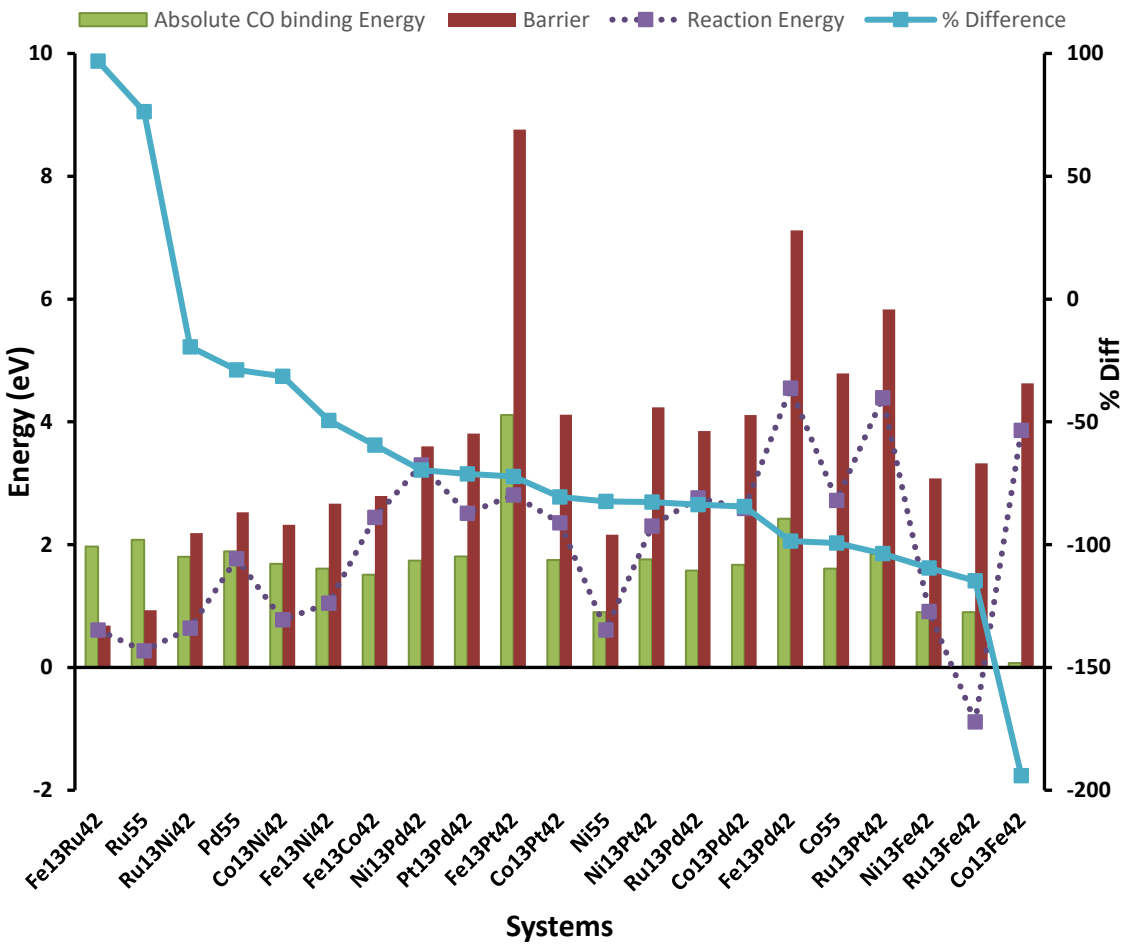

Figure 7-9: Summary of Comparison of CO binding energies, CO bond-breaking energies, % Difference, and Barrier energy for pure and binary systems grouped by the family of the same shell element. The first element in the name is the core-metal, and the second one is shell-metal (in CoPt: Co in the core, and Pt in the shell).

CHAPTER 8

CONCLUSIONS AND FUTURE WORK

8.1 Conclusions

In this work, DFT was used to study the catalytic systems (isolated nanoclusters) of icosahedral geometry with different sizes and compositions. Magic number clusters with icosahedral geometry were chosen as they have been seen to be most stable in previous theoretical studies[115], [116].

In ~0.5 nm size range, pure clusters of Ru, Pd, and Pt, while binary combinations of Ru, Pd, Pt, Fe, Ni, and Co, where shell element was Ru, Pd, and Pt, were studied. The results of this work are:

- The binary combinations where the shell element is Pt and Pt, the surface energy of metal atoms, was seen to be the dominant factor in cohesive energy trends, while size effect was found to be the dominant factor in the case of bimetallic systems where the host(shell) atom was Ru.
- According to the % difference values calculated for 13-atom pure clusters, Ru was found to be the best candidate for catalytic activity followed by Pd and Pt. Our results of Ru being the best and Pt being the worst catalysts for FT reaction also in full agreement with the literature findings[82].

In the clusters of ~1.2 nm size range, pure clusters of Ru, Pd, Ni, and Co, while 30 binary combinations in the core-shell structure of the above-mentioned elements along with

Fe and Pt were explored. Pure clusters of Fe and Pt were not considered for CO dissociation because of distortion of the cluster geometry making it asymmetric. The results of this work are:

- Pt 55-atom cluster regained its distorted reduced core, which is reported to be most stable for Pt cluster of this size[89].
- Among the pure nanoclusters, Ru was found to be having a maximum value of % difference, followed by Pd, Ni, and Co. A hollow site for CO adsorption was preferred in Ru and Ni clusters.
- Dissociative adsorption of CO occurred on the Ru surface on the bridge and hollow sites. A hollow site (either 5 or 6) is preferred for CO binding in pure Pd clusters and the binary combinations where Pd is the surface (shell) element.
- Surface energy is one of the factors influencing the type of mixing in bimetallic systems and was found to be overcoming the side effects in most of the binary systems explored.
- We also found that more electronegative metal atom prefers to be in the shell in binary combinations where Pd and Pt are the shell elements. The effects of surface energy, atomic size, and electronegativity play a vital role in the mixing and stability of bimetallic systems.
- From the Bader charge calculations, it was found that charge gets transferred to CO molecule from nanoclusters. More charge transfer occurred (higher value of Bader charge) from the surface to the CO molecule occurred in alloys involving Fe, Ni, and Ru.

- The charge density difference before and after CO adsorption on the surface of the cluster was calculated. It was found that the systems involving Fe showed charge dispersion all over the clusters and this might be due to the enhancement of local magnetic moments on the surface of the Fe_{55} cluster [115] in 55 atom clusters.
- Based on both % difference and excess energy values, we propose that the Fe core with Pt, Pd, Co, Ni, and Ru shells are preferred combinations for bimetallic nanoclusters.
- The preference of preferred catalysts based on their natural potential of breaking the C-O bond on their surface is as follows: $Fe_{13}Ru_{42}$ > Ru_{55} > > $Ru_{13}Ni_{42}$ > Pd_{55} > $Co_{13}Ni_{55}$ > $Fe_{13}Ni_{42}$.

8.2 Future Work

The percentage difference for bimetallic 0.5 nm clusters needs to be done to compare with the bigger size clusters (1.2 nm). Also, the magnetic properties of clusters of both sizes could be worth exploring to see the effect of magnetism on CO adsorption and dissociation.

On 55 atom clusters to see the charge transfer induce activity, further analysis of the density of states (DOS) and d-band centers can be done.

Supported nanoclusters with Alumina, Titania, and graphene can be explored to see the effect of support on the catalytic activity. We can compare the effect of support on 55-atom clusters with the work done by Gyawali et al.[82] on 13-atom models.

Hydrogen assisted CO adsorption can be studied to explain the reaction kinetics of CO bond breaking on a nanocluster surface and to further explore the reaction mechanism of formation of hydrocarbons.

Although the 55-atom cluster is quite challenging due to its bigger size for DFT calculations, further identifying the particle size >2nm will help in a realistic understanding of the catalytic activity. Molecular dynamics can be used to see the stability of nanocluster size at the reaction temperature.

APPENDIX A

DATA FOR 55-ATOM CLUSTERS

1-T_s	2-T_s	3-B_s	4-B_s	5-H_s	6-H_s
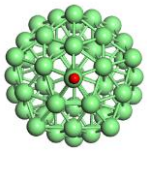	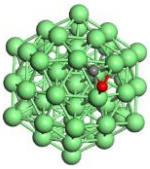	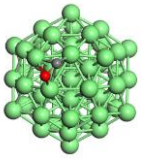	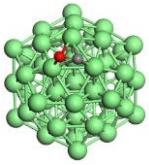	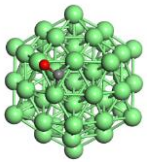	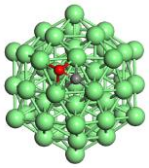
1-T_s	changed to 5-H_s	changed to 5-H_s	changed to 5-H_s	5-H_s	6-H_s
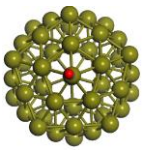	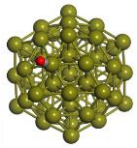	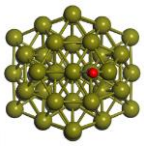	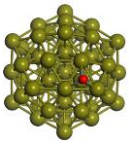	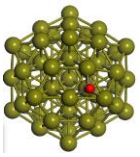	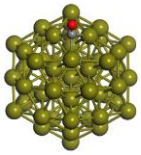
1-T_s	2-T_s	3-B_s	changed to 5-H_s	5-H_s	6-H_s
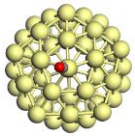	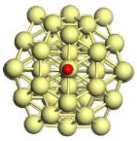	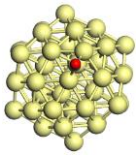	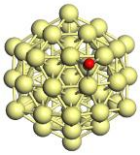		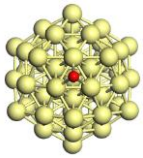
1-T_s	2-T_s	3-B_s	changed to 5-H_s	5-H_s	6-H_s
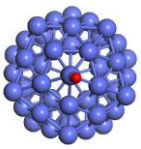	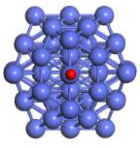	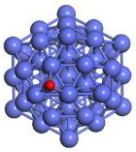	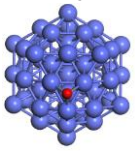	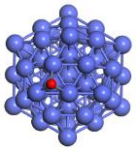	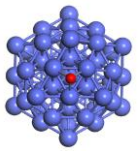
1-T_s	2-T_s	changed to 5-H_s	changed to 5-H_s	5-H_s	6-H_s
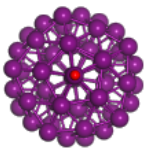	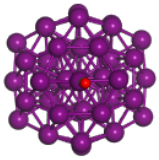	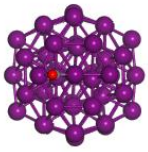	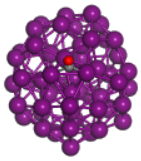	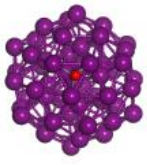	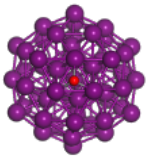
1-Ts	2-Ts	3-Bs	4-Bs	5-Bs	6-Bs

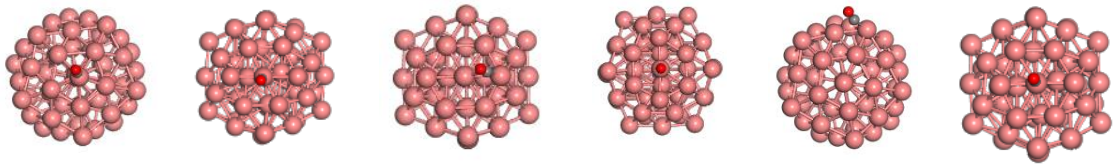

Figure A-1: CO adsorbed on all possible sites of 55 atom pure clusters. Ru, Pd, Ni, and Co are shown in light green, olive, pale yellow, and blue colors, respectively. (Clusters are shown in an orientation so that adsorbed CO can be seen clearly)

Table A-1: CO adsorption Energies (E_{ads}), C-O distances (Å) and C-M distances (Å) on all active sites (Top, Bridge, and Hollow), Preferred adsorption site(PAS-highlighted green), Bader charge (charge transferred to CO by the cluster), and Bond breaking Energies of CO($E_{barrier}$) on Binary 55-atom nanoclusters.

System		Adsorption sites						Bader (e)	$E_{barrier}$ (eV)
		1(T_s)	2(T_s)	3(B_s)	4(B_s)	5(H_s)	6(H_s)		
$Ru_{13}Pd_{42}$	E_{ads} (eV)	-1.39	-1.02	-1.48	-1.52	-1.58	-1.52	-0.26	3.85
	C-O (Å)	1.167	1.166	1.187	1.201	1.202	1.201		
	C-M(Å)	1.886	1.873	1.986	2.088	2.073	2.087		
$Ru_{13}Pt_{42}$	E_{ads} (eV)	-1.85	-1.29	-1.35	-1.23	-1.23	-1.01	-0.09	5.82
	C-O (Å)	1.169	1.166	1.190	1.204	1.204	1.202		
	C-M(Å)	1.864	1.860	2.010	2.118	2.119	2.133		
$Ru_{13}Fe_{42}$	E_{ads} (eV)	2.21	7.75	3.26	-0.90	1.37	-0.65	-0.44	3.32
	C-O (Å)	1.19	1.185	1.20	1.186	1.212	1.186		

Table A-2: Continued

	C-M(Å)	1.775	1.775	2.006	1.767	2.098	1.773		
$Ru_{13}Ni_{42}$	**E_{ads} (eV)**	-1.70	-1.49	-1.69	-1.56	-1.80	-1.68	-0.49	2.19
	C-O (Å)	1.171	1.171	1.171	1.197	1.21	1.209		
	C-M(Å)	1.758	1.755	1.758	1.884	1.950	1.960		
$Co_{13}Pd_{42}$	**E_{ads} (eV)**	-1.18	-1.24	-1.59	-1.21	-1.67	-0.68	-0.25	4.11
	C-O (Å)	1.166	1.167	1.187	1.201	1.2	1.201		
	C-M(Å)	1.880	1.867	1.990	2.082	2.076	2.083		
$Co_{13}Ni_{42}$	**E_{ads} (eV)**	-1.56	-1.50	-1.63	-1.69	-1.68	-1.56	-0.48	2.32
	C-O (Å)	1.171	1.171	1.191	1.206	1.206	1.206		
	C-M(Å)	1.755	1.747	1.882	1.961	1.961	1.970		
$Co_{13}Pt_{42}$	**E_{ads} (eV)**	-1.53	-1.60	-1.75	-1.64	-1.64	-1.64	-0.15	4.11
	C-O (Å)	1.169	1.167	1.188	1.20	1.20	1.20		
	C-M(Å)	1.851	1.837	2.018	2.125	2.127	2.126		
$Co_{13}Fe_{42}$	**E_{ads} (eV)**	4.26	-0.07	2.13	3.57	2.91	1.66	-0.33	4.62
	C-O (Å)	1.182	1.186	1.192	1.185	1.209	1.186		

Table A-3: Continued

	C-M(Å)	1.767	1.756	2.034	1.877	2.088	1.753		
$Ni_{13}Pd_{42}$	**E_{ads} (eV)**	-1.20	-1.22	-1.61	-1.57	-1.69	-1.74	-0.27	3.6
	C-O (Å)	1.166	1.167	1.187	1.19	1.201	1.202		
	C-M(Å)	1.882	1.868	1.988	2.000	2.077	2.081		
$Ni_{13}Pt_{42}$	**E_{ads} (eV)**	-1.58	-1.62	-1.76	-1.64	-1.63	-1.64	-0.15	4.23
	C-O (Å)	1.169	1.166	1.188	1.2	1.2	1.2		
	C-M(Å)	1.847	1.836	2.018	2.127	2.128	2.126		
$Ni_{13}Fe_{42}$	**E_{ads} (eV)**	2.12	-0.56	-0.86	4.41	-0.32	-0.54	-0.45	3.07
	C-O (Å)	1.18	1.183	1.187	1.207	1.215	1.21		
	C-M(Å)	1.780	1.770	1.761	1.969	2.022	2.074		
$Fe_{13}Ru_{42}$	**E_{ads} (eV)**	-1.73	-1.78	-1.80	-1.96	-1.97	-1.94	-0.47	0.68
	C-O (Å)	1.177	1.181	1.182	1.206	1.206	1.214		
	C-M(Å)	1.892	1.867	1.861	2.053	2.055	2.142		
$Fe_{13}Pd_{42}$	**E_{ads} (eV)**	-1.90	-0.41	-0.63	-1.18	-0.83	-2.42	-0.24	7.12
	C-O (Å)	1.167	1.167	1.188	1.19	1.2	1.201		

Table A-4: Continued

	C-M(Å)	1.893	1.876	1.988	2.002	2.074	2.083		
$Fe_{13}Pt_{42}$	E_{ads} **(eV)**	-4.62	-3.87	-2.00	-2.09	-3.77	-1.39	-0.01	7.85
	C-O (Å)	1.169	1.166	1.189	1.201	1.202	1.201		
	C-M(Å)	1.885	1.858	2.016	2.120	2.122	2.123		
$Fe_{13}Co_{42}$	E_{ads} **(eV)**	-1.35	-1.51	-1.37	-1.50	-1.45	-1.39	-0.33	2.79
	C-O (Å)	1.178	1.179	1.191	1.179	1.207	1.212		
	C-M(Å)	1.172	1.747	1.968	1.747	2.014	1.983		
$Fe_{13}Ni_{42}$	E_{ads} **(eV)**	-1.54	-1.39	-1.49	-1.60	-1.61	-1.48	-0.48	2.67
	C-O (Å)	1.171	1.171	1.192	1.206	1.206	1.208		
	C-M(Å)	1.761	1.757	1.880	1.963	1.962	1.967		
$Pt_{13}Pd_{42}$	E_{ads} **(eV)**	-1.56	-1.39	-1.71	-1.806	-1.807	-1.72	-0.26	3.81
	C-O (Å)	1.167	1.167	1.188	1.205	1.205	1.204		
	C-M(Å)	1.864	1.863	1.986	2.065	2.064	2.075		

Table A-5: Continued

$Pt_{13}Fe_{42}$	E_{ads} **(eV)**	0.86	-1.35	-4.69	-3.17	-3.91	-5.83	-0.39	
	C-O (Å)	1.181	1.184	1.185	1.191	1.191	1.186		
	C-M(Å)	1.765	1.775	1.762	1.742	2.080	1.774		

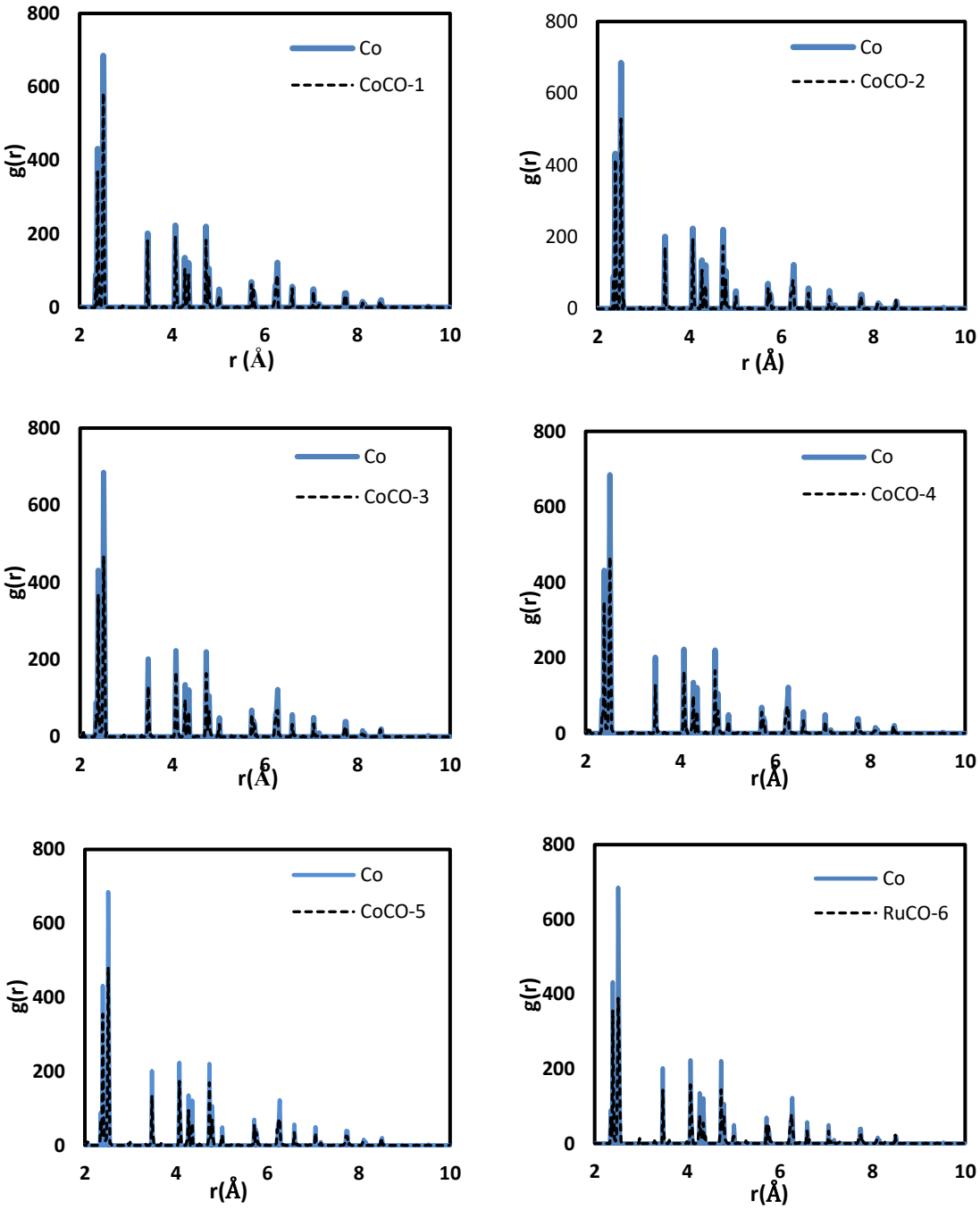

Figure A-2: Plots of Radial distribution function $g(r)$, relative to the center of geometry of bare and CO adsorbed on Co55 nanoclusters.

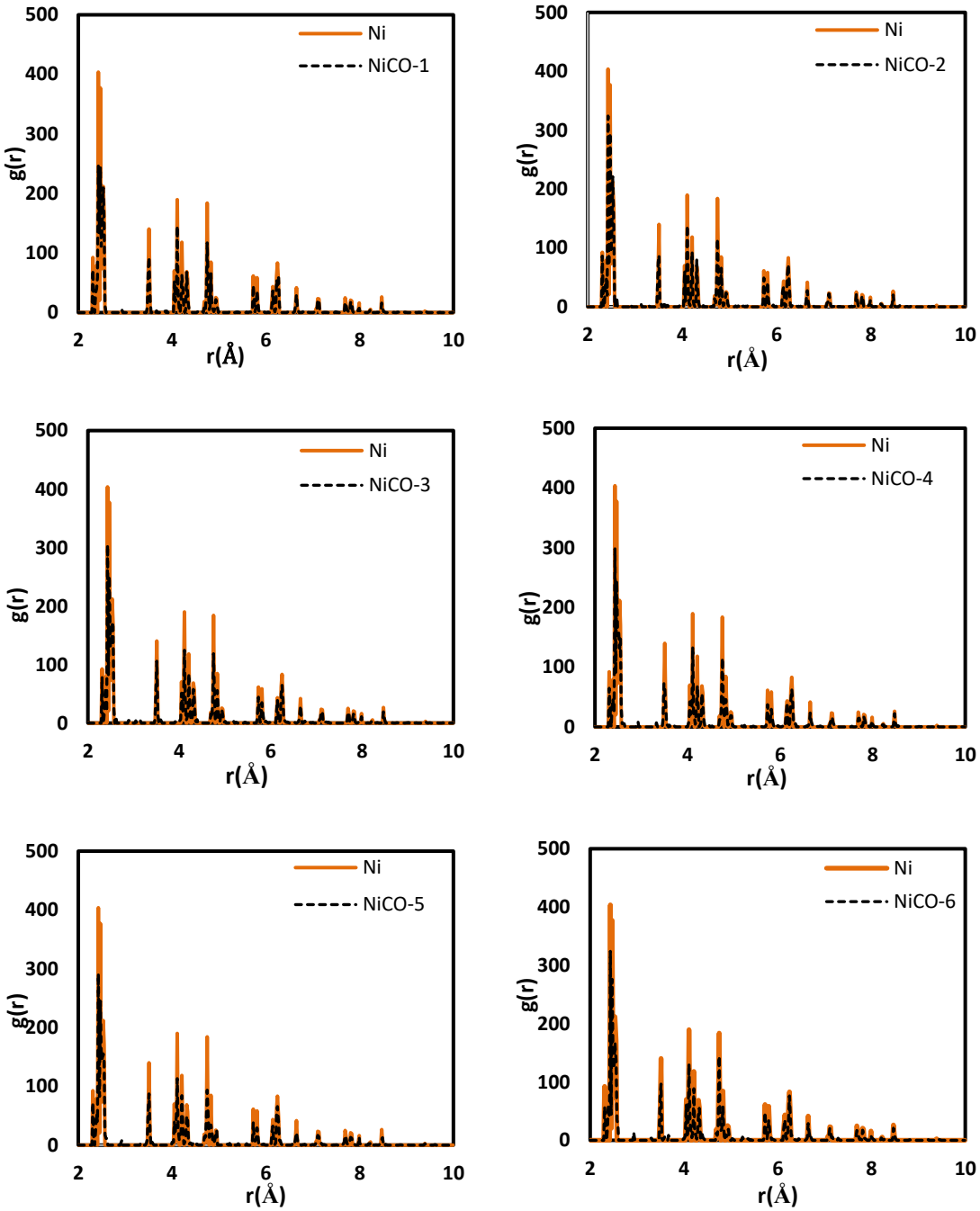

Figure A-3: Plots of Radial distribution function $g(r)$, relative to the center of geometry of bare and CO adsorbed on Ni55 nanoclusters.

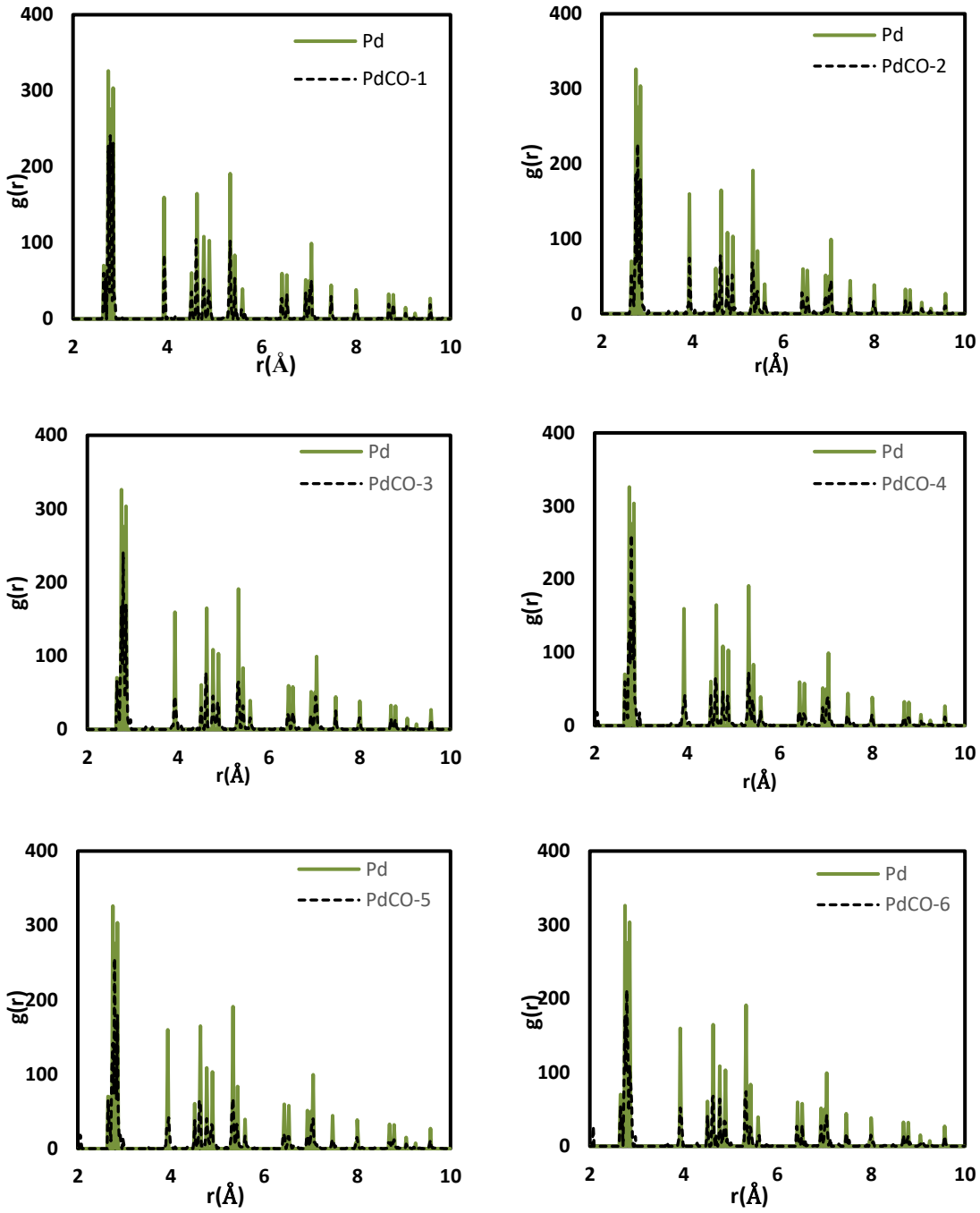

Figure A-4: Plots of Radial distribution function $g(r)$, relative to the center of geometry of bare and CO adsorbed on Pd55 nanoclusters.

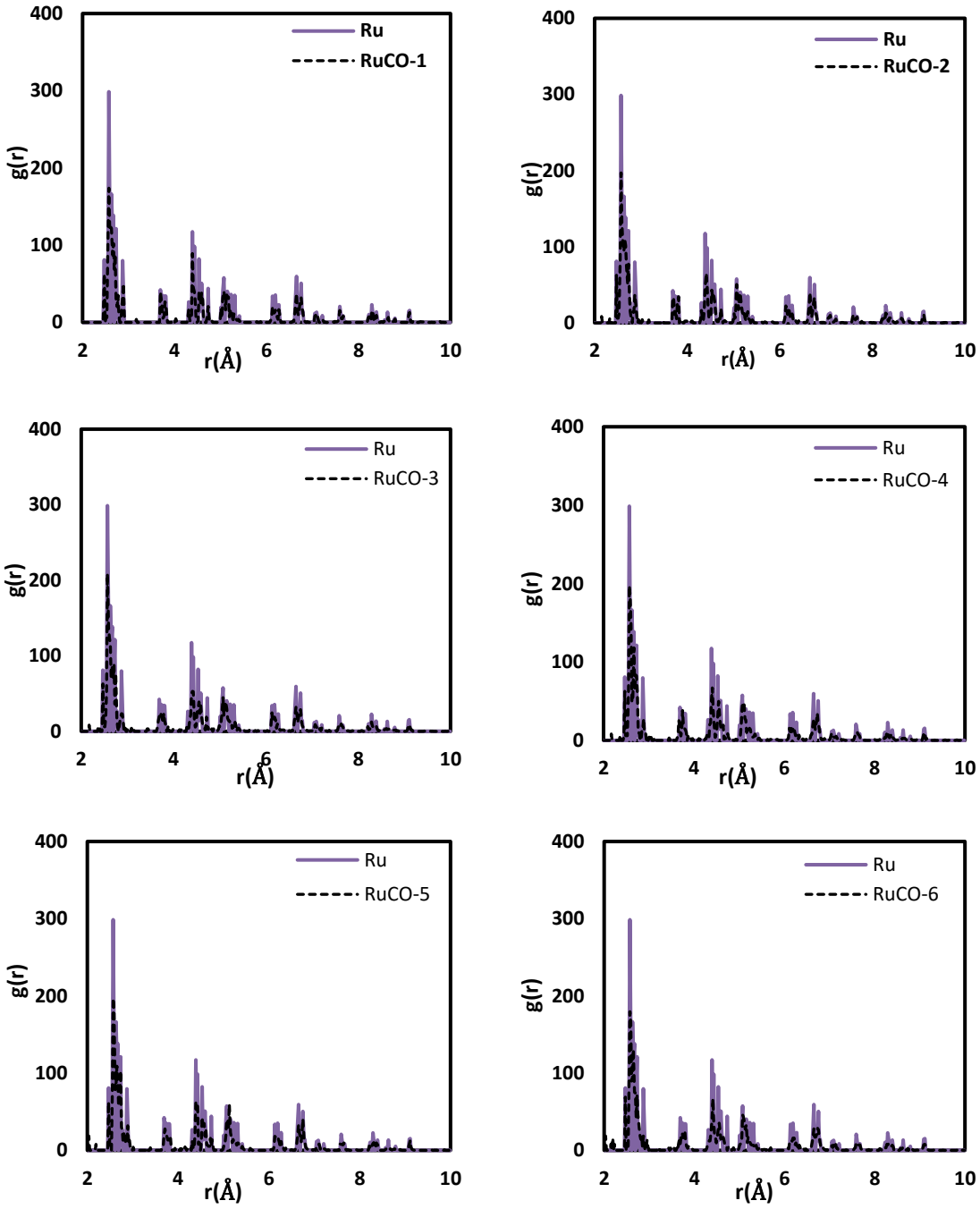

Figure A-5: Plots of Radial distribution function $g(r)$, relative to the center of geometry of bare and CO adsorbed on Ru55 nanoclusters.

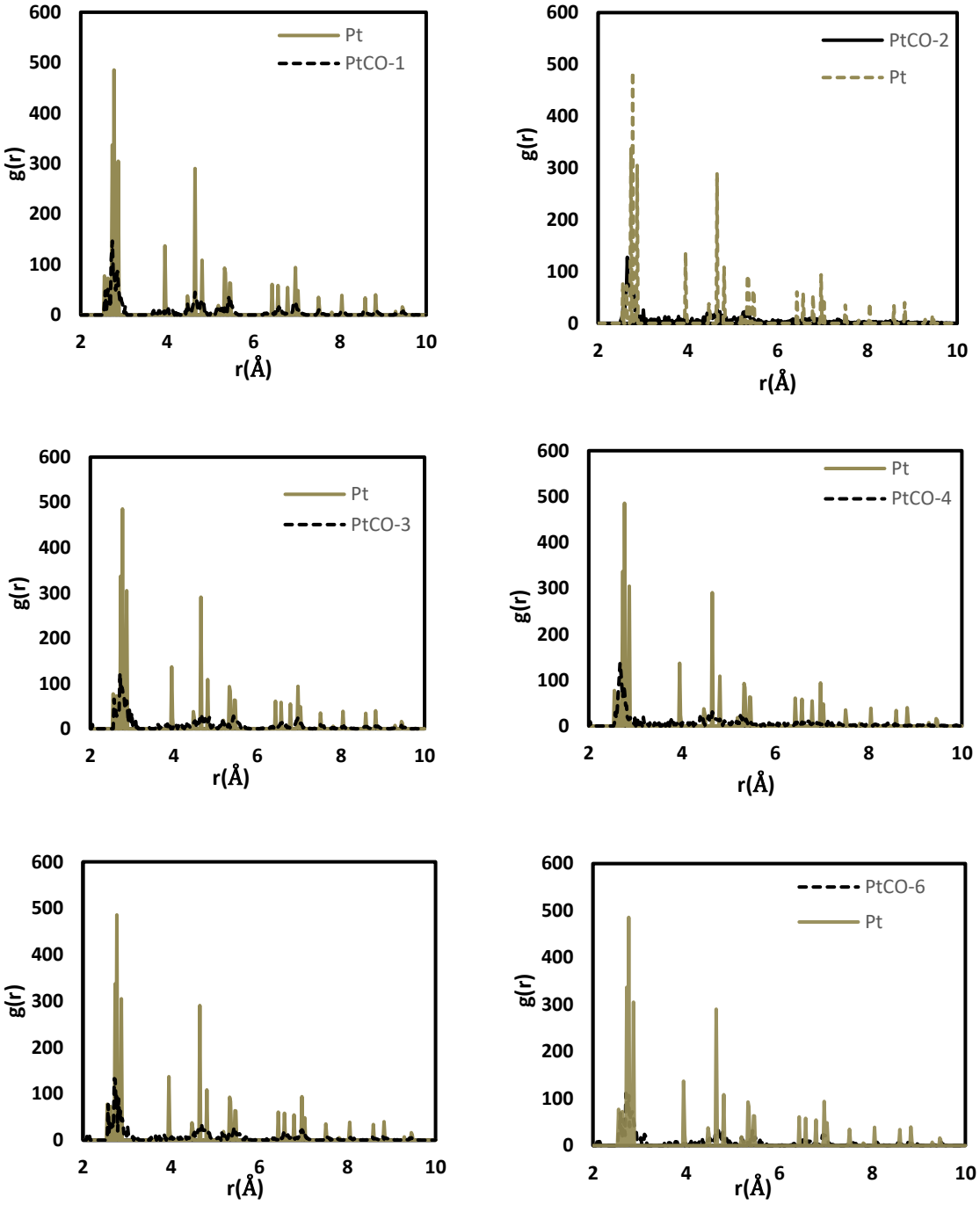

Figure A-6: Plots of Radial distribution function $g(r)$, relative to the center of geometry of bare and CO adsorbed on Pt55 nanoclusters.

BIBLIOGRAPHY

[1] A. Y. Khodakov, W. Chu, and P. Fongarland, "Advances in the development of novel cobalt Fischer-Tropsch catalysts for synthesis of long-chain hydrocarbons and clean fuels," *Chem. Rev.*, vol. 107, no. 5, pp. 1692–1744, 2007, doi: 10.1021/cr050972v.

[2] S. Kocic, "Activity and selectivity loss modelling on Co based Fischer-Tropsch catalysts." Université de Lyon, 2019.

[3] J. K. Nørskov, F. Abild-Pedersen, F. Studt, and T. Bligaard, "Density functional theory in surface chemistry and catalysis," *Proc. Natl. Acad. Sci. U. S. A.*, vol. 108, no. 3, pp. 937–943, 2011, doi: 10.1073/pnas.1006652108.

[4] H. Jahangiri, J. Bennett, P. Mahjoubi, K. Wilson, and S. Gu, "A review of advanced catalyst development for Fischer-Tropsch synthesis of hydrocarbons from biomass derived syn-gas," *Catal. Sci. Technol.*, vol. 4, no. 8, pp. 2210–2229, 2014, doi: 10.1039/c4cy00327f.

[5] J. Van de Loosdrecht *et al.*, "Fischer-Tropsch synthesis: catalysts and chemistry," in *Comprehensive Inorganic Chemistry II: from elements to applications*, Elsevier, 2013, pp. 525–557.

[6] J. Van De Loosdrecht, S. Technology, and S. Africa, *Fischer – Tropsch Synthesis : Catalysts and Chemistry*. Elsevier Ltd., 2013.

[7] A. A. Adesina, "Hydrocarbon synthesis via Fischer-Tropsch reaction : travails and triumphs," vol. 138, pp. 345–367, 1996.

[8] M. Zhuo, K. F. Tan, A. Borgna, and M. Saeys, "Density functional theory study of the co insertion mechanism for Fischer-Tropsch synthesis over co catalysts," *J. Phys. Chem. C*, vol. 113, no. 19, pp. 8357–8365, 2009, doi: 10.1021/jp900281h.

[9] A. de Klerk, "Fischer–Tropsch Process," *Kirk-Othmer Encycl. Chem. Technol.*, pp. 1–20, 2000.

[10] D. Leckel, "Diesel production from Fischer - Tropsch: The past, the present, and new concepts," *Energy and Fuels*, vol. 23, no. 5, pp. 2342–2358, 2009, doi: 10.1021/ef900064c.

[11] G. Rothenberg, *Catalysis:Concepts and Green Applications*. John Wiley & Sons, 2017.

[12] A. E. De Paepe *et al.*, *The Chemistry of the Catalyzed Hydrogenation of Carbon Monoxide*, vol. 53, no. 9. 2019.

[13] H. H. Storch, *The Fischer-Tropsch and related syntheses: including a summary of theoretical and applied contact catalysis*. Wiley, 1951.

[14] H. Mahmoudi, M. Mahmoudi, O. Doustdar, and H. Jahangiri, "A review of Fischer Tropsch synthesis process , mechanism , surface chemistry and catalyst formulation," pp. 11–31, 2017.

[15] B. Todic, W. Ma, G. Jacobs, B. H. Davis, and D. B. Bukur, "CO-insertion mechanism based kinetic model of the Fischer-Tropsch synthesis reaction over Re-promoted Co catalyst," *Catal. Today*, vol. 228, pp. 32–39, 2014, doi: 10.1016/j.cattod.2013.08.008.

[16] Z.-P. Liu and P. Hu, "A new insight into Fischer− Tropsch synthesis," *J. Am. Chem. Soc.*, vol. 124, no. 39, pp. 11568–11569, 2002.

[17] S. Paul, K. Momeni, and V. Levitas, "Shear-induced diamondization of multilayer graphene structures: A computational study," *Carbon N. Y.*, 2020.

[18] S. Paul and K. Momeni, "Mechanochemistry of stable diamane and atomically thin diamond films synthesis from bi-and multilayer graphene: a computational study," *J. Phys. Chem. C*, vol. 123, no. 25, pp. 15751–15760, 2019.

[19] K. Momeni *et al.*, "Multiscale computational understanding and growth of 2D materials: a review," *npj Comput. Mater.*, vol. 6, no. 1, pp. 1–18, 2020.

[20] J. Cheng, P. Hu, P. Ellis, S. French, G. Kelly, and C. M. Lok, "Some understanding of Fischer–Tropsch synthesis from density functional theory calculations," *Top. Catal.*, vol. 53, no. 5–6, pp. 326–337, 2010.

[21] R. G. Parr and Y. Weitao, *Density-Functional Theory of Atoms and Molecules*. Oxford University Press, 1994.

[22] V. Fernandez *et al.*, "A Photoelectron Diffraction Study of the Pd {111}(√ 3x√ 3) R30°-CO Chemisorption Phase," *Zeitschrift für Phys. Chemie*, vol. 198, no. 1–2, pp. 73–85, 1997.

[23] H. Conrad, G. Ertl, and J. Küppers, "Interactions between oxygen and carbon monoxide on a Pd (111) surface," *Surf. Sci.*, vol. 76, no. 2, pp. 323–342, 1978.

[24] V. R. Calderone, N. R. Shiju, D. C. Ferré, and G. Rothenberg, “Bimetallic catalysts for the Fischer–Tropsch reaction,” *Green Chem.*, vol. 13, no. 8, pp. 1950–1959, 2011, doi: 10.1039/c0gc00919a.

[25] X. Ma, Q. Sun, F. Cao, W. Ying, and D. Fang, “Effects of the different supports on the activity and selectivity of iron-cobalt bimetallic catalyst for Fischer-Tropsch synthesis,” *J. Nat. gas Chem.*, vol. 15, no. 4, pp. 335–339, 2006.

[26] P. J. Feibelman *et al.*, “The CO/Pt(111) Puzzle a,” *J. Phys. Chem. B*, vol. 105, no. 18, pp. 4018–4025, 2001, doi: 10.1021/jp002302t.

[27] G. Sitja and C. R. Henry, “Molecular Beam Study of the CO Adsorption on a Regular Array of PdAu Clusters on Alumina,” *J. Phys. Chem. C*, vol. 123, no. 13, pp. 7961–7967, 2019, doi: 10.1021/acs.jpcc.8b07350.

[28] M. Meunier, “Guest Editorial: Industrial Applications of Molecular Simulation,” *Mol. Simul.*, vol. 32, no. 2, pp. 71–72, Feb. 2006, doi: 10.1080/08927020600710900.

[29] M. Zhang and R. Fournier, “Structure of 55-atom bimetallic clusters,” *J. Mol. Struct. THEOCHEM*, vol. 762, no. 1–3, pp. 49–56, 2006, doi: 10.1016/j.theochem.2005.08.042.

[30] J. P. K. Doye and L. Meyer, “The structure of binary Lennard-Jones clusters: The effects of atomic size ratio,” pp. 1–13, 2006.

[31] F. Baletto and R. Ferrando, “Structural properties of nanoclusters: Energetic, thermodynamic, and kinetic effects,” *Rev. Mod. Phys.*, vol. 77, no. 1, pp. 371–423, 2005, doi: 10.1103/RevModPhys.77.371.

[32] R. Ferrando, J. Jellinek, and R. L. Johnston, “Nanoalloys: From theory to applications of alloy clusters and nanoparticles,” *Chem. Rev.*, vol. 108, no. 3, pp. 845–910, 2008, doi: 10.1021/cr040090g.

[33] L. Liu and A. Corma, “Metal Catalysts for Heterogeneous Catalysis: From Single Atoms to Nanoclusters and Nanoparticles,” *Chem. Rev.*, vol. 118, no. 10, pp. 4981–5079, 2018, doi: 10.1021/acs.chemrev.7b00776.

[34] D. Guedes-Sobrinho, R. L. H. Freire, A. S. Chaves, and J. L. F. Da Silva, “Ab Initio Investigation of the Role of CO Adsorption on the Physical Properties of 55-Atom PtCo Nanoalloys,” *J. Phys. Chem. C*, vol. 121, no. 49, pp. 27721–27732, 2017, doi: 10.1021/acs.jpcc.7b09243.

[35] B. Delley, “From molecules to solids with the DMol3 approach,” *J. Chem. Phys.*, vol. 113, no. 18, pp. 7756–7764, 2000, doi: 10.1063/1.1316015.

[36] J. Hafner and G. Kresse, “The Vienna AB-Initio Simulation Program VASP: An Efficient and Versatile Tool for Studying the Structural, Dynamic, and Electronic Properties of Materials BT - Properties of Complex Inorganic Solids,” A. Gonis, A. Meike, and P. E. A. Turchi, Eds. Boston, MA: Springer US, 1997, pp. 69–82.

[37] V. E. R. F. Nalewajski *et al.*, “Density Functional Theory III Interpretation , Atoms , Molecules.”

[38] F. Giustino, A. Roy, R. G. Parr, and Y. Weitao, *Density-Functional Theory of Atoms and Molecules*. Oxford University Press, 2014.

[39] M. Born and R. Oppenheimer, “Zur quantentheorie der molekeln,” *Ann. Phys.*, vol. 389, no. 20, pp. 457–484, 1927.

[40] A. Fortunelli and G. Barcaro, “Metal Clusters and Nanoalloys,” in *Metal Clusters and Nanoalloys*, 2013, p. 243.

[41] P. Hohenberg and W. Kohn, “Inhomogeneous electron gas,” *Phys. Rev.*, vol. 136, no. 3B, p. B864, 1964.

[42] A. Roy, *Theoretical and Computational Developments in Modern Density Functional Theory*. Nova Science Publishers, 2012.

[43] W. Kohn and L. J. Sham, “Self-consistent equations including exchange and correlation effects,” *Phys. Rev.*, vol. 140, no. 4A, p. A1133, 1965.

[44] N. Mardirossian and M. Head-Gordon, “Thirty years of density functional theory in computational chemistry: An overview and extensive assessment of 200 density functionals,” *Mol. Phys.*, vol. 115, no. 19, pp. 2315–2372, 2017, doi: 10.1080/00268976.2017.1333644.

[45] J. P. Perdew *et al.*, “Atoms, molecules, solids, and surfaces: Applications of the generalized gradient approximation for exchange and correlation,” *Phys. Rev. B*, vol. 48, no. 7, p. 4978, 1993, doi: 10.1103/PhysRevB.48.4978.2.

[46] J. P. Perdew, K. Burke, and M. Ernzerhof, “Generalized gradient approximation made simple,” *Phys. Rev. Lett.*, vol. 77, no. 18, pp. 3865–3868, 1996, doi: 10.1103/PhysRevLett.77.3865.

[47] B. Hammer, L. B. Hansen, and J. K. Nørskov, “Improved adsorption energetics within density-functional theory using revised Perdew-Burke-Ernzerhof functionals,” *Phys. Rev. B - Condens. Matter Mater. Phys.*, vol. 59, no. 11, pp. 7413–7421, 1999, doi: 10.1103/PhysRevB.59.7413.

[48] F. Abild-Pedersen and M. P. Andersson, “CO adsorption energies on metals with correction for high coordination adsorption sites - A density functional

study," *Surf. Sci.*, vol. 601, no. 7, pp. 1747–1753, 2007, doi: 10.1016/j.susc.2007.01.052.

[49] E. G. Lewars, *Computational Chemistry. Introduction to the Theory and Applications of Molecular and Quantum Mechanics*, vol. 43, no. 38. 2004.

[50] S. Huzinaga, "Basis sets for molecular calculations," *Comput. Phys. Reports*, vol. 2, no. 6, pp. 281–339, 1985, doi: https://doi.org/10.1016/0167-7977(85)90003-6.

[51] A. E. Mattsson, P. A. Schultz, M. P. Desjarlais, T. R. Mattsson, and K. Leung, "Designing meaningful density functional theory calculations in materials science - A primer," *Model. Simul. Mater. Sci. Eng.*, vol. 13, no. 1, 2005, doi: 10.1088/0965-0393/13/1/R01.

[52] E. R. Davidson and D. Feller, "Basis Set Selection for Molecular Calculations," *Chem. Rev.*, vol. 86, no. 4, pp. 681–696, 1986, doi: 10.1021/cr00074a002.

[53] W. J. Hehre, K. Ditchfield, and J. A. Pople, "Self-consistent molecular orbital methods. XII. Further extensions of gaussian-type basis sets for use in molecular orbital studies of organic molecules," *J. Chem. Phys.*, vol. 56, no. 5, pp. 2257–2261, 1972, doi: 10.1063/1.1677527.

[54] M. M. Francl *et al.*, "Self-consistent molecular orbital methods. XXIII. A polarization-type basis set for second-row elements," *J. Chem. Phys.*, vol. 77, no. 7, pp. 3654–3665, 1982, doi: 10.1063/1.444267.

[55] R. Fournier, J. Andzelm, D. R. Salahub, R. Fournier, J. Andzelm, and D. R. Salahub, "Analytical gradient of the linear combination of Gaussiantype orbitals — local spin density energy Analytical gradient of the linear combination of Gaussian-type orbitals-local spin density energy," vol. 6371, no. 1989, 2001, doi: 10.1063/1.456354.

[56] N. W. Ashcroft and N. D. Mermin, *Solid State Physics*. Holt, Rinehart and Winston, 1976.

[57] M. C. Payne, M. P. Teter, D. C. Allan, T. A. Arias, and J. D. Joannopoulos, "Iterative minimization techniques for ab initio total-energy calculations: Molecular dynamics and conjugate gradients," *Rev. Mod. Phys.*, vol. 64, no. 4, pp. 1045–1097, 1992, doi: 10.1103/RevModPhys.64.1045.

[58] I. J. Robertson and M. C. Payne, "K-point sampling and the k.p method in pseudopotential total energy calculations," *J. Phys. Condens. Matter*, vol. 2, no. 49, pp. 9837–9852, 1990, doi: 10.1088/0953-8984/2/49/010.

[59] P. Kratzer and J. Neugebauer, “The basics of electronic structure theory for periodic systems,” *Front. Chem.*, vol. 7, no. MAR, pp. 1–18, 2019, doi: 10.3389/fchem.2019.00106.

[60] J. D. Pack and H. J. Monkhorst, “Special points for Brillouin-zone integrations,” *Phys. Rev. B*, vol. 13, no. 12, pp. 1748–1749, 1977, doi: 10.1103/PhysRevB.16.1748.

[61] D. J. Chadi and M. L. Cohen, “Special points in the brillouin zone,” *Phys. Rev. B*, vol. 8, no. 12, pp. 5747–5753, 1973, doi: 10.1103/PhysRevB.8.5747.

[62] A. Baldereschi, “Mean-value point in the Brillouin zone,” *Phys. Rev. B*, vol. 7, no. 12, pp. 5212–5215, 1973, doi: 10.1103/PhysRevB.7.5212.

[63] J. C. Phillips, “Energy-band interpolation scheme based on a pseudopotential,” *Phys. Rev.*, vol. 112, no. 3, pp. 685–695, 1958, doi: 10.1103/PhysRev.112.685.

[64] N. Troullier and J. L. Martins, “Efficient pseudopotentials for plane-wave calculations,” *Phys. Rev. B*, vol. 43, no. 3, pp. 1993–2006, 1991, doi: 10.1103/PhysRevB.43.1993.

[65] P. E. Blöchl, “Projector augmented-wave method,” *Phys. Rev. B*, vol. 50, no. 24, pp. 17953–17979, 1994, doi: 10.1103/PhysRevB.50.17953.

[66] D. Joubert, “From ultrasoft pseudopotentials to the projector augmented-wave method,” *Phys. Rev. B - Condens. Matter Mater. Phys.*, vol. 59, no. 3, pp. 1758–1775, 1999, doi: 10.1103/PhysRevB.59.1758.

[67] D. Vanderbilt, “Soft self-consistent pseudopotentials in a generalized eigenvalue formalism,” *Phys. Rev. B*, vol. 41, no. 11, p. 7892, 1990.

[68] G. B. Bachelet and M. Schlüter, “Relativistic norm-conserving pseudopotentials,” *Phys. Rev. B*, vol. 25, no. 4, pp. 2103–2108, 1982, doi: 10.1103/PhysRevB.25.2103.

[69] K. J. Laidler and M. C. King, “The development of transition-state theory,” *J. Phys. Chem.*, vol. 87, no. 15, pp. 2657–2664, 1983, doi: 10.1021/j100238a002.

[70] H. Jónsson, G. Mills, and K. W. Jacobsen, “Nudged elastic band method for finding minimum energy paths of transitions,” in *Classical and Quantum Dynamics in Condensed Phase Simulations*, 1988, p. 385.

[71] G. Henkelman, B. P. Uberuaga, and H. Jónsson, “Climbing image nudged elastic band method for finding saddle points and minimum energy paths,” *J. Chem. Phys.*, vol. 113, no. 22, pp. 9901–9904, 2000, doi: 10.1063/1.1329672.

[72] N. Govind, M. Petersen, G. Fitzgerald, D. King-Smith, and J. Andzelm, “A generalized synchronous transit method for transition state location,” *Comput. Mater. Sci.*, vol. 28, no. 2, pp. 250–258, 2003, doi: 10.1016/S0927-0256(03)00111-3.

[73] C. Peng and H. Bernhard Schlegel, “Combining synchronous transit and quasi-newton methods to find transition states,” *Isr. J. Chem.*, vol. 33, no. 4, pp. 449–454, 1993.

[74] H. S. Ahn, S. C. Lee, S. Han, K. R. Lee, and D. Y. Kim, “Ab initio study of the effect of nitrogen on carbon nanotube growth,” *Nanotechnology*, vol. 17, no. 3, pp. 909–912, 2006, doi: 10.1088/0957-4484/17/3/048.

[75] K. Momma and F. Izumi, “VESTA 3 for three-dimensional visualization of crystal, volumetric and morphology data,” *J. Appl. Crystallogr.*, vol. 44, no. 6, pp. 1272–1276, 2011.

[76] F. Aguilera-Granja, J. M. Montejano-Carrizalez, and R. A. Guirado-López, “Magnetic properties of small 3d and 4d transition metal clusters: The role of a noncompact growth,” *Phys. Rev. B - Condens. Matter Mater. Phys.*, vol. 73, no. 11, pp. 1–10, 2006, doi: 10.1103/PhysRevB.73.115422.

[77] M. J. Piotrowski, P. Piquini, and J. L. F. Da Silva, “Platinum-based nanoalloys Pt nTM 55- n (TM = Co, Rh, Au): A density functional theory investigation,” *J. Phys. Chem. C*, vol. 116, no. 34, pp. 18432–18439, 2012, doi: 10.1021/jp302844f.

[78] E. Aprà and A. Fortunelli, “Density-functional calculations on platinum nanoclusters: Pt 13, Pt 38, and Pt 55,” *J. Phys. Chem. A*, vol. 107, no. 16, pp. 2934–2942, 2003, doi: 10.1021/jp0275793.

[79] N. S. Froemming and G. Henkelman, “Optimizing core-shell nanoparticle catalysts with a genetic algorithm,” *J. Chem. Phys.*, vol. 131, no. 23, pp. 1–7, 2009, doi: 10.1063/1.3272274.

[80] C. A. Welker, “Ruthenium Based Fischer-Tropsch Synthesis on Crystallites and Clusters of Different Sizes from ‘Nano’ To ‘Ångstrøm,’” *Univeristy Cape T.*, no. August, pp. 1–225, 2007.

[81] I. V. Yudanov, A. Genest, S. Schauermann, H. J. Freund, and N. Rösch, “Size Dependence of the adsorption energy of CO on metal nanoparticles: A DFT search for the minimum value,” *Nano Lett.*, vol. 12, no. 4, pp. 2134–2139, 2012, doi: 10.1021/nl300515z.

[82] A. V. Ruban, H. L. Skriver, and J. K. Nørskov, “Local equilibrium properties of metallic surface alloys,” in *Chemical Physics of Solid Surfaces*, vol. 10, no. C, 2002, pp. 1–29.

[83] S. Gyawali, S. Godara, F. A. Soto, and D. S. Mainardi, “In search of initial predictors of fischer-tropsch catalytic activity,” *IEEE Trans. Nanotechnol.*, vol. 15, no. 5, pp. 738–745, 2016, doi: 10.1109/TNANO.2016.2531423.

[84] P. C. D. Mendes *et al.*, “Ab Initio Insights into the Formation Mechanisms of 55-Atom Pt-Based Core-Shell Nanoalloys,” *J. Phys. Chem. C*, 2020, doi: 10.1021/acs.jpcc.9b09561.

[85] G. P. V. A. N. D. E. R. Laan and A. A. C. M. Beenackers, “Kinetics and Selectivity of the Fischer – Tropsch Synthesis : A Literature Review Kinetics and Selectivity of the Fischer – Tropsch Synthesis : A Literature,” vol. 4940, 2011, doi: 10.1081/CR-100101170.

[86] J. L. F. Da Silva, H. G. Kim, M. J. Piotrowski, M. J. Prieto, and G. Tremiliosi-Filho, “Reconstruction of core and surface nanoparticles: The example of Pt 55 and Au55,” *Phys. Rev. B - Condens. Matter Mater. Phys.*, vol. 82, no. 20, pp. 1–6, 2010, doi: 10.1103/PhysRevB.82.205424.

[87] N. Marinkovic, K. Sasaki, and R. Adzic, “Nanoparticle size evaluation of catalysts by EXAFS: Advantages and limitations,” *Zast. Mater.*, vol. 57, no. 1, pp. 101–109, 2016, doi: 10.5937/zasmat1601101m.

[88] T. Björkman and O. Grånäs, “Adaptive smearing for Brillouin zone integration,” *Int. J. Quantum Chem.*, vol. 111, no. 5, pp. 1025–1030, 2011.

[89] Z. Yang, Q. Wang, X. Shan, W. Q. Li, G. H. Chen, and H. Zhu, “DFT study of Fe-Ni core-shell nanoparticles: Stability, catalytic activity, and interaction with carbon atom for single-walled carbon nanotube growth,” *J. Chem. Phys.*, vol. 142, no. 7, 2015, doi: 10.1063/1.4907897.

[90] K. E. A. Batista, M. J. Piotrowski, A. S. Chaves, and J. L. F. Da Silva, “A theoretical investigation of the structural and electronic properties of 55-atom nanoclusters: The examples of Y-Tc and Pt,” *J. Chem. Phys.*, vol. 144, no. 5, 2016, doi: 10.1063/1.4941295.

[91] M. J. Piotrowski *et al.*, “Theoretical study of the structural, energetic, and electronic properties of 55-atom metal nanoclusters: A DFT investigation within van der waals corrections, spin−Orbit coupling, and PBE+U of 42 metal systems,” *J. Phys. Chem. C*, vol. 120, no. 50, pp. 28844–28856, 2016, doi: 10.1021/acs.jpcc.6b10404.

[92] R. Vardi, L. Rubinovich, and M. Polak, “On the use of corrected cohesion energies in model computations of transition metal properties: The case of Pt-Rh cluster compositional structures,” *Surf. Sci.*, vol. 602, no. 5, pp. 1040–1044, 2008, doi: 10.1016/j.susc.2007.12.024.

[93] D. R. Lide, *CRC handbook of chemistry and physics: a ready-reference book of chemical and physical data*. CRC press, 1995.

[94] G. Lanzani, A. G. Nasibulin, K. Laasonen, and E. I. Kauppinen, “CO dissociation and CO+O reactions on a nanosized iron cluster,” *Nano Res.*, vol. 2, no. 8, pp. 660–670, 2009, doi: 10.1007/s12274-009-9069-9.

[95] K. M. Gameel, I. M. Sharafeldin, and N. K. Allam, “First-principles descriptors of CO chemisorption on Ni and Cu surfaces,” *Phys. Chem. Chem. Phys.*, vol. 21, no. 21, pp. 11476–11487, 2019, doi: 10.1039/c9cp00881k.

[96] I. V. Yudanov *et al.*, “CO adsorption on Pd nanoparticles: Density functional and vibrational spectroscopy studies,” *J. Phys. Chem. B*, vol. 107, no. 1, pp. 255–264, 2003, doi: 10.1021/jp022052b.

[97] A. M. Bradshaw and F. M. Hoffmann, “The chemisorption of carbon monoxide on palladium single crystal surfaces: IR spectroscopic evidence for localised site adsorption,” *Surf. Sci.*, vol. 72, no. 3, pp. 513–535, 1978.

[98] X. Guo and J. T. Yates Jr, “Dependence of effective desorption kinetic parameters on surface coverage and adsorption temperature: CO on Pd (111),” *J. Chem. Phys.*, vol. 90, no. 11, pp. 6761–6766, 1989.

[99] K. Christmann, O. Schober, and G. Ertl, “Adsorption of CO on a Ni(111) surface,” *J. Chem. Phys.*, vol. 4719, no. 111, pp. 4719–4724, 1974, doi: 10.1063/1.1680972.

[100] H. Conrad, G. Ertl, J. Küppers, and E. E. Latta, “Adsorption of CO on clean and oxygen covered Ni(111) surfaces,” *Surf. Sci.*, vol. 57, no. 2, pp. 475–484, 1976, doi: 10.1016/0039-6028(76)90341-1.

[101] S. E. Mason, I. Grinberg, and A. M. Rappe, “First-principles extrapolation method for accurate CO adsorption energies on metal surfaces,” *Phys. Rev. B - Condens. Matter Mater. Phys.*, vol. 69, no. 16, pp. 1–4, 2004, doi: 10.1103/PhysRevB.69.161401.

[102] J. Carrasco, L. Barrio, P. Liu, J. A. Rodriguez, and M. V. Ganduglia-Pirovano, “Theoretical studies of the adsorption of CO and C on Ni(111) and Ni/CeO2(111): Evidence of a strong metal-support interaction,” *J. Phys. Chem. C*, vol. 117, no. 16, pp. 8241–8250, 2013, doi: 10.1021/jp400430r.

[103] S. Dobrin, “CO oxidation on Pt nanoclusters, size and coverage effects: A density functional theory study,” *Phys. Chem. Chem. Phys.*, vol. 14, no. 35, pp. 12122–12129, 2012, doi: 10.1039/c2cp41286a.

[104] S. Korniy, “A Theoretical Study of CO Adsorption on Pt-Me (Me- Fe , Co , Ni),” *J. Thermodyn. Catal.*, vol. 7, no. 2, pp. 2–5, 2016, doi: 10.4172/2160-7544.1000169.

[105] H. Orita, N. Itoh, and Y. Inada, “All electron scalar relativistic calculations on adsorption of CO on Pt(1 1 1) with full-geometry optimization: A correct

estimation for CO site-preference," *Chem. Phys. Lett.*, vol. 384, no. 4–6, pp. 271–276, 2004, doi: 10.1016/j.cplett.2003.12.034.

[106] Y. Wang, S. De Gironcoli, N. S. Hush, and J. R. Reimers, "Successful a priori modeling of CO adsorption on Pt(111) using periodic hybrid density functional theory," *J. Am. Chem. Soc.*, vol. 129, no. 34, pp. 10402–10407, 2007, doi: 10.1021/ja0712367.

[107] J. X. Liu, B. Y. Zhang, P. P. Chen, H. Y. Su, and W. X. Li, "CO dissociation on face-centered cubic and hexagonal close-packed nickel catalysts: A first-principles study," *J. Phys. Chem. C*, vol. 120, no. 43, pp. 24895–24903, 2016, doi: 10.1021/acs.jpcc.6b08742.

[108] W. Tang, E. Sanville, and G. Henkelman, "A grid-based Bader analysis algorithm without lattice bias," *J. Phys. Condens. Matter*, vol. 21, no. 8, 2009, doi: 10.1088/0953-8984/21/8/084204.

[109] E. Sanville, S. D. Kenny, R. Smith, and G. Henkelman, "Improved Grid-Based Algorithm for Bader Charge Allocation," 2007, doi: 10.1002/jcc.

[110] G. Henkelman, "A fast and robust algorithm for Bader decomposition of charge density," vol. 36, pp. 354–360, 2006, doi: 10.1016/j.commatsci.2005.04.010.

[111] M. Yu, D. R. Trinkle, and I. Introduction, "Accurate and efficient algorithm for Bader charge integration," vol. 064111, pp. 1–8, 2011, doi: 10.1063/1.3553716.

[112] K. Kelsey and B. Duff, "Predicting Transitions in Fischer-Tropsch Reactors," no. May, 2019.

[113] M. Mansouri, H. Atashi, and A. A. Mirzaei, "Hydrogenation of CO on Cobalt Catalyst in Fischer–Tropsch Synthesis," *J. Thermodyn. Catal.*, vol. 03, no. 02, 2012, doi: 10.4172/2157-7544.1000113.

[114] "an Investigation of Fischer-Tropsch Reaction for Synthesis of," 2009.

[115] B. Zijlstra, R. J. P. Broos, W. Chen, I. A. W. Filot, and E. J. M. Hensen, "First-principles based microkinetic modeling of transient kinetics of CO hydrogenation on cobalt catalysts," *Catal. Today*, vol. 342, pp. 131–141, 2020, doi: 10.1016/j.cattod.2019.03.002.

[116] A. Fernando, K. L. D. M. Weerawardene, N. V Karimova, and C. M. Aikens, "Quantum mechanical studies of large metal, metal oxide, and metal chalcogenide nanoparticles and clusters," *Chem. Rev.*, vol. 115, no. 12, pp. 6112–6216, 2015.

[117] M. Sankar, N. Dimitratos, P. J. Miedziak, P. P. Wells, C. J. Kiely, and G. J. Hutchings, “Designing bimetallic catalysts for a green and sustainable future,” *Chem. Soc. Rev.*, vol. 41, no. 24, pp. 8099–8139, 2012.